

INFORMATION TO USERS

This manuscript has been reproduced from the microfilm master. UMI films the text directly from the original or copy submitted. Thus, some thesis and dissertation copies are in typewriter face, while others may be from any type of computer printer.

The quality of this reproduction is dependent upon the quality of the copy submitted. Broken or indistinct print, colored or poor quality illustrations and photographs, print bleedthrough, substandard margins, and improper alignment can adversely affect reproduction.

In the unlikely event that the author did not send UMI a complete manuscript and there are missing pages, these will be noted. Also, if unauthorized copyright material had to be removed, a note will indicate the deletion.

Oversize materials (e.g., maps, drawings, charts) are reproduced by sectioning the original, beginning at the upper left-hand corner and continuing from left to right in equal sections with small overlaps. Each original is also photographed in one exposure and is included in reduced form at the back of the book.

Photographs included in the original manuscript have been reproduced xerographically in this copy. Higher quality 6" x 9" black and white photographic prints are available for any photographs or illustrations appearing in this copy for an additional charge. Contact UMI directly to order.

U·M·I

University Microfilms International
A Bell & Howell Information Company
300 North Zeeb Road, Ann Arbor, MI 48106-1346 USA
313/761-4700 800/521-0600

Order Number 9322664

**Microwave measurements on transition metal and weakly bound
molecular complexes**

Roehrig, Mark August, Ph.D.

The University of Arizona, 1993

U·M·I
300 N. Zeeb Rd.
Ann Arbor, MI 48106

MICROWAVE MEASUREMENTS ON
TRANSITION METAL AND WEAKLY
BOUND MOLECULAR COMPLEXES

by

Mark August Roehrig

A Dissertation submitted to the Faculty of the

DEPARTMENT OF CHEMISTRY

In Partial Fulfillment of the Requirements

For the Degree of

DOCTOR OF PHILOSOPHY

In the Graduate College

THE UNIVERSITY OF ARIZONA

1 9 9 3

THE UNIVERSITY OF ARIZONA
GRADUATE COLLEGE

As members of the Final Examination Committee, we certify that we have read the dissertation prepared by Mark August Roehrig entitled Microwave Measurements on Transition Metal and Weakly Bound Molecular Complexes

and recommend that it be accepted as fulfilling the dissertation requirement for the Degree of Doctor of Philosophy

<u><i>S.G. Kukolich</i></u>	<u>4-26-93</u>
Dr. S.G. Kukolich	Date
<u><i>W.R. Salzman</i></u>	<u>26 APR 93</u>
Dr. W.R. Salzman	Date
<u><i>Ludvik Adamowicz</i></u>	<u>26 APR 93</u>
Dr. L. Adamowicz	Date
<u><i>M.F. Burke</i></u>	<u>26 Apr 93</u>
Dr. M.F. Burke	Date
<u><i>S.W. Buckner</i></u>	<u>4-26-93</u>
Dr. S.W. Buckner	Date

Final approval and acceptance of this dissertation is contingent upon the candidate's submission of the final copy of the dissertation to the Graduate College.

I hereby certify that I have read this dissertation prepared under my direction and recommend that it be accepted as fulfilling the dissertation requirement.

<u><i>Stephen S. Kukolich</i></u>	<u>April 26, 1993</u>
Dissertation Director	Date
Dr. S.G. Kukolich	

STATEMENT BY THE AUTHOR

This dissertation has been submitted in partial fulfillment of requirements for an advanced degree at the University of Arizona and is deposited in the University Library to be made available to borrowers under the rules of the Library.

Brief quotations from this dissertation are allowable without special permission, provided that accurate acknowledgment of source is made. Requests for permission for extended quotation from or reproduction of this manuscript in whole or in part may be granted by the head of the major department or the Dean of the Graduate College when in his or her judgment the proposed use of the material is in the interests of scholarship. In all other instances, however, permission must be obtained from the author.

SIGNED:



ACKNOWLEDGMENTS

To obtain one's goals is not a solo effort. Many people have influenced me in many ways and I would like to acknowledge them all. In one form or another they have helped me achieve what I have set out to do in my life. From my dear friends back home in Michigan to all the new friends I have made in Arizona, all to some degree, have contributed in realizing my goals. For this I am eternally grateful.

In each endeavor there are always a few people who have, upon reflection, made themselves more available and therefore instrumental in achieving one's goals. One of those persons is Steve Kukolich, whose guidance and criticism has helped me shape my outlook in science and made me a confident but realistic researcher. I have also learned from Steve the importance of completing a 'project' and looking forward to the next one. I wish to take this opportunity and thank him for his time and effort in helping me complete my 'project'. I also wish to thank Ludwik Adamowicz who has always had the time and patience to interact with me during my stay here in Arizona.

Over the years there have been two people who have always supported me unconditionally, even when I had 'crazy ideas on the shore of a lake'. Those people are Gerd and Gerti Röhrig, my parents. I do not know how to even begin to thank them. It is due to them that I have had the opportunity to attempt many things in my life and because of them I can look back at what I have accomplished with the sense of who I am and where I have come from. Thanks.

In the end there is usually one person who has made the most of any situation. My one person is Gill. By being there she has made my life much more interesting and her care and support have given me so much that I do not know what to say. However, what I can say is, I look forward to sharing a life with her.

TABLE OF CONTENTS

LIST OF TABLES	9
LIST OF FIGURES	12
ABSTRACT	13
CHAPTER I: INTRODUCTION	14
I.1 Transition Metal Complexes	15
I.2 Overview of Research	17
CHAPTER II: PULSED BEAM FOURIER TRANSFORM MICROWAVE SPECTROSCOPY	19
II.1 Properties of Supersonic Expansions	19
II.2 Polarization and Emission of the Expanding Gas	23
II.3 Machine Diagram and Details of Operation	26
II.4 Gas and Sample Handling	30
II.5 PB-FTS Stark Experiment	33
CHAPTER III: QUADRUPOLE COUPLING IN NOCl AND ClF ₃	36
III.1 NOCl Spectrum	37
III.1.i Synthesis of NOCl	39
III.1.ii Pulsed Beam Measurements	39
III.1.iii Molecular Beam Maser Measurements	41
III.1.iv Hyperfine Structure and Analysis	44

TABLE OF CONTENTS - *continued*

III.2 ClF ₃ Spectrum and Structure	48
III.2.i Experimental	48
III.2.ii ClF ₃ Hyperfine Analysis	49
III.2.iii Data Analysis	50
III.2.iv Structural Analysis	51
III.2.v Discussion of ClF ₃	53
III.3 Townes Dailey Interpretation of Quadrupole Data	54

CHAPTER IV: MICROWAVE MEASUREMENTS OF COBALT TRI-	
CARBONYL NITROSYL, CYCLOPENTADIENYL COBALT DI-CARBONYL,	
AND CYCLOPENTADIENYL MANGANESE TRI-CARBONYL	
	58
IV.1 Nuclear Quadrupole Coupling in Co(CO) ₃ NO	59
IV.1.i Pulsed Beam Measurements	61
IV.1.ii Rotational and Hyperfine Analysis	62
IV.1.iii Summary	66
IV.2 CpCo(CO) ₂ : Hindered Rotor Spectrum	67
IV.2.i Experimental Considerations	67
IV.2.ii Data Analysis	68
IV.2.iii Quadrupole Coupling	73
IV.2.iv Results and Discussion	73
IV.3 Manganese Quadrupole Coupling in CpMn(CO) ₃	76
IV.3.i Data Analysis	76
IV.3.ii Experimental Results	81
IV.3.iii Summary	84

TABLE OF CONTENTS - *continued*

CHAPTER V: MICROWAVE SPECTRA OF CYCLOBUTADIENE IRON TRI-CARBONYL, CYCLOHEXADIENE IRON TRI-CARBONYL, AND BUTADIENE IRON TRI-CARBONYL	85
V.1 Cyclobutadiene Iron tri-Carbonyl	85
V.1.i Experimental	87
V.1.ii Results and Discussion	89
V.1.iii Summary	93
V.2 Cyclohexadiene Iron tri-Carbonyl	94
V.2.i Microwave Spectrum and Analysis	95
V.2.ii Structural Parameters	96
V.2.iii Results	101
V.3 Butadiene Iron tri-Carbonyl Kraitchman Analysis	104
V.3.i Kraitchman Equations and Molecular Structure	105
 CHAPTER VI: MICROWAVE SPECTRUM, STRUCTURE AND DIPOLE MOMENT OF THE HCCH-CO COMPLEX	 109
VI.1 Experimental	109
VI.2 Spectral Analysis	113
VI.3 Structural Analysis	114
VI.4 D_J , Force Constant, and Binding Energy	117
VI.5 Dipole Moment	120
VI.6 Summary	121

TABLE OF CONTENTS - *continued*

CHAPTER VII: SUMMARY AND CONCLUSIONS	123
VII.1 Future Directions	125
APPENDIX A.I: ClF_3 TRANSITION FREQUENCIES	127
APPENDIX A.II: TRANSITION FREQUENCIES FOR COBALT TRI-CARBONYL NITROSYL, CYCLOPENTADIENYL COBALT DI-CARBONYL, AND CYCLOPENTADIENYL MANGANESE TRI-CARBONYL	132
APPENDIX A.III: TRANSITION FREQUENCIES FOR CYCLOBUTADIENE IRON TRI-CARBONYL, CYCLOHEXADIENE IRON TRI-CARBONYL, AND BUTADIENE IRON TRI-CARBONYL	144
REFERENCES	151

LIST OF TABLES

Table III.1 Transition frequencies for NOCl obtained on the PB-FTS machine.	40
Table III.2 Transition frequencies for NOCl obtained on the maser spectrometer	42
Table III.3 Values of the molecular parameters for NOCl obtained from fitting the transition frequencies in Tables III.2 and III.3.	47
Table III.4 Values of the molecular parameters obtained for ClF ₃	51
Table III.5 Effective structure calculation for ClF ₃	53
Table III.6 Nitrogen quadrupole coupling strength for some typical molecules and NOCl.	55
Table III.7 Chlorine quadrupole coupling strength and unbalance of p electrons.	56
Table IV.1 Molecular constants for Co(CO) ₃ NO	64
Table IV.2 Molecular constants for CpCo(CO) ₂	71
Table IV.3 Some N-fold potential barriers.	75
Table IV.4 Best parameters to the hyperfine transitions for CpMn(CO) ₃ . . .	79
Table IV.5 Comparison of the distortion parameters D _J for some transition metal compounds.	80
Table V.1 Best fit values for CbFe(CO) ₃	89
Table V.2 Comparison of distortion parameters for some other transition metal complexes with CbFe(CO) ₃	91
Table V.3 Rotational and distortion constants for C-hexFe(CO) ₃	96

LIST OF TABLES - *continued*

Table V.4 Comparison of measured rotational constants and calculated constants from X-ray data	97
Table V.5 Structural parameters describing relative orientation of the ligands in C-hexFe(CO) ₃	98
Table V.6 Selected interatomic distances from X-ray and optimized X-ray coordinates	101
Table V.7 Selected intramolecular angles from X-ray and optimized X-ray coordinates	103
Table V.8 Comparison of interatomic distances and angles between Kraitchman and structure fit analyses	107
Table VI.1 Measured rotational constants for normal and isotopically labeled HCCH-CO	112
Table VI.2 Best fit results for the isotopomers of HCCH- CO	114
Table VI.3 Measured and calculated rotational constants obtained from the least squares fit to moments of inertia	116
Table VI.4 Structural parameters for HCCH-CO	117
Table VI.5 Calculated k_s , ν_s , and ϵ for the HCCH-CO complex	118
Table VI.6 Comparison of HCCH-CO dynamical parameters with other CO complexes	119
Table VI.7 Observed stark shifts for HCCH-CO	120
Table A.I.1 Measured and calculated transition frequencies for ³⁵ ClF ₃	128
Table A.I.2 Measured and calculated transition frequencies for ³⁷ ClF ₃	130

LIST OF TABLES - *continued*

Table A.II.1 Measured and calculated frequencies for the $J=2 \rightarrow 3$, $K=0$ transitions of $\text{Co}(\text{CO})_3\text{NO}$	133
Table A.II.2 Measured and calculated frequencies for the $J=3 \rightarrow 4$, $K=0$ transitions of $\text{Co}(\text{CO})_3\text{NO}$	134
Table A.II.3 Measured and calculated frequencies for the $J=4 \rightarrow 5$, $K=0$ transitions of $\text{Co}(\text{CO})_3\text{NO}$	135
Table A.II.4 Measured and calculated frequencies for the $J=5 \rightarrow 6$, $K=0$ transitions of $\text{Co}(\text{CO})_3\text{NO}$	136
Table A.II.5 Measured and calculated frequencies for the $J=3 \rightarrow 4$, $K=3$ transitions of $\text{Co}(\text{CO})_3\text{NO}$	137
Table A.II.6 Measured and calculated hindered rotor transition frequencies for $\text{CpCo}(\text{CO})_2$	138
Table A.II.7 Measured and calculated $K=0$ hyperfine transition frequencies for $\text{CpCo}(\text{CO})_2$	139
Table A.II.8 Measured and calculated $K \neq 0$ hyperfine transition frequencies for $\text{CpCo}(\text{CO})_2$	140
Table A.II.9 Hyperfine components for the $J=3 \rightarrow 4$ transition of $\text{CpMn}(\text{CO})_3$	141
Table A.II.10 Hyperfine components for the $J=4 \rightarrow 5$ transition of $\text{CpMn}(\text{CO})_3$	142
Table A.II.11 Hyperfine components for the $J=5 \rightarrow 6$ transition of $\text{CpMn}(\text{CO})_3$	143
Table A.II.12 Hyperfine components for the $J=6 \rightarrow 7$ transition of $\text{CpMn}(\text{CO})_3$	144
Table A.III.1 Measured and calculated frequencies for $\text{CbFe}(\text{CO})_3$	146
Table A.III.2 Measured and calculated frequencies for ^{56}Fe C-hex $\text{Fe}(\text{CO})_3$	147
Table A.III.3 Measured and calculated frequencies for ^{54}Fe C-hex $\text{Fe}(\text{CO})_3$	150

LIST OF FIGURES

Figure II.1 Block diagram of the Arizona pulsed beam Fourier transform microwave spectrometer	27
Figure II.2 Timing diagram for the pulse sequence	29
Figure II.3 Sample FID and FT spectra obtained by the Arizona machine . .	30
Figure II.4 Stark plate calibration plot	34
Figure III.1 Substitution structure of NOCl	38
Figure III.2 FT-spectrum of the NOCl $J=0 \rightarrow 1$ hyperfine transition	40
Figure III.3 NOCl maser spectrum	42
Figure III.4 Block diagram for the maser spectrometer	44
Figure III.5 Structural parameters for ClF_3	52
Figure IV.1 Structure of $\text{Co}(\text{CO})_3\text{NO}$	60
Figure IV.2 Structural parameters for $\text{CpCo}(\text{CO})_2$	72
Figure IV.3 Structure of $\text{CpMn}(\text{CO})_3$	81
Figure V.1 Structure of $\text{CbFe}(\text{CO})_3$	87
Figure V.2 Structural parameters for C-hex $\text{Fe}(\text{CO})_3$	99
Figure V.3 Conformation and orientation of the C-hex $\text{Fe}(\text{CO})_3$ in the principal axis system	102
Figure V.4 Molecular structure and fitted parameters as determined from Kraitchman analysis	104
Figure VI.1 Vibrationally averaged structure of HCCH-CO	115
Figure VI.2 Plot of $\Delta\nu$ vs. ϵ^2 for HCCH-CO	121

ABSTRACT

High resolution microwave spectra for the transition metal compounds cobalt tri-carbonyl nitrosyl ($\text{Co}(\text{CO})_3\text{NO}$), cyclopentadienyl cobalt di-carbonyl ($\text{CpCo}(\text{CO})_2$), and cyclopentadienyl manganese tri-carbonyl ($\text{CpMn}(\text{CO})_3$) were obtained for the first time using pulsed beam Fourier transform spectroscopy. An oblate symmetric top spectrum was measured for $\text{Co}(\text{CO})_3\text{NO}$ and the first gas phase value of the cobalt nuclear quadrupole coupling parameter was obtained. The asymmetric top hindered rotor spectrum for $\text{CpCo}(\text{CO})_2$ was measured and a barrier to internal rotation was estimated from the spectrum. Analysis of the prolate symmetric top hyperfine spectrum of $\text{CpMn}(\text{CO})_3$ yielded the first gas phase measurement of the rotational constant and the Mn nuclear quadrupole coupling. High resolution microwave spectra for the iron containing transition metal complexes cyclobutadiene iron tri-carbonyl ($\text{CbFe}(\text{CO})_3$), cyclohexadiene iron tri-carbonyl ($\text{C-hexFe}(\text{CO})_3$) were obtained and a Kraitchman analysis of the isotopic substitution data for the butadiene iron tri-carbonyl ($\text{BuFe}(\text{CO})_3$) is also discussed. Structural parameters for HCCH-CO were obtained from various isotopomers for this complex. An analysis of the distortion parameter D_J yielded an estimation of the binding energy for this weakly bound complex. Analysis of spectra for nitrosyl chloride (NOCl) and chlorine tri-fluoride (ClF_3) yielded the first high resolution low J data sets for these molecules. The quadrupole coupling data are interpreted using the Townes- Dailey model for quadrupole coupling and an improved ground state structure for ClF_3 was obtained. Microwave spectra reported here were obtained using a pulsed beam Fourier transform microwave spectrometer constructed at the University of Arizona. The design is similar to original Flygare-Balle apparatus with many modifications for improving signal sensitivity and data acquisition.

CHAPTER I: INTRODUCTION

Microwave spectroscopy has been used for many years to obtain very precise structural measurements for molecular systems. To this day, it is considered to be one of the highest resolution forms of gas phase molecular spectroscopy known with linewidths as narrow as 2 kHz measured from microwave maser spectrometers [1]. Not only do the small linewidths contribute to the overall precision of structural measurements, it has also contributed to the measurements of small hyperfine interactions of nuclear properties of atoms contained within the molecule.

Over the years, large advances have been made in the technology used in microwave techniques. In the last ten years an instrument was developed by Flygare and Balle [2] that has brought new life into microwave spectroscopy. By combining the techniques of free jet expansions and Fourier transform spectroscopy, the study of van der Waals molecules, which was pioneered by Klemperer in the microwave region in the 1970's, has exploded. Conditions in the gas expansion are such that van der Waals molecules are readily formed and stabilized long enough so rotational spectra can be obtained. Today more than 60 % of the high resolution microwave data of these complexes has been obtained by the PB-FTS technique from groups around the world.

Study of van der Waals molecules continues today with experiments designed in microwave and other regions of the electromagnetic spectrum and even many *ab initio* and semiempirical calculations have been stimulated by the large

amount of data obtained from PB-FTS. However, the PB-FTS technique lends itself to study many other areas of molecular spectroscopy as well. Starting in the early 1950's groups have been trying to obtain high resolution spectra of larger more complex molecules like transition metal complexes. The early studies resulted in obtaining minimal amounts of spectral information, often obtaining only approximations of rotational constants. The fundamental obstacle was the large moments of inertia which produced closely spaced rotational transitions in the spectra making the spectra difficult to assign.

Combining PB-FTS with the study of transition metal complexes and other large molecules has proven most successful as demonstrated by the results presented in this dissertation. New information on structure, bonding and nuclear interactions have been obtained for these compounds and will add to the overall understanding of the nature of these compounds.

I.1 Transition Metal Complexes

Transition metal or organometallic complexes combine organic compounds and transition metals in a variety of ways. From binding of the organic compound to a transition metal center, the reactivity or stability of the ligand can be significantly altered. For example, free cyclobutadiene does not exist, but when complexed to $\text{Fe}(\text{CO})_3$ it is greatly stabilized and can be examined experimentally in many ways. The converse is also true, stable compounds can combine with transition metal compounds and be activated to react [3] often in some predictable and beneficial way. Synthetic chemists turn to organometallic methods to exploit their special reactivity and selectivity that cannot be found in conventional methods. Therefore, there

is a precedence in obtaining new information on transition metal complexes which could help in the overall understanding of these compounds and their properties.

Over the many years transition metal chemistry has been studied, a number of factors have been identified that seem to form a basis for a rationalism underlying the understanding of transition metal reactivity. One of those factors is 'the geometrical restrictions to the orientation of bonding of ligands in many transition metal complexes. This determines the alignment of reacting species brought together by the metal, so providing control of both chemical selectivity and stereoselectivity'[3]. Loosely translated, the structure of these transition metal complexes, especially knowing how the ligands are oriented about the metal center, can improve insight into how the reacting species interacts with the complex. Obtaining very precise data sensitive to the structure of these molecules will aid in the general understanding of transition metal complexes.

One particular field of transition metal chemistry can greatly benefit from knowing detailed information of the geometries of these complexes, catalysis. Synthetic methods that are catalyzed by soluble transition metal complexes of Co, Mn, and Fe in the formation organic compounds are used extensively in industry[4]. Most of the structural information on these complexes comes from solid state X-ray diffraction studies. Though very accurate in determining the locations of the large atoms in the complex, smaller atoms of the ligands such as hydrogens are undetermined by X-ray diffraction. The orientation of the hydrogens often indicate some unusual bonding interaction between the ligand and metal center. Since X-ray diffraction is measured in the solid state, the crystal packing of the solid perturbs the geometry of the complex. Sometimes these affects are small but other times they can be quite large. Therefore, gas phase measurements of transition

metal complexes is very desirable to provide information on the intrinsic geometries of these molecules.

I.2 Overview of Research

The studies of the structures of some transition metal complexes presented here are the beginnings of a research program involving the use of pulsed beam Fourier transform microwave spectroscopy (PB-FTS) and transition metal complexes. The goal was to obtain high resolution spectra for these compounds so that more detailed and perhaps new information could be obtained on their structures as well as nuclear properties of several of the transition metals involved. Throughout the research advances were made in the handling of these compounds so as to provide a knowledge base for future studies of more reactive species like transition metal hydrides.

Studies involving the interhalogen compound ClF_3 and the nitrosyl NOCl were made in order to obtain a high resolution data set of low J transitions where the complicating effects of nuclear quadrupole coupling is somewhat simplified. A model interpreting the quadrupole coupling data in terms of an unbalance of bonding electrons was then applied to this high resolution data set to acquire an accurate description of the chemical bonding in terms of the interaction of the nuclear quadrupole moment and overall rotation.

Spectra acquired on the HCCH-CO weakly bound complex were made to establish the ground state vibrationally averaged structure of this complex. An analysis of the distortion parameter D_J was made to investigate the weak intermolecular dynamics of this system by estimating the weak bond dissociating energy. This study compliments some of the previous work done on weakly bound molecular

complexes in the Kukolich laboratory at the University of Arizona. The study of these complexes is ongoing with more and more emphasis on combining experimental and theoretical approaches. An excellent review on polyatomic weakly bound complexes can be found elsewhere [5,6].

CHAPTER II:
PULSED BEAM FOURIER TRANSFORM
MICROWAVE SPECTROSCOPY

The technique of pulsed beam Fourier transform microwave spectroscopy (PB-FTS) has been around for more than ten years [2]. The molecular systems available to its scrutiny are almost unlimited with the determining factor being that of successfully introducing a sample intact into the apparatus. The data obtained from these machines is of unquestionable quality in terms of sensitivity and resolution. In this Chapter, illustration of this technique will be achieved through a moderate discussion of the fundamentals of operation from supersonic free jet expansions, polarization of the expanding gas, detection of the molecular signals to data acquisition and analysis. For details on the construction of the apparatus please see reference [7] .

II.1. Properties of Supersonic Expansions

To understand the basic properties of a supersonic expansion, it is worthwhile to briefly contrast it with the more familiar properties of an effusive flow through a nozzle source. To acquire effusive flow through a nozzle source, each particle's motion must be independent of all other particle's, that is, no collisions occur between the particles to alter their energy in some way. For effusive flow to exist through a nozzle of diameter D , the condition is,

$$\frac{\lambda'}{D} \gg 1 \quad (1)$$

where λ' is the mean free path of the particle, and $\frac{\lambda'}{D}$ is known as the Knudsen number. The mean free path is given by

$$\lambda' = (2^{\frac{1}{2}} \pi \rho_n d^2)^{-1} \quad (2)$$

where d is a molecular diameter. For an effusive source $\rho_n = \rho_0$, the source or stagnation molecular density. For a typical molecular diameter of $d \approx 4 \times 10^{-8}$ cm and for 1 atmosphere, the mean free path is 4.3×10^{-5} mm. For a fairly standard nozzle diameter of 1 mm used in pulsed beam machines of today and stagnation pressures ranging from 0.5 to 2.0 atmospheres the gas exiting from the nozzle under these conditions is far from the effusive limit. As we can see, the effusive flow essentially retains the characteristics of the stagnation reservoir, with the difference between the gas in the reservoir and the gas exiting the nozzle being the change in Maxwellian distribution of molecular velocities, the distribution is now only over a single velocity component of the one coinciding with the exit hole of the nozzle source.

In the pulsed beam apparatuses of today, the gas exiting the nozzle undergoes drastic changes in its properties when it is compared to the reservoir conditions. These changes can be attributed to what is occurring in the nozzle as the gas exits the reservoir. The gas does not leave the reservoir unhindered, but rather, undergoes many collisions within the nozzle itself. These collisions have the effect of

interconverting the stored internal energy in the form of rotations and vibrations into mass flow thus adiabatically cooling the gas. The effective rotational and vibrational temperatures drop, the velocity distribution narrows and moves out along the flow velocity axis through the nozzle. As the gas exits the plane of the nozzle, it expands freely undergoing no more collisions with itself thus producing relatively low temperatures within the expansion[8] .

It is apparent from the rotational and vibrational cooling described above, that to a high resolution spectroscopist, the supersonic free jet expansion is an indispensable and powerful tool in the acquisition of complicated spectra of unique molecular species such as transition metal and weakly bound complexes. The rotational and vibrational congestion in the molecular spectra is dramatically reduced by the free jet expansion.

The discussion above was based on equations describing free jet expansions in the continuous or equilibrium conditions [8-12]. The supersonic free jet incorporated into the PB-FTS is used in a pulsed fashion and the duration of time the valve is actually open is very short and the gas is expanded into a high vacuum, the gas achieves equilibrium expansion properties very rapidly under these conditions and these equations will hold. In addition, the gas pulsed into the vacuum of the chamber is mixture of a few percent of sample gas in typically 1 to 2 atmospheres of a carrier gas such as argon or neon. Therefore the characteristics of the expansion are dominated by the properties of the carrier gas.

The major considerations of the free jet expansion are the temperature of the gas, its spatial distribution during the expansion and the number of particles entering the vacuum. The temperature and spatial distribution was described above and the number of particles entering the vacuum is a vital factor that must be

considered as well since, it is obvious, that if the number density of sample molecules is not high enough during the expansion then detection of the molecular signal will not be possible or at least very difficult. The number of molecules released during a gas pulse is given [2, 8] by,

$$N = \rho_0 a_0 A_n t_v (0.31) \quad (3)$$

where ρ_0 and a_0 are the source number density and local speed of sound, A_n is the nozzle area, t_v is the time the valve is open. The factor of (0.31) takes into account for the discharge coefficient for a monatomic gas and the flow velocity of the gas at the nozzle in terms of the Mach number [8]. Typical values for the quantities are, $t_v = 3$ ms, $A_n = \pi$ mm² (for a nozzle diameter of 1 mm), and for 1 atm and 300 K $\rho_0 = 2.69 \times 10^{19}$ molecules/cm³, there are 4×10^{18} particles released from the nozzle into the cavity. Considering that the molecules are travelling around 3.8×10^4 cm/s, there are about one tenth of this total in the beam waist and since it is a seeded beam there are usually only 1 to 5 percent of the number in the waist. If we consider the limiting condition of forming dimers in the expansion then this number drops further still. There has been much theory and experiment [13- 17] on the formation of dimers in an expanding gas and the simple expression $p^2 D$ can be used to predict the amount of dimer formation in the expansion, p and D are the pressure or number density at the nozzle and nozzle diameter respectively. From this expression and experimental results [14, 15], dimer mole fractions as high as 0.1 have been reported. This is sufficient for detection of molecular signals using microwave spectroscopy.

The above limiting case example of dimer formation was used to illustrate that even under the conditions of the free jet expansion, the molecular number density of unique molecular species is sufficient for detection. And while most of the experiments discussed here involve only single monomer detection, the effect of dimer formation is ever present to some degree. Therefore for every experiment the conditions used in the stagnation reservoir are very critical to the successful measurement of the molecular spectra. More detail will be given to the reservoir conditions in Section II.iv Modifications to PB-FTS.

II.2. Polarization and Emission of the Expanding Gas

An understanding of the free jet expansion properties is necessary to work out timing schemes for pulsing the microwave radiation into the Fabry-Perot cavity and polarizing the gas with this radiation. A macroscopic polarization of a gas containing a number of nondegenerate two-level quantum systems with a static electric field has the form [2]

$$p(\mathbf{r}, \mathbf{v}, t) = (p_r(\mathbf{r}, \mathbf{v}, t) + ip_i(\mathbf{r}, \mathbf{v}, t))\exp(i\omega t) + c.c. \quad (4)$$

where p_r and p_i are real valued functions of the six phase- space coordinates \mathbf{r} , \mathbf{v} , and of t , and 'c.c.' is the complex conjugate. Assigning each coordinate \mathbf{r} of the gas with a unique velocity $\mathbf{v}(\mathbf{r})$, the polarization components p_r and p_i and the two-level population difference per unit volume associated with the velocity \mathbf{v} , $\Delta n(\mathbf{r}, \mathbf{v}, t)$, satisfy a set of Bloch-type coupled partial differential equations [2]:

$$\left(\frac{\partial}{\partial t} + \mathbf{v} \cdot \nabla\right) p_r + \Delta\omega p_i + p_r/T_2 = 0 \quad (5)$$

$$\left(\frac{\partial}{\partial t} + \mathbf{v} \cdot \nabla\right) p_i - \Delta\omega p_r + \kappa^2 \varepsilon(\mathbf{r}, t) \frac{\hbar \Delta n}{4} + p_i/T_2 = 0 \quad (6)$$

$$\left(\frac{\partial}{\partial t} + \mathbf{v} \cdot \nabla\right) \frac{\hbar \Delta n}{4} - \varepsilon(\mathbf{r}, t) p_i + \frac{\hbar(\Delta n - \Delta n_0)}{4T_1} = 0 \quad (7)$$

where $\Delta\omega = \omega_0 - \omega$, the difference between the molecular transition angular frequency ω_0 , and the carrier or stimulating angular frequency ω , T_1 and T_2 are phenomenologically introduced first-order relaxation terms, Δn_0 is the equilibrium value of Δn in the absence of an electric field and is considered to be constant, and

$$\kappa = 2\hbar^{-1} |\langle a | \mu_z | b \rangle| \quad (8)$$

where $\langle a | \mu_z | b \rangle$ is the dipole transition moment connecting the two levels.

These equations describe the interaction of the electric field or the microwave pulse with the gas pulse. The gas is pulsed into a Fabry-Perot cavity which is inherently a narrow bandwidth, high electric field instrument, so solution to these equations can be found by considering only the on resonance, $\Delta\omega = 0$, form of these equations. When the polarization pulse length, τ_p , is short enough, the molecules travel only a short distance when compared to the characteristic distance of variations in p_r and p_i , and Δn , and making $\tau_p \ll T_1, T_2$, the terms involving $\mathbf{v} \cdot \nabla$ and

T_1 and T_2 may be neglected in the above equations. The solutions to the resulting equations are:

$$p_r(\mathbf{r}, t) = 0 \quad (9)$$

$$p_i(\mathbf{r}, t) = -\frac{\kappa\hbar\Delta n_0}{4} \sin\left(\kappa \int_{t_0}^t \varepsilon(\mathbf{r}, t') dt'\right) \quad (10)$$

$$\Delta n(\mathbf{r}, t) = \Delta n_0 \cos\left(\kappa \int_{t_0}^t \varepsilon(\mathbf{r}, t') dt'\right) \quad (11)$$

The appropriate form of $\varepsilon(\mathbf{r}, t)$ depends on the TEM_{00q} cavity mode of the Fabry-Perot cavity. The derivation of the form for $\varepsilon(\mathbf{r}, t)$ is given in detail in [2] and only the results will be given here. Using the results from [2] and substituting them into the above equations, give at the end of the pulse duration τ_p ,

$$p_i(\mathbf{r}, t) = -\frac{\kappa\hbar\Delta n_0}{4} \times \sin\left(\kappa E_0 \tau_p \left(\frac{\omega_0}{\omega}\right) \exp(-\rho^2/\omega^2) \cos(ky - \pi q/2)\right) \quad (12)$$

with a similar expression for Δn .

After the polarizing radiation has been removed, p_r , p_i , and Δn continue to evolve as described by the above equation without the $\varepsilon(\mathbf{r}, t)$ terms thus producing an electric field within the Fabry-Perot cavity. Again, details of the derivation

of the emission process are given in [2] and presented here are the results of this derivation. The electric field produced by the emitting molecules can be written in the following simplified form:

$$\varepsilon(t) = \exp(-t/T_2)\cos[\omega_0 t + (\omega - \omega_0)]I(t) \quad (13)$$

where t_1 is the time at the end of the polarization pulse and ω_0 and ω are the molecular transition and polarizing angular frequencies, respectively. The function $I(t)$ contains all the lineshape information, while the remaining terms provide an exponential damping and center the emission at ω_0 [18].

The envelope function $I(t)$ accounts for amplitude variations of the emitted signal characteristics of the particular cavity mode, the molecular density distribution in the gas phase in the gas pulse at time t and two types of signal damping. The first type of damping corresponds to all fall off due to motion of the molecules out of the cavity and has been shown to be small [2]. The second, and major type of damping has been called Doppler dephasing and results from the movement of molecules from a region where they were polarized with one phase to regions where they would have been polarized with a different phase [19]. This is then the molecular signal being emitted into the Fabry-Perot cavity which in turn is detected, saved and Fourier transformed to yield the spectral information desired. Details are given in the Section II.iii.

II.3. Machine Diagram and Details of Operation

The essential theory behind the operation of the PB-FTS was given in the previous sections and presented in this section are the details of operation of the

Arizona Machine. A block diagram of the spectrometer is shown in Figure II.1. The gas or sample handling will be discussed in more detail in Section II.iv and this section is concerned with only the details of integrating the gas pulses and the microwave stimulation and subsequent detection and data handling elements such as storing the signal and Fourier transformation.

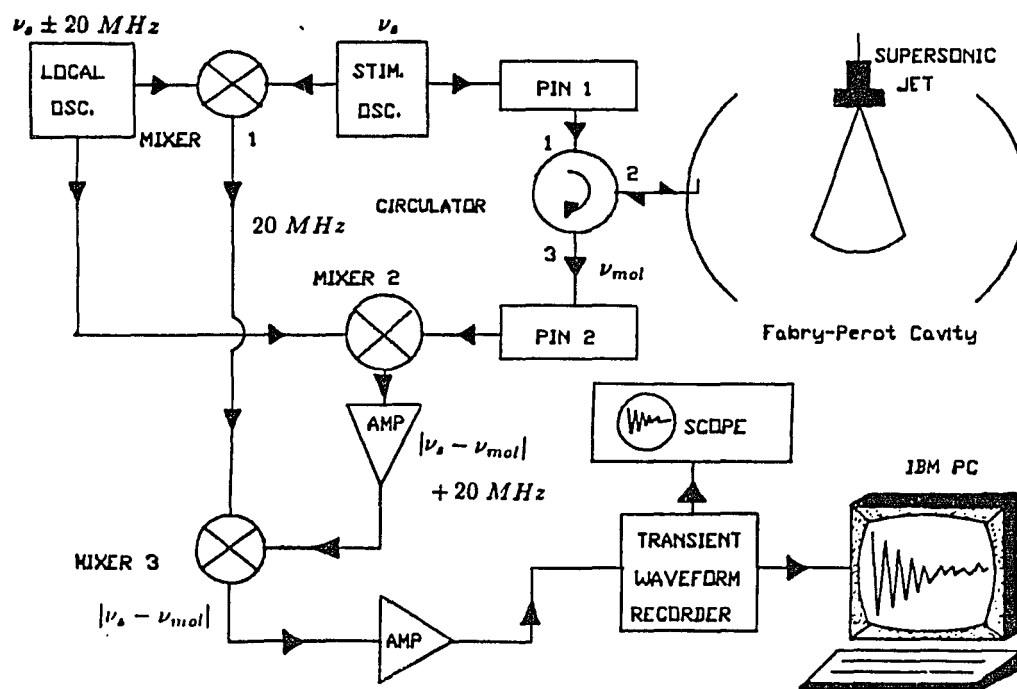


Figure II.1 Block diagram of the Arizona pulsed beam Fourier transform microwave spectrometer.

A stimulating frequency in the 4-18 GHz range is generated by locking a harmonic frequency generated in the 800 to 900 MHz range by a Hewlett Packard frequency synthesizer to a solid state oscillating device. For frequencies generated in the C-band range, 4 to 8 GHz, a YIG tuned transistor oscillators (Avantek 7443 and 7553, 30 and 100mW respectively) are used. In X- band, 8 to 12 GHz and Ku-band, 12 to 18 GHz, the oscillators are YIG-tuned Gunn diode devices (Watkins-Johnson WJ-5008-303F in X- band and WJ-5041-303F in Ku-band both rated at 30 mW). A gas pulse is admitted to the Fabry-Perot cavity through through a solenoid valve (General Valve Corp. 9-181-100) resulting in a supersonic expansion with rotational and vibrational cooling. After a short period of time ($75 \mu\text{s}$ to 3 ms), a 0.1 to 1.0 μs duration stimulating microwave pulse is coupled into the cavity through a 1/4 - wave antenna mounted in the center of one of the mirrors by opening a pin diode switch (PIN1) shown in Figure II.1. The microwave pulse polarizes the gas molecules as described in Section II.ii and the duration of the pulse, τ_p , is defined by how long PIN1 is left open. This results in a $\pi/2$ pulse and a superposition of rotational states will subsequently decay emitting radiation at the microwave frequency into the cavity in the form of a free induction decay or FID.

After PIN1 closes there is time delay before opening PIN2 to allow the energy stored in the cavity to decay away. This known as cavity ring and does not include any signals from the polarized gas which decays at a much slower rate than the cavity ring. PIN2 then opens coupling the FID out of the cavity through the same 1/4 -wave antenna and into a superheterodyne detection system. The timing sequence [7] of the pulse valve and PIN switches is shown in Figure II.2. The molecular FID $\nu_{molecular}$, which is in the GHz frequency range, is then mixed with a local oscillator which oscillates at $\nu_{loc} = |\nu_{stim} \pm 20 \text{ MHz}|$ which produces

an intermediate frequency $\nu_{int} = 20 \text{ MHz} + |\nu_{stim} \pm \nu_{molecular}|$. ν_{int} is filtered, amplified and mixed once more with a 20 MHz frequency to produce an offset frequency $\nu_{off} = |\nu_{stim} - \nu_{molecular}|$ which is in the 0 to 1 MHz range which is amplified one more time to enhance signal sensitivity. The ν_{off} is then digitized into 4096 channels at a 20 MHz sampling rate using a Physical Data 522A transient waveform recorder. The digital data are transferred to an IBM PC where they are averaged and saved onto a floppy diskette in the form of the digitized offset FID signal ν_{off} . The averaging sequence is such that gas pulses are applied on alternate microwave pulses and alternating signals are added and subtracted to produce the average. This has the affect of removing most of the spurious signals due to cavity ring and switch noise. From there it is Fourier transformed to yield the relevant spectral information. A sample FID and FT spectrum is shown Figure II.3.

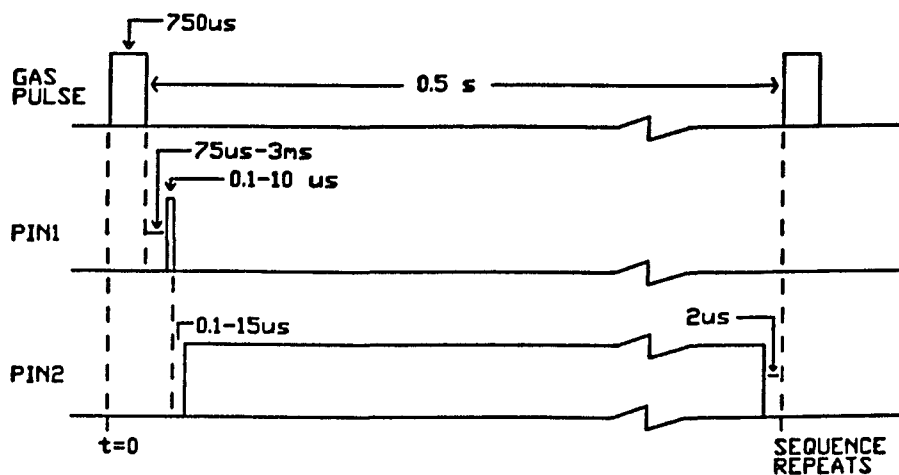


Figure II.2 Timing diagram for the pulse sequence. Taken from [7].

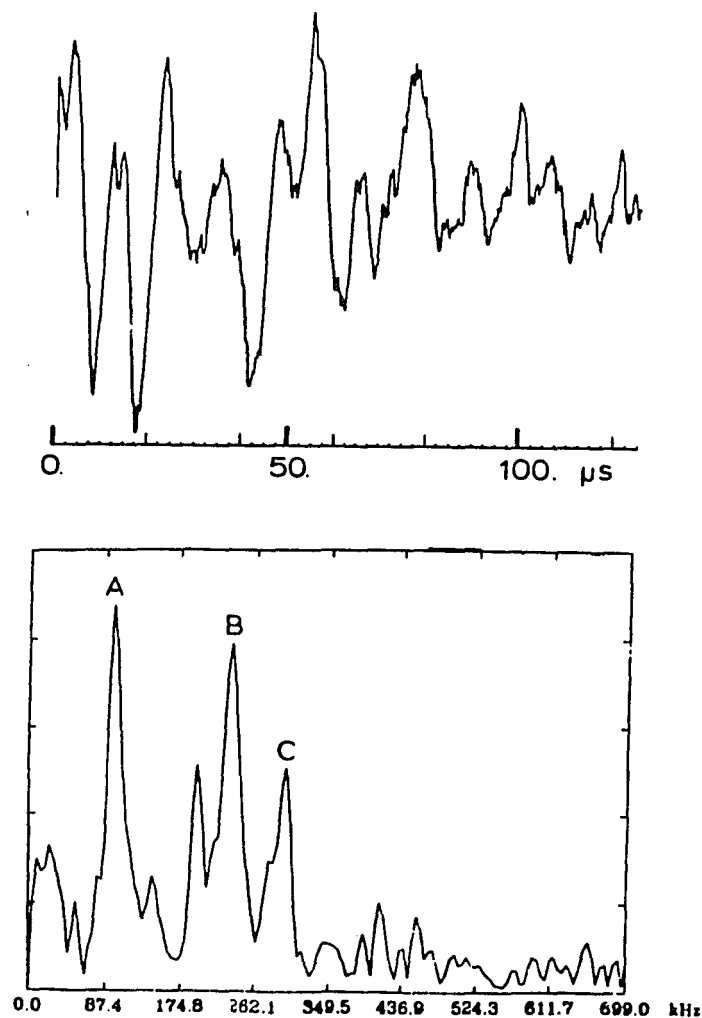


Figure II.3 Sample FID and FT-spectrum obtained from the Arizona PB-FTS machine.

II.4. Gas and Sample Handling

The gas handling system which delivers the carrier gas to the pulsed valve is described in more detail elsewhere [7]. Discussed in this section are the modifications made to part of the gas handling system which allows the study of samples which are not easily obtainable in the gas phase, *e.g.* transition metal complexes.

Most of the transition metal complexes discussed here are in a physical state at room temperature where obtaining sufficient vapor phase mole fractions is negligible. These compounds are usually in the liquid state or, sometimes, in the solid state at room temperature. Therefore to obtain sufficient vapor pressure to measure gas phase spectra, one needs to heat the sample up in a reservoir prior to pulsing into the cavity. However, just heating the sample is not enough since once coming into contact with cooler surfaces, the sample will immediately condense out of the vapor phase due to its high boiling point. Therefore, a system is required in which all the surfaces that the sample may come into contact with, including the pulse valve, be maintained at high enough temperatures to prevent condensation of the sample. The basic is to heat the sample and pulse valve at a constant elevated temperature within a stainless steel hot source. Heat is applied effectively through heat tape wrapped around and placed within the hot source and controlled by several variacs. An approximately 25 cm dia by 1 cm thick copper plate is placed over the top of the hot source to help in maintaining the temperature. The sample cells are made out of pyrex and are connected directly to the pulse via Teflon Swedge Lock fittings. The construction of the hot source is based the ideas and design of S. Kukolich.

With the construction of the hot source, the versatility of PB- FTS has been demonstrated once more. Temperatures as high as 77 °C have been successfully maintained with little difficulty in the performance of the pulse valve. However, long exposure to elevated temperatures seems to reduced the lifetime of the pulse valve components requiring more frequent replacements of these components. The limiting factor of this design seems to be the high temperature failure of the General Valve Corporation pulse valves. To obtain spectra at higher temperatures, perhaps the re- incorporation of the once used fuel injectors may be necessary since these devices are accustomed to operating at higher temperatures. This is currently being pursued.

II.5 PB-FTS Stark Experiment

The Stark effect is a valuable tool to high resolution spectroscopists, since it can be used to sort out rather complicated spectra by noting how certain transitions behave within an electric field, such as the first order Stark effect of a hindered rotor molecule. Obtaining the dipole moment μ of a molecule or weakly bound complex will all ways be considered valuable information because of how it relates to the fundamental properties of the molecule or complex. By incorporating Stark plates into the PB-FTS apparatus one can potentially couple the high sensitivity and resolution of the instrument with very precise measurements of the dipole moment.

Stark plates were constructed out of two 4 mm thick by 21.5 cm square aluminium plates where one side of each plate was polished to remove any surface imperfections. The corners of the plates were rounded with approximately a 2.5 cm radius so as to reduce the potential of electrical arcing while in the cavity of the spectrometer. The plates were suspended within the spectrometer along the centerline of gas expansion from the nozzle by milled nylon suspension anchors which attach to the same supports as the cavity mirrors do [7]. The spacing of the plates was chosen to be 10 cm so as to reduce the perturbation of the plates within the electric field of the Fabry-Perot cavity. High voltage of up 6000 Volts was applied to one of the plates so as to produce the Stark effect in the molecules during a gas expansion.

The plates were calibrated by measuring the Stark shifts in $^{16}\text{O}^{12}\text{C}^{32}\text{S}$ which has a very well known experimental value for its dipole moment. A calibration plot is shown in Figure II.5 from which the electric field and plate separation can be determined.

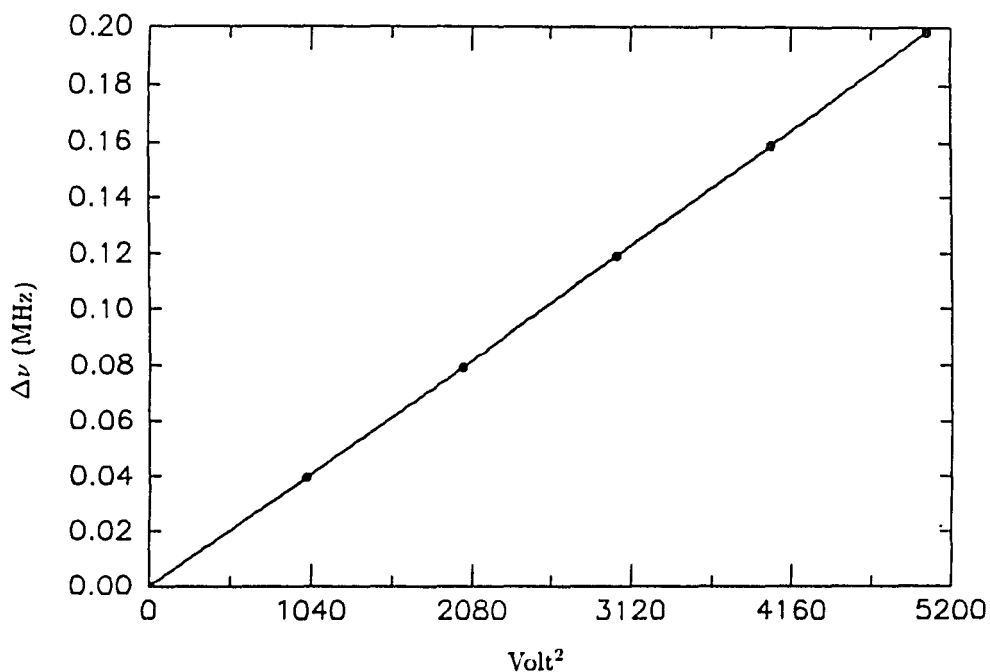


Figure II.4 Stark plate calibration plot for $^{16}\text{O}^{12}\text{C}^{32}\text{S}$ in the PB-FTS Arizona machine.

The results of the Stark experiment were below expectations. The perturbation of the electric field within the cavity due to the presence of the plates proved to be too great. Satisfactory spectra for molecules were hard to obtain since most low J transitions for molecules where the Stark splitting is simpler to analyze occurs in the C-band range. Obtaining spectra in the C-band is inherently difficult without

the presence of the Stark plates since the long wavelengths of C-band produce a limited number of modes in which to tune the cavity. In the future, it is desirable to change the design of the plates so as to reduce this perturbation within the cavity and hopefully yield better results. A successful dipole measurement was made on the HCCH-CO weakly bound complex and those results are discussed in Chapter VI.

CHAPTER III:

QUADRUPOLE COUPLING IN NOCI AND ClF₃

Analysis of nuclear quadrupole coupling hyperfine spectra can provide information about the electronic environment around the coupling atom within a molecule. The Townes-Daily[20] model allows one to interpret the quadrupole coupling in terms of unbalanced p-electrons of the coupling atom. The electric field gradient around an atom which gives rise to the nuclear quadrupole coupling in most molecules is due primarily to an unequal filling of the valance p-orbitals in the coupling atom. The results of this model are summarized below;

$$\begin{aligned}(U_p)_x &= \left(\frac{n_y + n_z}{2} \right) - n_x \\(U_p)_y &= \left(\frac{n_z + n_x}{2} \right) - n_y \\(U_p)_z &= \left(\frac{n_x + n_y}{2} \right) - n_z\end{aligned}\tag{14}$$

where n_x , n_y , and n_z are the occupation numbers of their respective orbitals. $(U_p)_g$ is the unbalance of p-electrons along the corresponding 'g' reference axis. U_p is defined such that a positive value corresponds to a p-electron deficit along its reference axis and a negative value indicates a p-electron excess along the reference axis, thus

providing a sensitive tool in which to investigate the electronic environments within molecules containing quadrupole coupling atoms.

III.1 NOCl Spectrum

The hyperfine structure of nitrosyl chloride (NOCl) was first investigated by Millen and Pannel[21] using a low resolution microwave spectrometer. They obtained isotopic substitution data which was used to determine the molecular structure of the molecule (see Figure III.1). Chlorine quadrupole coupling constants were measured but hyperfine structure due to the nitrogen quadrupole was not resolved. Further studies on NOCl[22] at higher resolution obtained better values for the chlorine quadrupole and new measurements on nitrogen quadrupole coupling were made. These previous experiments utilized Stark modulated spectrometers, and since then, there have been substantial improvements in microwave technology and molecular beam techniques which resulted in orders of magnitude improvement in resolution and sensitivity of molecular measurements in the gas phase. The recent development of the pulsed beam Fourier transform technique (see Chapter II) has resulted in obtaining rotational spectra with 10-12 kHz linewidth resolution which can easily resolve the closely spaced $J = 0 \rightarrow 1$ hyperfine transitions in NOCl. The $J = 1 \rightarrow 2$ transitions for NOCl occur in the K-band of the microwave region and are out of range of the current PB-FTS experimental setup[23]. Measurements of the $J = 1 \rightarrow 2$ transitions were made with a molecular beam maser spectrometer which provides the highest resolution available for molecular spectroscopy with observed linewidths of 2-8 kHz. Measurements of chlorine and nitrogen quadrupole coupling were made using both techniques to obtain a high resolution low J data set for NOCl.

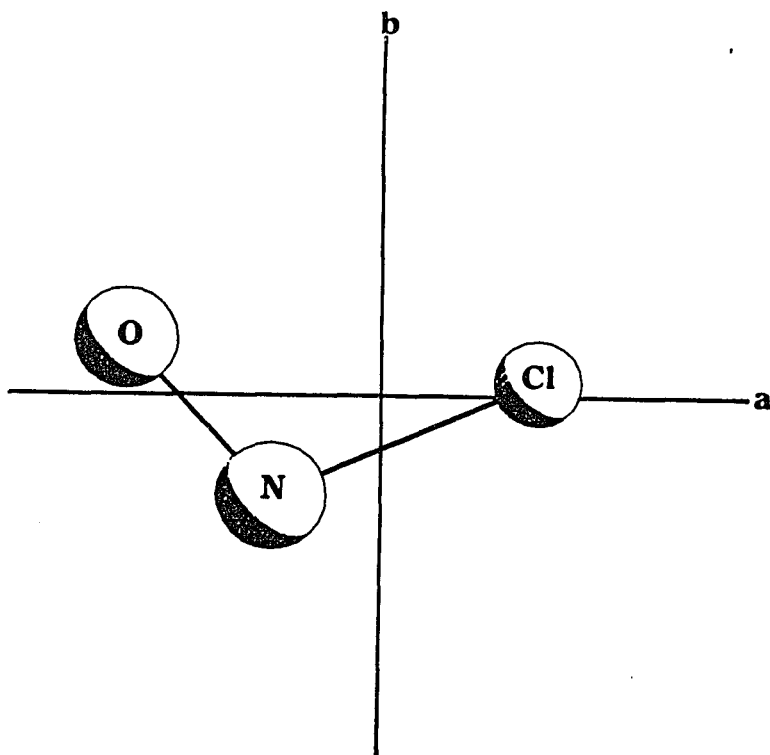


Figure III.1. Substitution structure obtained by Millen and Pannel[21]. $r_{NCl}=1.975(5)\text{\AA}$, $r_{NO}=1.139(12)\text{\AA}$, and $\angle ONCl=113.2(5)^\circ$

The nitrogen quadrupole coupling can be used as a useful indicator of structure and bonding in larger molecules containing a nitrosyl groups[24]. Accurate quadrupole measurements in simple compounds such as NOCl are important and can aid in the understanding of structure and bonding in nitrosyl groups of larger molecules.

III.1.i Synthesis of NOCl

Nitrosyl chloride was prepared by bubbling gaseous HCl through approximately 20 ml of nitrosylsulfuric acid[25] at room temperature under an atmosphere of dry nitrogen. The nitrosyl chloride was a yellowish orange gas which was condensed in a cold trap kept at approximately -20°C by a dry ice ethanol bath. The bubble rate was controlled to approximately 200 to 300 bubbles per minute. The reaction was allowed to progress for approximately 2 hours or until no more yellowish orange gas was observed. This usually resulted in 10 to 20 ml of relatively pure condensed NOCl.

III.1.ii Pulsed Beam Measurements

Seven hyperfine components of the $J = 0 \rightarrow 1$ transition were measured using using a Flygare-Balle type[23] PBFT microwave spectrometer (details of the spectrometer are given in Chapter II). These transitions were observed in the 11104 to 11127 MHz range with approximately 12kHz linewidth (f.w.h.m). An example spectrum of three of these transitions are shown in Figure III.2. NOCl was delivered to the spectrometer via a connection to the gas manifold system from a sample cell containing condensed NOCl in a dry ice ethanol bath. The NOCl was allowed to warm up to increase the vapor pressure of the sample to 10 to 20 torr, and then delivered to the manifold where it was diluted with 1.0 to 1.1 atmospheres of Ar gas. The resulting mixture was then pulsed through the nozzle at 0.5 Hz with backing pressures ranging from 0.5 to 1.1 atm. The free induction decay signals were averaged over several hundred gas pulses to improve signal to noise. The hyperfine transitions measured with the PB-FTS are shown in Table 1.

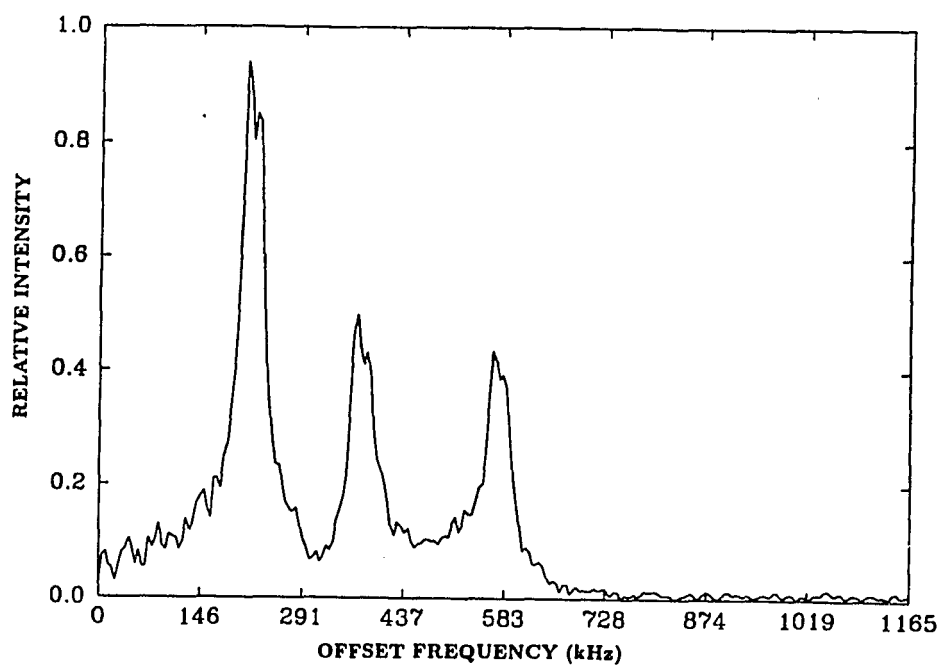


Figure III.2. FT spectrum of the $J = 0 \rightarrow 1$ hyperfine transition.
Stimulating frequency= 11104.587 MHz

Table III.1 Transition frequencies for the $J = 0 \rightarrow 1$, $K = 0$, and $\Delta I = 0$ measured on the PB-FTS for $^{35}\text{ClNO}$.

2I	2F	2F'	Meas.(MHz)	M-Calc.(MHz)
3	3	3	11104.010(2)	-0.007
5	5	5	11104.210(3)	-0.007
1	1	1	11104.370(9)	-0.005
1	1	3	11116.324(8)	0.020
5	5	7	11116.414(14)	0.021
3	3	5	11116.607(3)	0.006
5	5	3	11126.245(5)	-0.014
5	5	5	11104.210(3)	-0.007

III.1.iii Molecular Beam Maser Measurements

The transitions in the 22215 MHz to 22603 MHz range were measured on a molecular beam maser spectrometer[26] operated in the one cavity mode and are shown in Table III.2. The linewidths for the maser transitions were approximately 8kHz (f.w.h.m) and an example of three of these transitions is shown Figure III.3. Sample delivery to the maser was achieved by connecting the sample cell containing neat NOCl directly to the nozzle. The backing pressure of the NOCl ranged from 0.5 to approximately 1.0 atm and was controlled by the placement of the sample cell above a dry ice-ethanol bath. A continuous molecular beam was produced by the expansion of NOCl through a nozzle source with a 0.15 mm exit hole[27]. The beam was then collimated through a liquid nitrogen cooled trap followed by a 0.6 cm aperture placed 20cm down stream from the nozzle. The beam then passes through the quadrupole focuser region where a potential difference of up to approximately 15 kV was applied to alternate stainless steel rods. The large radial electric field gradient produced by the quadrupole focuses the molecules with positive Stark coefficients (usually molecules in upper states) along the symmetry axis of the focuser where the electric field gradient is zero. Molecules with negative Stark coefficients (usually molecules in lower states) are deflected away from the main part of the beam. The beam then enters a 10 to 20 cm long TM_{010} cylindrical microwave cavity. The stimulating frequency is then tuned to the desired transition frequency of the molecule which also corresponds to the cavity resonance mode.

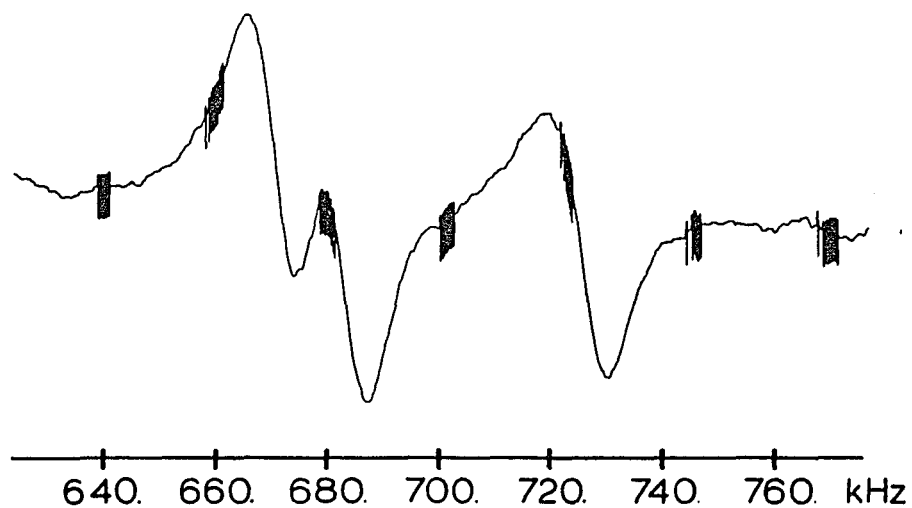


Figure III.3. First derivative maser spectrum relative to 22227000 kHz.

Table III.2 Transition frequencies for the $J = 1 \rightarrow 2$, $K = 0$, and $\Delta I = 0$ measured on the maser spectrometer for $^{35}\text{ClNO}$. Frequencies in MHz.

2I	2F	2F'	Meas.	M-Calc.
3	5	5	22215.324(6)	-0.014
3	1	3	22226.603(11)	-0.022
1	1	3	22227.414(6)	-0.001
1	5	9	22227.669(1)	0.010
1	1	5	22227.690(2)	0.015
1	5	5	22227.731(7)	0.009
1	3	5	22227.935(7)	0.013
1	5	5	22236.392(14)	-0.009
1	3	3	22236.597(6)	-0.009
1	3	3	22580.931(5)	0.010
1	7	9	22592.371(5)	-0.004
1	3	7	22592.987(4)	-0.003
1	5	1	22602.179(4)	-0.002

The stimulating frequency which induces molecular transitions in the TM_{010} cavity is produced by a phase-locked klystron. Signals are detected by a superheterodyne microwave receiver with a phase-locked local oscillator followed by lock-in detection near 200 Hz with a time constant of 15 s. The quartz crystal reference oscillator used earlier[27], was replaced by a variable frequency synthesizer (Vanguard Labs model SG-100C) operated near 100 MHz. The reference frequency was then slowly swept by a circuit external to the synthesizer. This modification allowed a wide range of frequencies to be scanned without the need for changing crystals. The stimulating frequency klystron is phase locked to a multiple of the synthesized reference frequency which is phase modulated by the 200 Hz oscillator. The modulation signal also serves as the reference for the phase-sensitive detector. The synthesized reference frequency is displayed on a frequency counter which is referenced to the 60 kHz radio transmission of WWVB, Boulder CO. Frequency markers are derived from the counter and are displayed on the chart recorder along with the output from the phase sensitive detector. A block diagram of the maser spectrometer is shown in Figure III.4.

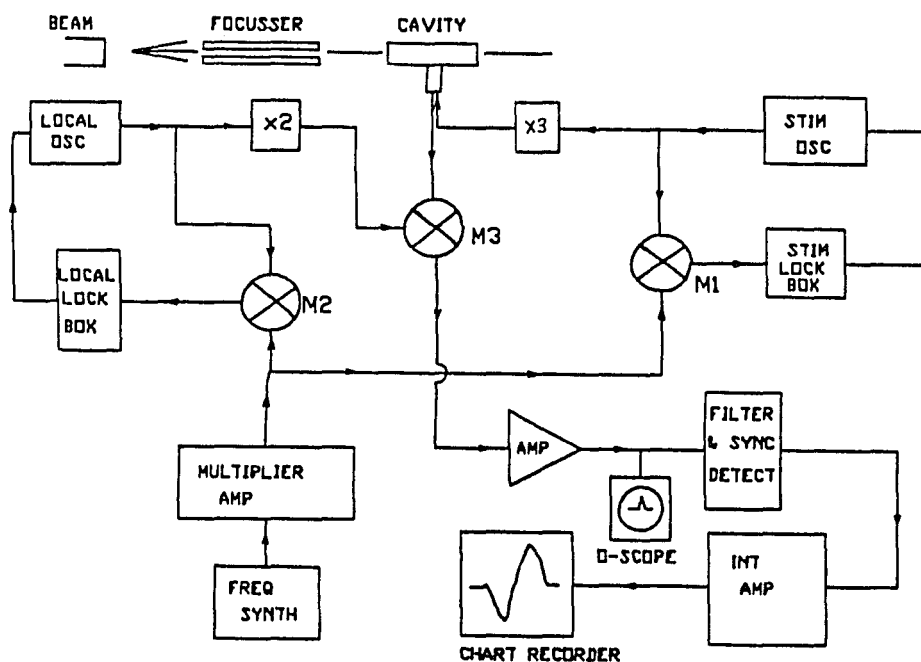


Figure III.4. Block diagram of maser.

III.1.iv Hyperfine Structure and Data Analysis

The hyperfine structure was analyzed using the coupled representation. The lab frame coupling scheme is $J + I_{Cl} = F_1$ and $F_1 + I_N = F$. J is the rotational angular momentum and I_{Cl} and I_N the chlorine and nitrogen spin angular momenta. The Hamiltonian matrix elements for the quadrupole hyperfine structure are

$$\begin{aligned}
\langle IJ'F|H_Q|IJF\rangle &= eQq_J(Cl)g(J)f(I_{Cl})(-1)^{J+I_{Cl}+F_1} \\
&\times SIXJ(F_1, I_{Cl}, J', 2, J, I_{Cl}) + eQq_J(N)g(J)f(I_N)(-1)^{J+I_{Cl}+I_N+2F_1+F} \\
&\times [(2F_1 + 1)(2F_1' + 1)]^{1/2}SIXJ(J', F_1', I_{Cl}, F_1, J, 2) \\
&\times SIXJ(F, I_N, F_1', 2, F_1, I_N)
\end{aligned} \tag{15}$$

Where q_J is the electric field gradient at the chlorine or nitrogen nucleus and is related to the components $q_{\alpha\alpha}$ along the principal axes, a , b , and c by the relation

$$q_J = 2 \sum_{\alpha} q_{\alpha\alpha} \frac{\langle J_{\alpha}^2 \rangle}{J(J+1)} \tag{16}$$

and

$$f(I) = \frac{1}{4} \left[\frac{(2I+1)(I+1)(2I+3)}{I(2I-1)} \right]^{\frac{1}{2}} \tag{17}$$

and

$$g(J) = \left[\frac{J(2J+1)(J+1)}{(2J-1)(2J+3)} \right]^{\frac{1}{2}} \tag{18}$$

Terms off-diagonal in the rotational states were not included in the analysis and matrices for each value of F for each rotational state were constructed and diagonalized. The rotational energies were described by :

$$H_{ROT} = AJ_a^2 + BJ_b^2 + CJ_c^2 - D_J(J^2)^2 - D_{JK}J^2J_a^2 \quad (19)$$

The differences between frequencies calculated with the above ‘first-order’ treatment and calculations including terms off-diagonal in rotational states were on the order of 3-4 kHz. The measured and calculated, best fit, transition frequencies are shown in Tables III.1 and III.2. The standard deviation of the fit was 14kHz. The deviations (last column, Tables III.1 and III.2.) between calculated and measured frequencies are slightly larger than experimental uncertainties for individual transitions, but including other interactions, such as spin-rotation interactions, did not significantly improve the standard deviations for the fits. The values for A , D_J and D_{JK} were determined more accurately in the earlier work of reference[28] since higher J transitions were measured. The previous values of reference 2, $A = 87374.46$ MHz, $D_J = 0.0063$ MHz and $D_{JK} = -0.0585$ MHz were used as fixed parameters in our analysis. The molecular parameters obtained here are in reasonably good agreement with the previous values, as shown in Table III.3.

Table III.3 Values of the molecular parameters obtained by fitting the observed transitions in Tables III.1 and III.2. Two standard deviations are in parentheses, $\sigma_{FIT} = 14 kHz$. Values in MHz.

Parameter	PresentResults	PreviousValues ^a
B	5737.70(6)	5737.69(3)
C	5376.32(6)	5376.31(3)
eQq _{aa} (Cl)	-49.05(4)	-49.18(35)
eQq _{bb} (Cl)	30.0(4.0)	29.46(20)
eQq _{aa} (N)	0.98(6)	1.0(4)
eQq _{bb} (N)	-4.78(22)	-4.8(2)

^a see reference [22]

III.2 ClF₃ Spectrum and Structure

The interhalogen compounds have a variety of interesting and unusual structures. The structure of ClF₃ is unusual when compared to other small molecules. Gas phase structures have also been obtained for ClF and ClF₅. Microwave spectroscopy[29] and x-ray diffraction work[30], carried out 37 years ago, obtained a planar, C_{2v} structure for ClF₃ with F-Cl-F bond angles slightly less than 90°. The basic T-shaped structure with 90° F-Cl-F bond angles is predicted by the VSEPR descriptions of molecular bonding. Even the observation of less than 90° F-Cl-F angles can be rationalized by the larger lone pair-bond repulsion effects. Accurate gas phase structural parameters and quadrupole coupling strengths can be obtained using microwave measurements. The electronic structure information from the quadrupole coupling combined with bond lengths and angles should be useful for *ab initio* electronic structure calculations on this molecule. In the previous microwave work[29], five groups of rotational transitions for ³⁵ClF₃ and ³⁷ClF₃ were measured in the 20-26 GHz range and fitted using a rigid rotor-first order quadrupole Hamiltonian. Some of the hyperfine structure was only partially resolved.

III.2.i Experimental

The ClF₃ spectrum was measured using the PB-FTS spectrometer which is described in detail in Chapter II. A commercial sample of ClF₃ (Air Products UN 1749) was used without further purification. In spite of the high reactivity of ClF₃, samples could be handled for short periods of time in a stainless steel system. Mixtures of 2% ClF₃ in argon at 0.5 atm pressure were pulsed into the Fabry-Perot

cavity of the spectrometer at a 1 Hz repetition rate. Signal-to-noise ratios ranged from 5 to 0.1 for a single gas pulse on the measured transitions.

Forty-two transitions for $^{35}\text{ClF}_3$ and 37 transitions for $^{37}\text{ClF}_3$ are listed in Tables A.I.1 and A.I.2 in Appendix A.I. Both Q -branches ($\Delta_J = 0$) and R -branch ($\Delta_J = 1$), b -dipole transitions were measured. All transitions that were observed with the PB-FTS had $K = 0$ for either the upper or lower state. This is probably due to the fact that the rotational cooling has substantially reduced populations in $K \neq 0$ states. This would imply efficient rotational cooling and beam rotational temperatures less than 10 K for rather mild expansion conditions.

III.2.ii ClF₃ Hyperfine Structure Analysis

The chlorine hyperfine structure was analyzed using the coupled representation with the total angular momentum $\mathbf{F} = \mathbf{I} + \mathbf{J}$. The nuclear spin $I = 3/2$ for $^{35}\text{ClF}_3$ and $^{37}\text{ClF}_3$ and the quadrupole coupling strengths were sufficiently large that Hamiltonian matrices for each F value were constructed and diagonalized. The Hamiltonian for rotational energies is given in equation (19) in section III.1.iv and the Matrix elements for quadrupole coupling have the form

$$\begin{aligned}
 \langle I'F | H_Q | IJF \rangle = & \\
 & 0.25eQq[(2I+1)(2I+3)(I+1)/I(2I-1)]^{1/2} \\
 & \times [J(J+1)(2J+1)/(2J-1)(2J+3)]^{1/2} \\
 & \times SIXJ(F, I, J', 2, J, I)(-1)^{J+I+F}
 \end{aligned}
 \tag{20}$$

where $eQq_J = 2eQ \sum q_{\alpha\alpha} \langle J_{\alpha}^2 \rangle / J(J+1)$. The differences between this diagonalization method and a ‘first-order’ treatment of the quadrupole coupling are on the order of 30 kHz for ClF_3 .

III.2.iii Data Analysis

A nonlinear least-squares fitting routine was used to obtain best fit values for A , B , C , D_J , D_{JK} , eQq_{aa} , and eQq_{bb} for both isotopic species of ClF_3 . The calculated transition frequencies and quantum number assignments are given in Tables A.I.1 and A.I.2. The parameters obtained are shown in Table III.4. The standard deviation for the fits are 17 kHz for both isotopomers. The distortion parameters D_J and D_{JK} were too small to be determined by the fitting procedure. Upper limits can be placed on D_J and D_{JK} of 1kHz and 10 kHz from the present data set.

The ratio of quadrupole coupling strengths for the two isotopes are $eQq_{aa} (^{35}\text{Cl}/^{37}\text{Cl}) = 1.2686$ and $eQq_{bb} (^{35}\text{Cl}/^{37}\text{Cl}) = 1.2684$. These are in agreement with the very precise ratio 1.268877 obtained from atomic beam resonance experiments[31] and provide indication of the accuracy of measurements and assignments.

Table III.4 Values of the molecular parameters obtained by fitting the observed transitions in Tables A.I.1 and A.I.2. Two standard deviations are in parentheses, $\sigma_{FIT} = 17\text{kHz}$. Units = MHz.

Parameter	$^{35}\text{ClF}_3$	$^{37}\text{ClF}_3$
A	13748.25(1)	13653.54(1)
B	4611.719(2)	4611.866(2)
C	3448.629(3)	3442.719(4)
eQq_{aa} (Cl)	82.03(3)	64.66(4)
eQq_{bb} (Cl)	65.35(2)	51.53(3)

III.2.iv Structural Analysis

The measured rotational constants were used to obtain better structural parameters for ClF_3 . The inertial defects $\Delta = I_c - I_a - I_b$ were found to be $\Delta = 0.19976 \text{ amu } \text{\AA}^2$ for $^{35}\text{ClF}_3$ and $\Delta = 0.19962 \text{ amu } \text{\AA}^2$ for $^{37}\text{ClF}_3$. These are typical values for chemically bound planar molecules and are attributed primarily to vibrational effects.

Since only one isotope of fluorine is available, obtaining a substitution structure is not feasible for this molecule. An 'effective' structure can be obtained[20] by fitting the observed rotational constants. If A , B , and C were fit simultaneously, the inertial defects would result in very large uncertainties. A preferred procedure[20] is to fit pairs of rotational constants, assuming a planar structure. The structural parameters are shown in Figure III.5.

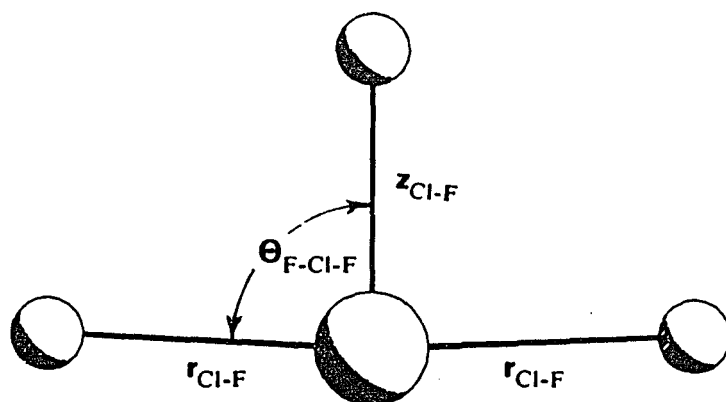


Figure III.5. Structural parameters for ClF_3 .

The results of fitting the structural parameters $Z_{\text{Cl-F}}$, $r_{\text{Cl-F}}$, and $\theta_{\text{F-Cl-F}}$ to A and B , or A and C , or B and C values are shown in Table III.5. The errors were much larger when fitting B and C . A weighted average of the fit results is shown in the bottom line of Table 5. These should be approximate to r_0 structural parameters, since substitution of ^{37}Cl for ^{35}Cl will not produce very large changes in vibrational zero-point energies.

Table III.5. Effective structure for ClF_3 calculations using least-squares fits to pairs of rotational constants for $^{35}\text{ClF}_3$ and $^{37}\text{ClF}_3$. Indicated errors are 2 standard deviations. These values should be very close to r_0 -type structural parameters since the effects of the Cl isotopic substitution on vibration-averaged coordinates will be small.

From	$Z_{\text{Cl-F}}(\text{\AA})$	$r_{\text{Cl-F}}(\text{\AA})$	$\Theta_{\text{F-Cl-F}}^\circ$
<i>A,B</i>	1.5984(5)	1.69990(6)	87.48(4)
<i>A,C</i>	1.5984(3)	1.70144(4)	87.48(2)
<i>B,C</i>	1.600(8)	1.6996(7)	87.7(6)
Avg ^a	1.5985(4)	1.70073(5)	87.48(4)

^aWeighted average, weighted by inverse of standard deviations.

III.2.v Discussion of ClF_3

The measured rotational constants and quadrupole coupling strengths are in very good agreement with earlier, less accurate, values obtained by Smith[29] using a completely different set of transitions. The earlier quadrupole coupling strengths were slightly smaller, possibly due to neglect of terms off diagonal in J . An electron diffraction study of ClF_3 was done recently[32] and the structural parameters obtained are in excellent agreement with the present work.

A planar, T-shaped structure for BrF_3 was obtained previously by Magnuson[33] using microwave measurements. The BrF_3 structure is very similar to the present ClF_3 structure. In both molecules, the axial X-F bond length is less than the equatorial X-F bond length. The F-X-F bond angles are both less than 90° , with an F-Cl-F angle of 87.5° for ClF_3 and an F-Br-F bond angle of 86.2° for BrF_3 .

III.3 Townes Dailey Interpretation of Quadrupole Coupling Data

From the results of the Townes-Dailey model of quadrupole coupling, summarized in Section III.1, one can discuss the electronic and bonding environments around the coupling atom in the molecule of interest. These results can also be used to compare the environments between molecules containing the same coupling atom.

The measured quadrupole coupling components for NOCl can be compared to values in other molecules. Metal nitrosyl complexes[34] show wide variations in electronic structure and MNO bond angle. The MNO or XNO bond angle and more detailed information about the electronic structure can be related to nitrogen nuclear quadrupole coupling strengths[24]. For linear bonding to NO the analysis is fairly simple, since quadrupole coupling tensor will be collinear with the NO bond axis and will be cylindrically symmetric (or very nearly cylindrically symmetric). The quadrupole coupling tensor for nonlinear XNO molecules will not be cylindrically symmetric and the principal axes will usually not be collinear with the NO bond.

Quadrupole coupling strengths for some typical molecules and ClNO are listed in Table 8. If these are interpreted in terms of the Townes-Dailey model[20], with n_x , n_y and n_z representing the approximate occupation of the valence atomic p orbitals on nitrogen, we can estimate $(U_p)_z = \left(\frac{n_x+n_y}{2} - n_z\right)$, the difference in occupation of parallel and perpendicular p orbitals with respect to the 'z' axis. The relation to the quadrupole coupling along the z-axis (a- axis for the listed molecules) is:

$$\begin{aligned}
eQq_{zz} &= 10\left(\frac{n_x + n_y}{2} - n_z\right)MHz \\
&= 10(U_p)_z MHz.
\end{aligned}
\tag{21}$$

For N_2 , $(U_p)_z \approx -0.25$. This difference is reduced to $(U_p)_z \approx -0.19$ for NO, presumably by additional electron density in p_x and p_y orbitals. This difference is further reduced to nearly zero for NNO. ClNO and FNO are both bent with bond angles of 113° and 110° respectively. CF_3NO is also bent and all three of these molecules have fairly large positive quadrupole coupling terms perpendicular to the molecular plane (eQq_{cc}). This indicates that the occupation numbers of the in-plane p-orbitals on nitrogen are much larger than the occupation number perpendicular to the molecular plane. In spite of the slightly different orientation of the a-axes for ClNO and FNO, the nitrogen quadrupole coupling strengths are very similar.

Table III.6. Nitrogen quadrupole coupling strengths for some typical molecules and $^{35}ClNO$ and values of $(U_p)_z$ obtained from eQq_{aa} values. Note that the z axis is taken to coincide with the a-axis for ClNO and FNO. Values in MHz.

Molecule	eQq_{aa}	eQq_{bb}	$(U_p)_z$	Ref.
N_2	-2.52	1.46	-0.25	[20]
NO	-1.86	0.93	-0.19	[35]
NN*O	-0.27	0.135	-0.03	[36]
ClNO	0.98	-4.78	0.10	
FNO	1.7	-4.8	0.17	[37]
CF_3NO	0.5	-6.0	0.05	[38]

The largest chlorine quadrupole coupling component in NOCl is negative and lies along the a-axis. Since the a-axis makes only an 18° angle with the N-Cl bond this would indicate a higher electron density in the chlorine p_z orbital along the N-Cl bond than in the perpendicular p_x or p_y orbitals. The difference, however, is significantly less than for Cl atom ($eQq = -110$ MHz) or Cl_2 molecule ($eQq = -109$ MHz) or even HCl ($eQq = -68$ MHz).

Measured values for the chlorine-35 quadrupole coupling for a few molecules are listed in Table III.7. For a chlorine atom $U_p = 1$, so one can estimate U_p for other molecules in Table III.7, using the quadrupole coupling strengths. U_p is 1.33 for ClF, indicating that n_z is less than the neutral atom value of 1. The fluorine atom appears to pull electron density away from the chlorine.

Table III.7. Chlorine (^{35}Cl) quadrupole coupling strengths and the unbalance of occupation numbers for the p electrons, U_p , for some molecules.

Molecule	eQq (MHz)	U_p	Ref
ClF	-145.87	1.33	[39]
Cl(atom)	-109.74	1	[41]
Cl_2	-108.95	0.99	[39]
ICl	-85.8	0.78	[39]
ClCN	-83.3	0.76	[42]
CH_3Cl	-74.75	0.68	[40]
HCl	-67.6188	0.62	[40]
ClF_3 (q_{bb})	65.36(3)	-0.62	present work
ClF_3 (q_{aa})	82.03(4)	-0.75	present work

For ICl, ClCN, CH₃Cl, and HCl, the bonding atoms apparently contribute additional electron density to $p_z(\text{Cl})$, resulting in $n_z > 1$ and a smaller unbalance. For ClF₃, however, the large positive values of eQ_q in the plane of the molecule and correspondingly large negative out of plane value ($eQ_{q_{cc}} = -147.4$ MHz) indicate a substantial reduction in occupation of the p orbital perpendicular to the plane of the molecule along with increased electron density in the in-plane p orbitals.

CHAPTER IV:**MICROWAVE MEAS. OF COBALT TRI-CARBONYL NITROSYL,
CYCLOPENTADIENYL COBALT DI-CARBONYL, AND
CYCLOPENTADIENYL MANGANESE TRI-CARBONYL**

Many transition metal complexes function as catalysts in reactions important in industry and biology. For example, cobalt is used in the catalytic production of esters and alcohols[43] in industry and plays an important role in the synthesis of vitamin B₁₂ in some animal species. Manganese is crucial in the conversion of ADP to ATP in metabolic processes as well as in photosynthesis[44]. Hence, understanding the roles transition metal complexes play in these reactions must include an accurate description of their overall geometry and electronic environments around the transition metal. Microwave spectroscopy provides data sensitive to these considerations free from solvent and crystal effects which can distort the true nature of the transition metal complex.

Until recently, obtaining high resolution molecular spectra of transition metal complexes was almost impossible. Due to their relatively large size (> 10 atoms) interpreting their spectra can be very difficult since large moments of inertia produce closely spaced and often unresolved rotational transitions. In addition, unresolved nuclear hyperfine structure caused by large quadrupole moments found in some transition metals often complicated the spectra so much that only estimates of molecular parameters could be obtained. Presented in this Chapter are the results of the first high resolution microwave study of Co(CO)₃NO, CpCo(CO)₂, and CpMn(CO)₃ using PB-FTS.

IV.1 Nuclear Quadrupole Coupling in $\text{Co}(\text{CO})_3\text{NO}$

The structure of cobalt tricarbonyl nitrosyl is shown in Figure IV.1. It is a C_{3v} oblate symmetric top and electron diffraction measurements of the gas-phase structure of $\text{Co}(\text{CO})_3\text{NO}$ were recently reported by Hedberg *et al.* [45]. Their structure indicated a linear Co-N-O group and was consistent with C_{3v} symmetry for the complex. The number of structural parameters obtained from electron diffraction data is much greater than from microwave measurements, especially for a symmetric top molecule. However, the accuracy relative to the equilibrium structure is not as high due to vibrational averaging effects and possible overlapping of interatomic distances in the radial distribution function. Therefore it is desirable to obtain both electron diffraction and microwave data for the structure determination of this type of molecule. This is particularly true for symmetric tops since only one rotational constant is obtained from the microwave data for each isotopic species.

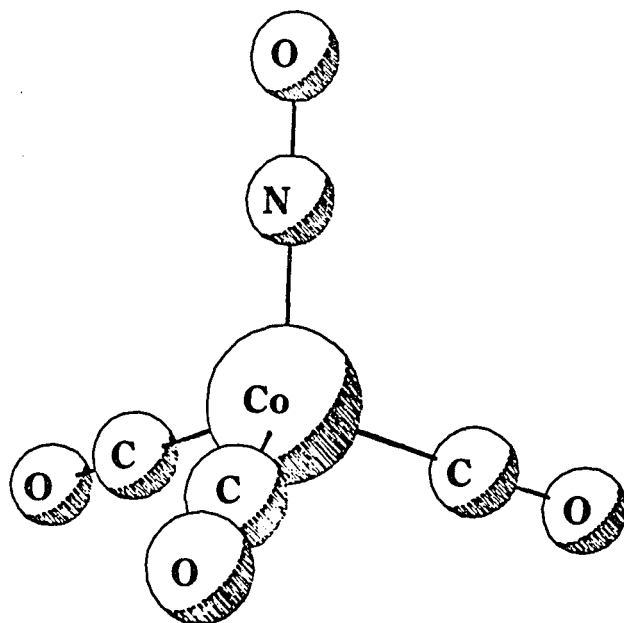


Figure IV.1. Structure of $\text{Co}(\text{CO})_3\text{NO}$ taken from [45].

An early attempt by others to measure the microwave spectrum of $\text{Co}(\text{CO})_3\text{NO}$ [46] 'failed to give conclusive results'. No transition frequencies were reported at that time. It is likely that the difficulties were due, in part, to the fairly large and complex hyperfine splitting due to ^{59}Co and ^{14}N quadrupole coupling.

The nitrogen quadrupole coupling strength in $\text{Co}(\text{CO})_3\text{NO}$ is slightly larger than the value for CpNiNO and is consistent with values observed for other linear M-N-O complexes. Since this is the first gas-phase ^{59}Co quadrupole coupling measurement, comparisons of this parameter with other gas-phase values are not possible. The measured value, however, should be useful for indicating valence shell p-electron distribution. The Co quadrupole coupling is sensitive to the electronic structure near the Co atom, and can be used as a test parameter for electronic

structure calculations. Electronic structure calculations on similar systems are currently being carried out, but are quite difficult due to the large basis sets required and relativistic effects associated with heavier nuclei.

IV.1.i Pulsed Beam Measurements

Microwave transitions in the 6-13 GHz range were measured using a pulsed beam, Fourier transform spectrometer described in detail in Chapter II. A 1-2% mixture of $\text{Co}(\text{CO})_3\text{NO}$ in Ar was pulsed at room temperature with a pressure behind the nozzle ranging from 0.4 to 0.7 atmospheres. The $\text{Co}(\text{CO})_3\text{NO}$ sample was obtained from Strem Chemicals (# 27-0500) and was used without further purification. The $J = 4 \rightarrow 5$ transitions were predicted to be near 10,791 MHz based on the model B, r_g structure of Reference [45]. The first $J = 4 \rightarrow 5$ transitions were found near 10,423 MHz. This may be an example of the 'shrinkage' effect in the electron diffraction data. A 3.7% increase in rotational constants would correspond to approximately a 1.8% shrinkage in coordinates if all coordinates are changed by the same fractional amount. With experimental conditions optimized, some transitions could be detected with a single beam pulse at 3 to 1 signal to noise. A few weak lines due to $J = 1 \rightarrow 2$ transitions near 4170 MHz were detected in our apparatus, but are not included in the data analysis.

The ^{59}Co nucleus has nuclear spin $I=7/2$ and nuclear electric quadrupole moment $Q=0.4$ barns[47] so many hyperfine transitions spread over many MHz were found. As a reference value, the nuclear electric quadrupole moment of ^{79}Br is $Q = 0.31$ barns [47]. The additional hyperfine structure splitting due to ^{14}N quadrupole coupling are also well resolved, resulting in rather complex hyperfine structure patterns.

IV.1.ii Rotational and Hyperfine Analysis

$\text{Co}(\text{CO})_3\text{NO}$ is an oblate symmetric top with C_{3v} symmetry. The $^{12}\text{C}^{16}\text{O}$ groups contain only bosons so the product of the nuclear spin wavefunction and rotational wavefunction must be totally symmetric with exchange of the CO groups. Since only the total $I=0$ symmetric spin function is possible for these CO groups, only $K=0$ or $K=3n$ rotational states exist. This simplified the analysis of the $J = 2 \rightarrow 3$ transitions, since only $K=0$ states could contribute to the spectrum. $K = 0$ and $K = 3$ states were observed for the $J = 3 \rightarrow 4$, and $4 \rightarrow 5$ rotational transitions.

The hyperfine structure was analyzed using the coupled representation. The lab frame coupling scheme is $J + I_{\text{Co}} = F_1$ and $F_1 + I_N = F$. J is the rotational angular momentum and I_{Co} and I_N the cobalt and nitrogen spin angular momenta. The Hamiltonian matrix elements for the quadrupole hyperfine structure are

$$\begin{aligned}
 \langle IJ'F | H_Q | IJF \rangle = & \\
 & (-1)^{J+I_{\text{Co}}+F_1} eQq_J(\text{Co})g(J)f(I_{\text{Co}}) \\
 & \times \text{SIX}J(F_1, I_{\text{Co}}, J', 2, J, I_{\text{Co}}) + C_{cc}(I_{\text{Co}} \cdot J) \\
 & + (-1)^{J+I_{\text{Co}}+I_N+2F_1+F} \times eQq_J(\text{N})g(J)f(I_N) \\
 & \times [(2F_1 + 1)(2F_1' + 1)]^{1/2} \text{SIX}J(J', F, I_{\text{Co}}, F_1, J, 2) \\
 & \times \text{SIX}J(F, I_N, F, 2, F_1, I_N)
 \end{aligned} \tag{22}$$

The field gradient in a given rotational state (J,K) for an oblate top is related to the cobalt or nitrogen electric field gradient along the c axis of the molecule by

$$q_J = q_{cc} \left(\left(\frac{3K^2}{J(J+1)} \right) - 1 \right) \quad (23)$$

and

$$f(I) = \frac{1}{4} \left(\frac{(2I+1)(I+1)(2I+3)}{I(2I-1)} \right)^{1/2} \quad (24)$$

and

$$g(J) = \left(\frac{J(2J+1)(J+1)}{(2J-1)(2J+3)} \right)^{1/2} \quad (25)$$

$$C_{Co}(J, K) = C_{aa} + (C_{cc} - C_{aa}) \frac{K^2}{J(J+1)} \quad (26)$$

The $K = 0$ data for $J = 2 \rightarrow 3$, $3 \rightarrow 4$, $4 \rightarrow 5$ and $5 \rightarrow 6$ transitions (Tables AII.1, AII.2, AII.3 and AII.4 in Appendix A.II) were fitted by constructing Hamiltonian matrices including quadrupole terms off-diagonal in rotational states. All data, including the above sets, were fitted with a ‘first-order’ treatment which did not include the terms off-diagonal in rotational states. Differences between these two types of calculations were less than 2 kHz for the listed transitions. The results

of fits to $K = 0$ transitions are shown in Table A.IV.5. The decrease in rotational constants can be used to determine the distortion constant $D_J = 0.17(8)$ kHz. This small value indicates rather high stretching force constants for this molecule.

Table IV.1. Molecular constants for $\text{Co}(\text{CO})_3\text{NO}$ obtained from least squares to the transition frequencies given in Appendix A.II. S.D. is the standard deviation for the fit. Values in MHz. Indicated errors are 2σ . The indicated J value is J_{lower}

Parameter	J=2	J=3	J=4	J=5	Fit Result
$A=B^a$.1561(7)	.1535(7)	.1503(4)	.1469(12)	.1590(4)
D_J	--	--	--	--	0.00017(8)
$eQq_{cc}^{59}\text{Co}$	35.37(8)	35.45(18)	35.79(16)	35.9(16)	35.14(30)
$DQ^{59}\text{Co}$	--	--	--	--	0.024(6)
$C_{cc}^{59}\text{Co}$	0.010(2)	0.008(2)	0.008(2)	0.007(6)	0.0085(22)
$eQq_{cc}^{14}\text{N}$	-1.57(7)	-1.53(9)	-1.65(6)	-1.63(14)	-1.59(10)
S.D.	0.011	0.009	0.008	0.014	

^a The number preceding the decimal point is 1042 for all of the indicated transitions.

The ^{59}Co quadrupole coupling strengths appear to be decreasing for the higher J transitions. We can fit the quadrupole coupling strengths to the equation:

$$eQq(J) = eQq_0 + DQJ(J + 1) \quad (27)$$

The parameters obtained are $eQq(^{59}\text{Co}) = 35.14(30)$ MHz and $DQ = 0.024(6)$ MHz for distortion of the quadrupole coupling.

The nitrogen quadrupole coupling values are reasonably consistent with an average value $eQq(^{14}\text{N}) = -1.59(10)$ MHz. This can be compared with the value $eQq = -1.22$ for CpNiNO [48]. The reported molecular parameters are based on $K = 0$ data only, since many more $K = 0$ transitions than $K = 3$ transitions were measured and assigned. The fits were significantly improved by including a spin-rotation constant C_{cc} for ^{59}Co . The observed value of 0.009 MHz is fairly large for a molecule with such small rotational constants.

$K=3$ transitions were observed and identified for $J = 3 \rightarrow 4$, $4 \rightarrow 5$ and $5 \rightarrow 6$. The measured frequencies and best fit values for the $K=3$, $J = 3 \rightarrow 4$ transitions are listed in Table A.IV.5. The molecular parameters determined from these transitions are also listed in Table IV.1. The ‘effective’ B value is

$$\begin{aligned} B_{eff} &= B_0 - D_{JK}K^2 - 2D_J(J_{upper})^2 \\ &= B_{eff}(K=0) - D_{JK}K^2 \end{aligned} \tag{28}$$

Comparison of this B_{eff} with the $K = 0$ value yields a very small distortion constant $D_{JK} \approx 0.6$ kHz. The quadrupole coupling strengths and spin-rotation constant are also quite close to $K = 0$ values, so no attempt will be made at this time to extract further parameters, such as C_{aa} from this data. The limited number of resolved $K = 3$ lines for other rotational transitions would not justify further analysis of these transitions at the present time.

IV.1.iii Summary

The absorption of transitions at 4B, 6B, 8B, 10B and 12B frequencies along with the observation of only $K = 0$ and $K = 3$ transitions confirm that this molecule is of C_{3v} symmetry, symmetric top. The fairly large deviation between the measured B value and that predicted from the electron diffraction data is somewhat surprising, particularly since the small measured D_J value (and D_{JK}) indicate a fairly rigid structure.

Solid state values of eQq (^{59}Co) in various transition metal complexes are tabulated in Lucken[49]. The values were obtained from nuclear quadrupole resonance and range from 32 MHz in $\text{NH}_4[\text{Co}(\text{NO}_2)(\text{NH}_3)_2]$ to 172 MHz in $[(\text{C}_5\text{H}_5)_2\text{Co}]\text{ClO}_4$. Our value of 35.1(3) MHz for $\text{Co}(\text{CO})_3\text{NO}$ is near the lower end of this distribution, indicating a fairly symmetrical electronic charge distribution around the ^{59}Co nucleus. The basic structure of $\text{Co}(\text{CO})_3$ is very nearly tetrahedral so that the observed quadrupole coupling must be due to the charge anisotropy produced by differences in bonding of CO and NO ligands. A popular text[50] suggests that NO is a 'three electron donor' while CO is a 'two electron donor', but it appears that this rule would overestimate the observed charge anisotropy for this complex.

The observed nitrogen quadrupole coupling eQq_{cc} (^{14}N) = -1.6(1) MHz falls between the value -1.22 MHz in Cp-Ni-NO [48] and the value -1.86 MHz for the free NO radical[51]. This would indicate a larger unbalance in p_z versus p_x or p_y electron density than for CpNiNO, but smaller than in NO or N_2 [48] (see Chapter III for discussion of unbalanced p-electrons and the Townes-Daily treatment).

IV.2 CpCo(CO)₂ : Hindered Rotor Spectrum

A gas phase electron diffraction study of CpCo(CO)₂ by Beagley *et al.* [52] provided values for many of the interatomic distances. The overall structure and symmetry was determined but the OC-Co-CO angle was not accurately determined and the Co-CO bond peak was not resolved. Hopefully, the combination of electron diffraction and microwave data will allow a better gas-phase structure determination. The structure shown in Figure IV.2 has the cobalt atom on the C_5 axis of cyclopentadiene and the carbonyls located such that the OC-Co-CO portion forms a C_{2v} structure. The present microwave data is consistent with this basic structure. Previous pulsed-beam measurements have been made on the related complexes Cp-NiNO [48] and Co(CO)₃NO [53]. Both of these cases are symmetric top molecules so only one parameter related to the structure is available from measurements on a single isotopomer. Since CpCo(CO)₂ is an asymmetric top, the three principal-axis moments of inertia are measurable and independent. The correlation between the ten fold barrier to internal rotation V_{10} and the A rotational constant is quite high. Other correlations are significant so rotational constants are not determined to the usual microwave accuracy, but the three to four significant figures should still provide useful structure information.

IV.2.i Experimental Considerations

Many hyperfine components for 15 rotational transitions in the 6-18 GHz range were measured with this spectrometer and the details are given in Chapter II. Most of the rotational transitions had ten or more components spread over a 10-30 MHz range. The larger splitting were assigned to internal rotation effects and the smaller splitting were interpreted as ⁵⁹Co quadrupole coupling hyperfine structure.

The experimental frequencies given in Table A.II.6 (in Appendix A.II) are averaged over the quadrupole splitting and in some cases, are also averaged over the internal rotation ' m '-state splitting.

The $\text{CpCo}(\text{CO})_2$ sample was purchased from Strem chemicals (product # 27-0550) and vacuum distilled before use. The sample was heated externally to increase the vapor pressure of $\text{CpCo}(\text{CO})_2$ and carried to a heated pulsed-expansion nozzle at the same temperature (28-32°C) by a flow of ultra pure argon. Backing pressures for the experiment ranged from 1 atmosphere down to 1/3 of an atmosphere. The molecular signal strengths were not very sensitive to the choice of backing pressure and strong transitions could be seen at a 3 to 1 signal to noise ratio for a single gas pulse.

IV.2.ii Data Analysis

The averaged and calculated transition frequencies are listed in Table IV.I. The hyperfine components due to the quadrupole coupling interaction of ^{59}Co atom were well resolved. The hindered internal rotation however, caused larger splitting in the rotational spectrum. In this section only the hindered rotor splitting are considered. The quadrupole components for a particular internal rotor transition were averaged to give approximate line centers for the internal rotor spectrum.

The Hamiltonian matrix for hindered rotation[54] was constructed in the $|JKm\rangle$ free-rotor basis and diagonalized. m is the quantum number for 'free' rotation of the 'top' (Cp-ring) relative to the 'frame' ($-\text{Co}(\text{CO})_2$). The hindered rotor matrix elements for a 10-fold potential barrier are given by:

$$\begin{aligned}
\langle JKm|H|JKm\rangle &= \frac{1}{2}(B+C)J(J+1) \\
&+ \left[A_z - \frac{1}{2}(B+C) \right] K^2 + Fm^2 - 2mA_zK
\end{aligned}
\tag{29}$$

$$\begin{aligned}
\langle JKm|H|J, K \pm 2, m\rangle &= -\frac{1}{4}(B-C)\{[J(J+1) - K(K \pm 1)] \\
&\times [J(J+1) - (K \pm 1)(K \pm 2)]\}^{1/2}
\end{aligned}
\tag{30}$$

$$\langle JKm|H|JK, m \pm 10\rangle = -\frac{1}{4}V_{10}
\tag{31}$$

where A_z is the moment of inertia of the framework alone, $A_z = \frac{\hbar^2}{2(I_z - I_\alpha)}$, and F is the reduced moment of the two parts of the molecule, $F = \frac{\hbar^2 I_z}{2I_\alpha(I_z - I_\alpha)}$. The 10-fold barrier gives matrix elements off-diagonal in m by 10 and the A -constant for the total I_z moment ($A = \frac{\hbar^2}{2I_z}$) was used as a fit parameter.

The selection rules[54-56] in the free rotor basis are $\Delta m = 0$ and $\Delta K = 0, \pm 2, \pm 4, \dots$. The $\Delta K = 0$ transitions will be stronger than those with $\Delta K = \pm 2, \pm 4, \dots$. Due to the spin statistics of the $\text{CpCo}(\text{CO})_2$ group (the carbonyls are bosons), there exists an additional restriction on the allowed states for $\text{CpCo}(\text{CO})_2$; only states with an even value of $|m - K|$ can exist. This is similar to restricting K_p values to even values for a rigid rotor where only bosons are exchanged by a C_2 rotation about the a -axis. This simplified the assignment of the spectrum

since the total number of observed transitions is reduced by this constraint. In our calculations of the hindered rotor energy levels the m -values were truncated at $m = 44$. At a 1 THz V_{10} barrier, this was sufficient to give truncation errors less than 1 kHz. At $V_{10}=40$ THz or greater the hindered rotor program yielded essentially rigid rotor energy levels with very small internal rotation splitting.

The fit parameters are given in Table IV.2. The fairly large deviations, (M-C) values in Table A.IV.6, and standard deviation values of the fit parameters are due, in part, to the correlation effects and in part, to averaging over many hyperfine components caused by the quadrupole coupling interaction of the cobalt atom. Since the hindered rotation is around the a-axis, the A rotational constant is strongly correlated with V_{10} . Going from a ‘free rotor’ to ‘high barrier’ resulted in A values ranging from 1440 MHz to 2170 MHz, respectively. The fit yielded a reasonable set of rotational constants A , B , and C , and a barrier to internal rotation, V_{10} , to be on the order of 0.3kJ/mol (0.82THz). These values for the parameters were obtained by fixing the top moment of inertia, $I_{\alpha} = 118.3 \text{ amu}\text{\AA}^2$. This value of I_{α} was calculated from the structural data obtained by the electron diffraction study of Beagley *et al.* [52]. By allowing I_{α} to be fit to the current data set, one obtains a slightly better (S.D=8MHz) overall fit. The fitted value, $I_{\alpha} = 122(3) \text{ amu}\text{\AA}^2$, is not much different, within experimental error, than the I_{α} obtained from the electron diffraction[52] study. Due to the small improvement in the fit standard deviation, we have chosen to fix I_{α} at $118.3 \text{ amu}\text{\AA}^2$ and report A , B , C and V_{10} as given in Table IV.2.

Table IV.2. Molecular constants for $\text{CpCo}(\text{CO})_2$ obtained from a least squares fit of the Hamiltonian to the observed transition frequencies. The reported error is 2σ . The quadrupole coupling results are in Table A.II.7. Errors for eQq are 4σ . The values are reported in MHz.

Parameter	Value	Error estimates
A	1625	± 20
B	1257	± 2
C	876	± 2
V_{10}	0.82 THz	± 0.20 THz
eQq_{aa}	12	± 4
eQq_{bb}	132	± 4

The structure was parameterized (shown in Fig. 2) with R_1 , the distance from the Cp plane to Co, R_2 the distance from Co to the carbonyl carbon atoms and θ , the OC-Co-CO angle. The structure of the Cp group is fixed at the electron-diffraction results[52] with C-C distance = 1.45 Å and C-H distance = 1.083 Å, giving $I_\alpha = 118.3 \text{ amu } \text{Å}^2$. R_1 , r_2 and θ are not linearly independent when used to determine moments of inertia since the Co atom is so close to the center of mass of the complex. R_1 was determined more accurately in the electron diffraction than R_2 or θ , so we also fixed R_1 at 1.735 Å, from the electron diffraction work. A least squares fit to our measured A , B and C values then yielded $R_2 = 1.69(5)$ Å and $\theta = 98(3)^\circ$. Since there is a fairly large uncertainty in A due to internal rotation effects and since θ depends almost directly on $A - B$, we report $\theta = 98(5)^\circ$ which

is in agreement with the electron diffraction result. Our present R_2 value is also in agreement with the electron diffraction result.

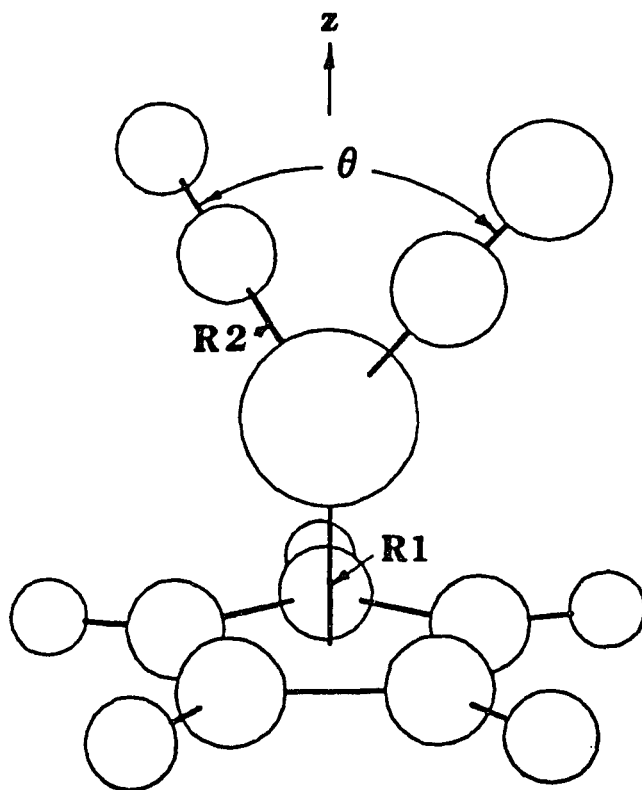


Figure IV.2. Structural parameters for $\text{CpCo}(\text{CO})_2$. $R_1 = 1.735 \text{ \AA}$, $R_2 = 1.69(5) \text{ \AA}$, $\theta = 98(5)^\circ$.

IV.2.iii Quadrupole Coupling

The ^{59}Co quadrupole splitting of the $J_K = 2_0 \rightarrow 3_0$, $3_0 \rightarrow 4_0$, $4_0 \rightarrow 5_0$ transitions were analyzed to obtain eQq_{aa} and eQq_{bb} . The $K = 0$ transitions were chosen because the relations between splitting and eQq values are nearly independent of internal rotation effects for $K = 0$ and $m = 0$ and are described reasonably accurately by a rigid-rotor hyperfine analysis[57]. The results of the least-squares fit to these transitions are shown in Table A.II.7. The standard deviation for the fit was only 70 kHz but uncertainties in eQq values (Table II) are given as 4 MHz due to possible small modifications of $\langle J_a^2 \rangle$, $\langle J_b^2 \rangle$ and $\langle J_c^2 \rangle$ by internal rotation effects. The eQq_{bb} quadrupole value is significantly larger than the value obtained from the relatively symmetrical $\text{Co}(\text{CO})_3\text{NO}$, but within the limits of other measurements by NQR in solid-state experiments.

IV.2.iv Results and Discussion

The present results for V_{10} barrier can be compared to earlier solid-state NMR studies[58] of hindered rotation of Cp in ferrocene, cobaltocene and ruthenocene. In those cases the barriers were a factor of 25 higher ranging from 7 to 9 kJ/mol. This could be due to additional interactions with neighboring molecules in the solid, or effects other than hindered rotation which modify NMR linewidths.

Listed in Table IV.3 are potentials for some V_3 and V_6 barriers as well as our current measurement V_{10} for $\text{CpCo}(\text{CO})_2$. The V_3 potentials for CH_3OH and CH_3COCl are relatively high, while the V_6 potentials for CH_3NO_2 and CH_3BF_2 are considerably lower. CH_3NO_2 and CH_3BF_2 were analyzed in the free rotor basis and provided reliable values for their respective V_6 barriers. Since these potentials fall in the 'low barrier' regime for hindered rotation, the elements off-diagonal by $m \pm 6$ in

the Hamiltonian matrix are small. The potential in CF_3NO_2 [56] is relatively higher so the $m \pm 6$ elements are larger, therefore more m states must be included in the diagonalization of the Hamiltonian. More mixing of the free rotor basis functions occurs for increasing values of the potential and also due to the asymmetry of the molecule. Since the multiplicity of the potential is larger for $\text{CpCo}(\text{CO})_2$ relative to CF_3NO_2 , m values up to $m = 44$ were needed. Although the standard deviation for the fit and the statistical errors in A, B, and C are fairly large compared with usual microwave values, they are still sufficiently accurate to provide useful structural information. We believe that these large deviations are due to ‘intermediate barrier’ effects of hindered rotation and the effects of large quadrupole coupling which are only partially analyzed in the present work. Another hindered motion of the CO groups could also cause shifts and splitting. We believe that the excellent fit to the quadrupole components (Table A.II.7) confirm the J , K , m assignments for those transitions.

Table IV.3. Some N -fold potential barriers (V_N) to internal rotation for various molecules.

Molecule	N-Fold	V_N (kJ/mol)
CH_3OH^a	V_3	4.477
CH_3COCl^b	V_3	5.422
CH_3NO_2^c	V_6	0.025
CF_3NO_2^d	V_6	0.311
CH_3BF_2	V_6	0.058
$\text{CpCo}(\text{CO})_2$	V_{10}	0.3

^a see: [59], ^b [60], ^c [61], ^d [62]

IV.3 Manganese Quadrupole Coupling in CpMn(CO)₃

Microwave measurements in the 4-14 GHz range were made using a PB-FTS type microwave spectrometer (see Chapter II). The spectrometer was configured in the same manner as it was for CpCo(CO)₂. A mixture of 1-2% CpMn(CO)₃ in argon was pulsed through a solenoid valve by heating a small sample cell containing solid CpMn(CO)₃ to 72°C while flowing argon through the cell. The cell and pulse valve were maintained at a constant temperature of 72°C to keep the valve from sticking. The CpMn(CO)₃ was purchased from Strem Chemicals (# 25-0390) and used without further purification. The $J = 5 \rightarrow 6$ transitions were predicted to be near 9918 MHz based on the rotational constant $B = 826.5$ MHz obtained from an earlier low resolution microwave experiment[63]. The first components of the $J = 5 \rightarrow 6$ transition were measured near 9930.6 MHz. Good signal to noise was obtained by using backing pressures ranging from 0.6 atm for the low J transitions to 0.4 atm for the high J transitions. When optimizing experimental conditions, 3/1 signal-to-noise ratios could be obtained for a single gas pulse for many hyperfine components of the $J = 3 \rightarrow 4$, $4 \rightarrow 5$ and $5 \rightarrow 6$ rotational transitions. Many components corresponding to $J = 7 \rightarrow 8$ and $J = 8 \rightarrow 9$ at 13,248 MHz and 14,904 MHz respectively were also measured, however, line centers could not be obtained from the data due to the large quadrupole interaction of the monoisotopic Mn nucleus $I=5/2$. The presence of the large quadrupole interaction produced closely spaced hyperfine components that could not be well resolved for the transitions involving high J values.

IV.3.i Data Analysis

CpMn(CO)₃ is a prolate symmetric top with C₃ symmetry, assuming a rigid structure for this molecule. The ¹²C¹⁶O groups contain bosons while the Cp

ring contains fermions. The symmetry properties of the product of the ‘two-top’ spin wavefunctions and the overall rotational wavefunction allow all the K-states to exist. Therefore, many hyperfine components of the rotational transitions were present in the spectrum. The measured frequencies and their assignments are listed in Tables A.II.8- A.II.12 in Appendix A.II. The 96 reported frequencies were fitted in a linear least squares fashion to a symmetric top Hamiltonian including terms for distortion and hyperfine structure due to the quadrupole coupling and spin rotation effects of the Mn nucleus:

$$H = H_{rot} + H_Q \quad (32)$$

where

$$H_{rot} = BJ^2 + (A - B)J_a^2 - D_J(J^2)^2 - D_{JK}J^2J_a^2 - D_K(J_a^2)^2$$

and

$$J^2 = J_a^2 + J_b^2 + J_c^2.$$

The Hamiltonian matrix elements for the quadrupole and spin- rotation interactions are:

$$\begin{aligned}
\langle IJ'F'|H_Q|IJF\rangle &= -0.25eQq_J \left(\frac{(2I+1)(2I+3)(I+1)}{I(2I-1)} \right)^{\frac{1}{2}} \\
&\times \left(\frac{J(J+1)(2J+1)}{(2J-1)(2J+3)} \right)^{\frac{1}{2}} \\
&\times SIXJ\{F, I, J', 2, J, I\}(-1)^{J+I+F} \\
&+ C_{Mn}(I_{Mn} \cdot J)
\end{aligned} \tag{33}$$

where

$$C_{Mn}(J, K) = C_{bb} + (C_{aa} - C_{bb}) \frac{K^2}{J(J+1)}.$$

The field gradient in a given rotational state (J, K) for a prolate symmetric top is related to the manganese electric field gradient along the a-axis of the molecule by

$$q_J = q_{aa} \left(\frac{3K^2}{J(J+1)} - 1 \right) \tag{34}$$

The quadrupole coupling was analyzed in the coupled representation $F = I + J$, where I and J are the spin angular momentum for the Mn and rotational angular momentum of the molecule respectively, F is the total angular momentum. All data were fitted by a 'first order' treatment of the quadrupole coupling interaction which did not include terms off diagonal in rotational states. The standard deviation

for the fit was 10 kHz. A second order analysis of the data was performed and the differences between these two analyses was on the order of a few kHz for the transitions listed in Tables A.II.8-A.II.12 in Appendix A.II.

The fit results to B , D_J , D_{JK} , eQq_{aa} , and C_{bb} are shown in Table IV.4. The rotational constant $B = 828.0333(3) MHz$ is comparable to an earlier experimental[63] value of $826.5(5) MHz$. The distortion parameters D_J and D_{JK} are very small but still well determined. D_K cannot be determined from the present data set. The distortion parameter D_J obtained in the present study can be compared to values obtained for other transition metal complexes in Table IV.5.

Table IV.4. Best fit parameters to the rotational hyperfine transitions listed in Appendix A.II. $\sigma_{FIT}=10$ kHz. listed errors are 2σ .

Parameter	Value
$B=C$	828.0333(6) MHz
D_J	0.088(9) kHz
D_{JK}	-0.04(3) kHz
eQq_{aa}	68.00(4) MHz
C_{aa}	-5.5(4) kHz

Table IV.5. Comparison of distortion parameters D_J for some transition metal containing complexes.

Molecule	D_J (kHz)
CpNiNO	0.08(2) ^a
Co(CO) ₃ NO	0.17(8) ^b
CpMn(CO) ₃	0.088(9)

^{a,b} See [48] and section IV.1 respectively.

The hyperfine constants $eQq_{aa} = 68.00(4)$ MHz and $C_{bb} = 5.5(8)$ kHz obtained from the fit are reasonable for a molecule containing an atom, such as Mn with large nuclear electric quadrupole ($Q = 0.4$ barns) and magnetic dipole ($\mu = 3.468$ nuclear magnetons) moments. Fitting both the C_{aa} and C_{bb} components of the spin-rotation simultaneously resulted in poorer fits, as did fitting only the C_{aa} component. The best fit to the data set was obtained from fitting only the C_{bb} spin-rotation component.

IV.3.ii Experimental Results

The basic geometry of CpMn(CO)_3 is shown in Figure IV.3. The Cp-ring has C_5 axis that is collinear with the C_3 of the Mn(CO)_3 group. The overall symmetry of the molecule is C_3 , however, the two moments of inertia I_b and I_c are equal, thereby producing a prolate symmetric top. This was confirmed by observing only transition frequencies at $6B$, $8B$, $10B$, $12B$, and $14B$. Since no isotopic substitution was performed, structural parameters were not directly obtained from the present study.

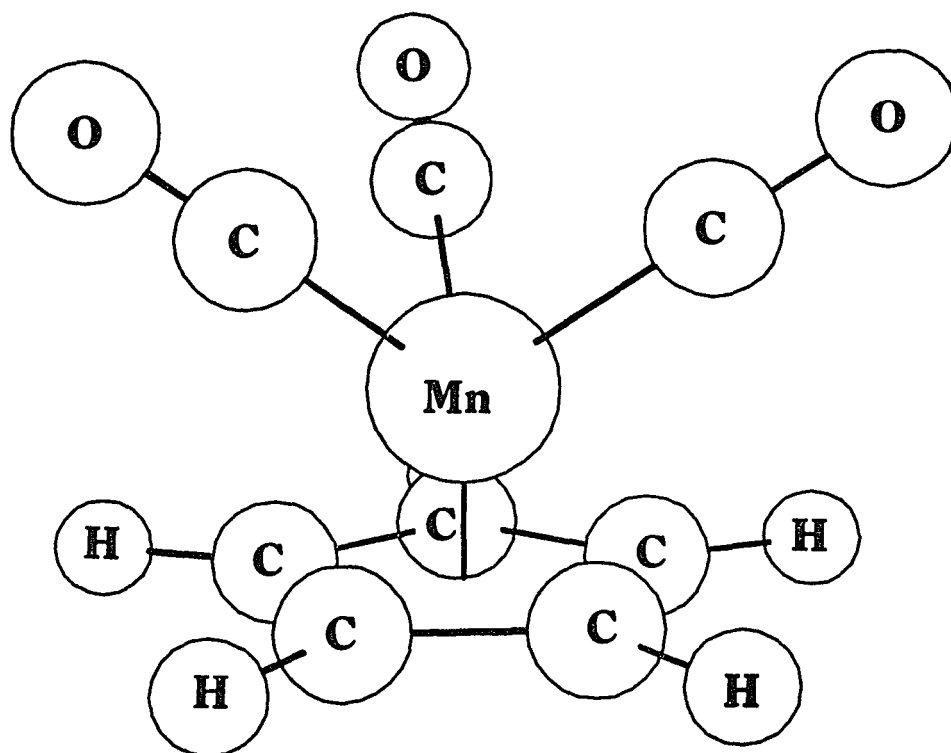


Figure IV.3. Structure of CpMn(CO)_3 .

The small distortion parameters D_J and D_{JK} shown in Table IV.4 indicate a fairly rigid structure for this molecule. A comparison of D_J values for CpNiNO and Co(CO)₃NO with CpMn(CO)₃ (see Table IV.5) show that these molecules are fairly consistent in their rigidity and undergo very little distortion due to rotation of the molecule.

This is the first gas phase measurement of eQq_{aa} for the manganese nucleus so comparisons to other eQq_{aa} values cannot be made. However, a solid state nuclear quadrupole resonance (NQR) study by Brill *et al.* [64] provided a value for $eQq = 64.29 \text{ MHz}$. It is apparent that their value corresponds to coupling along the symmetry axis of CpMn(CO)₃ which corresponds to the a-axis in the rotating frame. Comparing our $eQq = 68.00(4) \text{ MHz}$ with the solid state NQR measurement we see a good agreement between these two values. The 4 MHz difference could possibly be attributed to the perturbations induced by the lattice effects in the solid state whereas the gas phase measurement corresponds to the free molecule coupling. The large eQq for CpMn(CO)₃ can be attributed to the effects of the ligands, especially the Cp-ring. The Cp-ring is a five electron donor to the Mn and lies along the symmetry axis of the molecule. The Cp-ring appears to make a large contribution to the axial (a-axis here) electron density and therefore contribute significantly to the large field gradient and quadrupole coupling value $eQq = eQq_{aa} = 68.00 \text{ MHz}$.

In the present results, we report only the C_{bb} component of the spin rotation interaction. Parameter fits including the C_{aa} component were made and resulted in an improvement of the overall fit by 0.041 kHz. However, the value of the sixth parameter was $C_{aa} = -2.2 \pm 3.4 \text{ kHz}$ with the 2σ error limits being larger than the parameter. Often the values of the spin rotation components in symmetric tops are very similar. For example, spin rotation components C_{aa} and C_{cc} for nitrogen in

ammonia are 13.6 kHz and 11.4 kHz respectively, so one might expect that the C_{bb} and C_{aa} components in $\text{CpMn}(\text{CO})_3$ are also similar. When we examine equation (2), we note that C_{bb} can be determined from $K = 0$ data only, but to determine $(C_{aa} - C_{bb})$ we must use the $K \neq 0$ data. The quality of $K = 0$ data is usually better and more $K = 0$ transitions are accurately measured due to stronger signals so C_{bb} is much better determined than $(C_{aa} - C_{bb})$.

It is interesting to note the possibility of $\text{CpMn}(\text{CO})_3$ undergoing internal hindered rotation. Since the effects of hindered rotation are usually not seen for symmetric top molecules[65], except for symmetric tops in excited vibrational states, hindered rotation effects could not be observed for this molecule. In future isotopic substitution studies of $\text{CpMn}(\text{CO})_3$, it could be determined if this molecule undergoes internal rotation by substituting any one of the CO ligand atoms. By this substitution, the symmetry of the CO group would be destroyed thus changing the the moments of inertia to give a slightly asymmetric top . The resulting microwave spectrum would then reveal whether or not $\text{CpMn}(\text{CO})_3$ is hindered rotor.

An x-ray diffraction structure for $\text{CpMn}(\text{CO})_3$ was obtained by Berndt and Marsh[66]. Their averaged structure (corrected for libration effects), can be used to calculate rotational constants for comparison with the present results. Using their crystal structure data we obtain $A = 1053.8$ MHz and $B = C = 821.3$ MHz in excellent agreement with our measured value $B = 828.033$ MHz. This appears to indicate that there is very little change in structure of the molecule in a crystal, compared with the gas phase structure.

IV.3.iii Summary

Microwave measurements have been made for $\text{CpMn}(\text{CO})_3$ confirming it as a prolate symmetric top. The distortion parameters D_J and D_{JK} were well determined and comparison of D_J values with some other transition metal complexes indicate that these molecules are rigid in their geometries and undergo very little distortion. The hyperfine constants eQq_{aa} and C_{bb} are the first gas phase measurements for these parameters for Mn. The information obtained in the present study should provide additional insight into the nature of molecules containing transition metal complexes and should aid theoreticians in semi-empirical and *ab initio* calculations.

CHAPTER V:
MICROWAVE SPECTRA OF
CYCLOBUTADIENE IRON TRI-CARBONYL,
CYCLOHEXADIENE IRON TRI-CARBONYL,
AND BUTADIENE IRON TRI-CARBONYL

Iron containing transition-metal complexes are well known for their ability to catalyze various olefin reactions including hydrogenation, hydroformylation, isomerization, and polymerization[67, 68]. In this Chapter we look at three olefin containing iron carbonyl complexes and investigate their structural parameters in the gas phase using the PB-FTS technique. By determining how the structure and electronic properties of the olefin are altered by the metal-olefin bonding, one can better understand how the reactivity of an olefin is modified by its interaction with a metal atom. Therefore, precise structural measurements of metal complexes provide information on bonding which can be related to their electronic structure.

V.1 The Microwave Spectrum of Cyclobutadiene Iron tri-carbonyl

Cyclobutadiene is a particularly elusive compound. The compound is only stable as a ligand of low valent transition metal complexes such as iron in cyclobutadiene iron tricarbonyl. Cyclobutadiene iron tricarbonyl ($\text{CbFe}(\text{CO})_3$) was first synthesized by Emerson[69]. Since then, there have been a number of speculations and experiments on the structure of uncoordinated cyclobutadiene (Cb) and Cb

complexed as a ligand within a molecule (CbM). Infrared matrix isolation studies[70] indicate that Cb is slightly rectangular with alternating single and double bonds. When cyclobutadiene is substituted with bulky *tert*-butyl groups, x-ray crystallographic data[71] show that the substituted Cb is rectangular. However, the rectangular geometry is probably a direct consequence of packing effects and the bulky substituent rather than the nature of Cb itself. The rectangular geometry observed in the matrix isolation studies[70] can be explained by the *pseudo-Jahn-Teller effect* which leads to a change in geometry toward lower symmetry in systems that have sets of degenerate orbitals that are not fully occupied [72]. Therefore, it has been of interest, both experimentally and theoretically, to investigate the conditions for square *vs.* rectangular geometry.

Although several experimental attempts have been made to characterize the structure of Cb in $\text{CbFe}(\text{CO})_3$, none have clearly resolved this issue. Electron diffraction studies by Oberhammer *et al.* [73] and Davis *et al.* [74] have determined the basic geometry for $\text{CbFe}(\text{CO})_3$ which is shown Figure V.1. However, this technique is insensitive to asymmetries in the structure of the Cb ring. An earlier microwave study[75] indicates that $\text{CbFe}(\text{CO})_3$ is a symmetric top. However, this previous study reported signals with 20-60 MHz half width. These low resolution measurements were not capable of observing small asymmetry splitting which would result from any departure from a symmetric top (square Cb) structure. The high resolution available to PB-FTS will be useful in resolving the square *vs.* rectangular question of $\text{CbFe}(\text{CO})_3$.

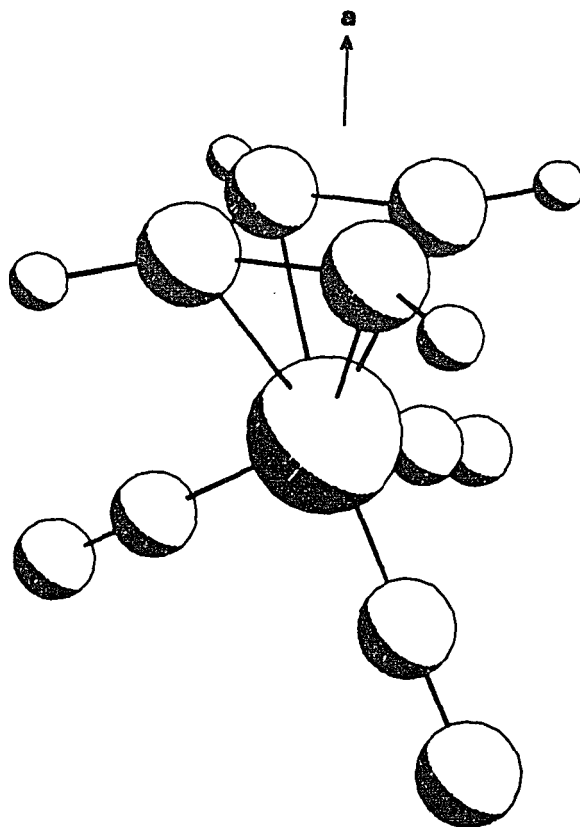


Figure V.1. Structure of $\text{CbFe}(\text{CO})_3$. Coordinates obtained from reference [73]. The a -inertial axis is collinear with the C_4 and C_3 axes of the cyclobutadiene and $\text{Fe}(\text{CO})_3$ respectively.

V.1.i Experimental

The $\text{CbFe}(\text{CO})_3$ was synthesized following the basic procedure outlined by Pettit and Henery[76]. Cis-3,4-dichlorocyclobutene (0.02 mol) (Fluka, Cat. # 35635) and iron nonacarbonyl (0.05 mol) (Strem Chemical, Cat. # 26-2640) were added to distilled benzene (20.0 ml), as a solvent, in a 100 ml round bottom flask. Reactants and products were handled in the inert atmosphere of a dry box. The

reactants were refluxed at 55°C with continuous stirring for 1.5 hours. The reaction mixture gradually changed from an orange to a dark green solution with a noticeable evolution of carbon monoxide gas. The contents of the vessel was then filtered and the residue was washed with pentane and solvent was removed from the filtrate by enhanced evaporation under vacuum to afford the product as a dark green oil. Further purification of the product was achieved by distillation under vacuum. The dark green oil which contained $\text{CbFe}(\text{CO})_3$ and iron pentacarbonyl with trace amounts of triiron dodecacarbonyl was then transferred to a sample cell which could be fitted to the pulsed valve of our spectrometer.

The pulsed valve and sample were maintained at a constant temperature of 60°C with argon flowing over the sample and pulsed through the valve as described previously in Chapter II. The spectrum was measured in the 4-16 GHz range. The $J = 4 \rightarrow 5$ transition was predicted to be near 9624 MHz based on the previous study[75]. Under high resolution we observed a signal at 9619.7 MHz with closely spaced components with less than 40 kHz separation. These components were assigned to the $J = 4 \rightarrow 5$ transition of $\text{CbFe}(\text{CO})_3$ with splitting due to centrifugal distortion. Corresponding components of the $J = 2 \rightarrow 3$, through $J = 7 \rightarrow 8$ transitions were measured and are listed with their respective assignments in Table A.III.1. Signal strengths for single gas pulses ranged from 3/1 (S/N) for low J transitions to 1/1 for higher J transitions. Weak FID signals were detected at 17315 MHz due to K components of the $J = 8 \rightarrow 9$ transition but were not included in the present analysis due to uncertainties in the line center measurements.

V.1.ii Results and Discussion

Spectroscopic parameters were obtained by fitting the measured frequencies in Table A.III.1 to prolate symmetric top transition frequencies given by

$$\nu = 2B(J + 1) - 4D_J(J + 1)^3 - 2D_{JK}(J + 1)K^2 \quad (35)$$

The parameter values obtained from this analysis are shown in Table V.1. Since $K=0$ and $K=1$ components were not resolved for $J = 2 \rightarrow 3, 3 \rightarrow 4, 4 \rightarrow 5$, and $5 \rightarrow 6$ transitions, the calculated frequencies for $K=0$ and $K=1$ were averaged and fitted to the corresponding observed line centers. The uncertainty of B , D_J , and D_{JK} obtained from these calculations is well within the expected precision of microwave measurements. These parameters are compared to those of the earlier study[75] in Table V.1. The high resolution Fourier transform method employed in this study has enabled us to obtain two orders of magnitude improvement in the B -rotational constant.

Table V.1. Best fit values for adjustable parameters obtained using equation 1 and data in Table A.III.1. The quoted errors are 2σ for the parameters and the $\sigma_{FIT} = 7.6$ kHz. Also shown are the results obtained from previous work [75].

parameter	present work	previous work
B	961.9856(8) MHz	962.41 MHz
D_J	0.184(8) kHz	0.41 kHz
D_{JK}	1.20(3) kHz	--

The centrifugal distortion parameter D_J is approximately half of the previously reported value[75]. The difference can be attributed to the ability to resolve the K components in the current study where as they were not resolved in the previous study. The previously measured transitions were broadened by 20 to 60 MHz half-width, thus skewing the actual line center measurements due to the unresolved K components.

D_J can be used as a measure of how strongly the Cb-ring is bound to the $\text{Fe}(\text{CO})_3$ group. To a crude approximation, $\text{CbFe}(\text{CO})_3$ can be modelled as a pseudodiatom where the Cb-ring and $\text{Fe}(\text{CO})_3$ groups are regarded as point masses. Since D_J is then a measure of the susceptibility to centrifugal distortion along this internuclear axis, the previous value of D_J (see Table V.1) would indicate a more weakly bound complex than the current measurements indicate. The distortion parameters observed for $\text{CbFe}(\text{CO})_3$ and other transition metal complexes[77 , 78, 79] are summarized in Table V.2. Unfortunately, there is no x-ray data for $\text{CbFe}(\text{CO})_3$ to compare with the current microwave results and older gas phase electron diffraction studies[73,74] give a wide range for the rotational constants calculated from their structural parameters; 934.70 to 969.85 MHz.

Table V.2. Comparison of distortion parameters for some other transition metal complexes with values for $\text{CbFe}(\text{CO})_3$.

Molecule	Distortion	Parameter
	$D_J(\text{kHz})$	$D_{JK}(\text{kHz})$
$\text{CbFe}(\text{CO})_3$	0.184(8)	1.20(3)
$\text{Co}(\text{CO})_3\text{NO}$	0.17(8) ^a	0.6
CpNiNO	0.08(2) ^b	2.70(6)
$\text{CpMn}(\text{CO})_3$	0.088(9) ^c	-0.04(3)
	$\Delta_J(\text{kHz})$	$\Delta_{JK}(\text{kHz})$
$\text{BuFe}(\text{CO})_3$ ^d	0.075(2)	0.16(1)

^a see Chapter IV

^b see [77]

^c see Chapter IV

^d see section V.4

$\text{BuFe}(\text{CO})_3$ = butadiene irontricarbonyl.

Δ_J and Δ_{JK} similar to the symmetric top D_J and D_{JK} .

There has previously been uncertainty whether the Cb ring is square or slightly rectangular when complexed[74]. The present results, indicate that the Cb ring is very nearly square when complexed to $\text{Fe}(\text{CO})_3$. A rectangular structure would make I_b and I_c different thus producing an asymmetric top spectrum. By modifying the electron diffraction coordinates[73] for the Cb ring and assuming no change in the $\text{Fe}(\text{CO})_3$ group, one can calculate the effects of a slightly rectangular structure for the Cb ring. By making a 1 mÅ difference in the lengths of the two

adjacent C-C bonds of the Cb ring, $B - C = 80$ kHz and results in an asymmetry splitting in the spectrum of 230 kHz for the $J = 3 \leftarrow 2$ transition. The observed splitting is 30 kHz for this transition and is due to the small D_{JK} value. Therefore, the vibrationally averaged structure of the Cb ring appears to be square to better than 1 mÅ. Other structural anomalies in $\text{CbFe}(\text{CO})_3$ can also be tested such as tilting the cyclobutadiene ring relative to the a -inertial axis. By calculating the effect of tilting the Cb ring by $\pm 2^\circ$, we can place an estimated value of $B - C = \pm 60$ kHz which would correspond to a 100 kHz asymmetry splitting in the spectrum. Therefore, we conclude that the Cb ring is vibrationally averaged to within less than $\pm 2^\circ$ of being perpendicular to the a -axis of the molecule. The overall structure of $\text{CbFe}(\text{CO})_3$ is shown in Figure V.1; the C_4 axis of the cyclobutadiene ring and the C_3 axis of the $\text{Fe}(\text{CO})_3$ are coincident with the a -molecular axis. The b - and c -axes are perpendicular to the a -axis making I_b and I_c equal. This symmetrical structure is consistent with the observed spectrum.

The eclipsing of one of the corners of the Cb ring with a carbonyl group and locking it into a fixed position would be detected only if the Cb ring was tilted by this interaction. However, if a rigid non-tilted, eclipsed structure was present in $\text{CbFe}(\text{CO})_3$, the moments of inertia would be the same as those observed in the present study. Therefore, a structure like this would still be consistent with the observed spectrum.

Finally, the possibility of hindered internal rotation of the cyclobutadiene ring relative to the $\text{Fe}(\text{CO})_3$ group cannot be ruled out. Hindered rotation effects in symmetric tops are not observed[80], since the energy levels in a symmetric top are perturbed by hindered rotation equally in each rotational state thus producing no observable splitting in the spectrum. Splitting could be produced by asymmetric

isotopic substitution and this might reveal whether or not $\text{CbFe}(\text{CO})_3$ undergoes internal rotation.

V.1.iii Summary

$\text{CbFe}(\text{CO})_3$ is shown to be a symmetric top molecule from the analysis of its high resolution microwave spectrum. Evidence has been given to indicate that the Cb ring has a square geometry in $\text{CbFe}(\text{CO})_3$. A non-tilting eclipsed structure cannot be distinguished from a staggered structure since the respective moments of inertia identical and consistent with the observed spectrum. Hindered internal rotation effects were not observed, however, evidence for such internal motion should be revealed by future isotopic studies.

V.2 Cyclohexadiene Iron tri-Carbonyl

In the 1970's, Cotton and coworkers [81] investigated a series of substituted cyclohexadiene iron tri-carbonyl compounds using X-ray diffraction. Results from this study yielded some structural parameters related to the cyclohexadiene ring itself as well as the $\text{Fe}(\text{CO})_3$ group. However, cyclohexadiene iron tri-carbonyl ($\text{C-hexFe}(\text{CO})_3$) unsubstituted does not form a crystal at room temperature and therefore structural data could not be obtained on the pure unsubstituted $\text{C-hexFe}(\text{CO})_3$. In 1989 Tam and coworkers [82] obtained X-ray data for $\text{C-hexFe}(\text{CO})_3$ in a crystalline matrix complex with thiourea. To date, this was the only known structural data on $\text{C-hexFe}(\text{CO})_3$. However, this study did not determine how much the thiourea affected the intrinsic gas phase structure for this molecule. By analyzing gas phase rotational constants for two isotopomers of $\text{C-hexFe}(\text{CO})_3$ and relating them to structural parameters of the molecule, the affect of the thiourea interaction with $\text{C-hexFe}(\text{CO})_3$ can be investigated.

A sample was obtained from Strem chemical (# 26-0850) and used without further purification. The liquid sample was placed in the hot source apparatus described in Chapter II and heated to 38 °C. This heat was sufficient to obtain a high enough vapour phase fraction of $\text{C-hexFe}(\text{CO})_3$ in an Ar carrier gas. The gas mixture was maintained at approximately 160 Torr backing pressure and signal to noise ratios of 20-30 to 1 were obtained for the ^{56}Fe species by averaging 50-100 gas pulse FID's. Rotational transitions for the ^{54}Fe species were measured in natural abundance by averaging several hundred to a thousand gas pulses.

V.2.i Microwave Spectrum and Analysis

Spectra obtained for ^{56}Fe and ^{54}Fe isotopes of $\text{C-hexFe}(\text{CO})_3$ contained a - and c - dipole R-branch characteristics of a near prolate asymmetric top. 76 transitions for $J=3$ up to $J=9$ and K_p up to 6 were measured for the ^{56}Fe species (see Table A.V.2). The a - dipole transitions were 2 to 3 times stronger than the c - dipole transitions. 14 a - dipole transitions were measured for the ^{54}Fe isotopomer (see Table A.V.3), which has 5.8 % natural abundance.

Both the ^{56}Fe and ^{54}Fe spectra were fitted to Watson's A-reduced Hamiltonian in the I' representation[83] including terms for quartic distortion,

$$H = H_{ROT} + H_d \quad (36)$$

where

$$H_{ROT} = AJ_a^2 + BJ_b^2 + CJ_c^2$$

and

$$H_d = -\Delta_J(J_a^2)^2 - \Delta_{JK}J^2 J_a^2$$

$$- 2\delta_{JK}J^2(J_b^2 - J_c^2) - \delta_K[J_a^2(J_b^2 - J_c^2) + (J_b^2 - J_c^2)J_a^2]$$

The resulting fit to A , B , and C and the four quartic centrifugal distortion parameters, Δ_J , Δ_{JK} , δ_K yielded standard deviations of 3.1 kHz for the ^{56}Fe and 0.5 kHz for ^{54}Fe isotopomer. The A and Δ_K constants were highly correlated in the rotational fit. Therefore, Δ_K was fixed at zero and was not determined by this data set. Measured and calculated transition frequencies are given in Tables A.III.2 and A.III.3 in Appendix A.III. The rotational constants and distortion parameters obtained from these fits are given in Table V.3.

Table V.3. Rotational and centrifugal distortion parameters obtained from least squares fits to frequencies in Tables A.III.2 and A.III.3 in Appendix A.III. listed uncertainties are 2σ

Parameter	$^{56}\text{C-hexFe}(\text{CO})_3$	$^{54}\text{C-hexFe}(\text{CO})_3$
A(MHz)	960.0298(4)	960.02(1)
B(MHz)	681.8343(2)	682.0245(6)
C(MHz)	659.3087(2)	659.4821(4)
Δ_J (kHz)	0.027(2)	0.030(2)
Δ_{JK} (kHz)	0.051(9)	0.05(2)
δ_J (kHz)	0.0086(8)	0.008(2)
δ_K (kHz)	-0.59(6)	-0.4(1)

V.2.ii Structural Parameters

From the X-ray data[82] summarized in Tables V.4 and V.5 (structure I) show that the orientation of the ligands to be the same as the numerous substituted cyclohexadiene analogs reported by Cotton and co-workers[81]. The unique CO ligand is oriented toward the open side of the diene and the cyclohexadiene ring is bent with the methylene groups situated out of the diene plane (see Figure V.2).

However, the X-ray coordinates of the C-hexFe(CO)₃ atoms show a large deviation from the expected x, z plane of symmetry and rotational constants calculated for this structure yield significantly different values from the observed microwave results.

Table V.4. Rotational constants (obsd) from the high-resolution microwave spectra of ⁵⁶Fe and ⁵⁴Fe C-hexFe(CO)₃ isotopomers compared with those calculated from the X-ray structure (I and II) and values calculated with optimized ligand orientations (III).

Parameter	obsd	I	II	III
A(⁵⁶ Fe)	960.030	972.704	972.644	960.025
B(⁵⁶ Fe)	681.834	680.594	679.719	681.828
C(⁵⁶ Fe)	659.309	664.298	664.583	659.301
A(⁵⁴ Fe)	960.020	972.710	972.650	960.025
B(⁵⁴ Fe)	682.024	680.780	679.906	682.030
C(⁵⁴ Fe)	659.482	664.475	664.583	659.490
σ (MHz)		8.655	8.654	0.007

Table V.5. Structural parameters describing the relative orientation of the C_6H_8 and CO ligands relative to the iron atom (see Figure V.2)^a

Parameter	microwave fit	X-ray data
α (deg)	71.9(3)	76.6
β (deg)	57.7(2)	52.0 ^b , 53.4
ΔX (Å)	0.860(4)	0.998

^a The microwave fit values were determined from a least squares fit to the measured rotational constants, with uncertainties reported as two standard deviations. ^b The plane of symmetry is not maintained in the thiourea complex so two different X-ray values were obtained.

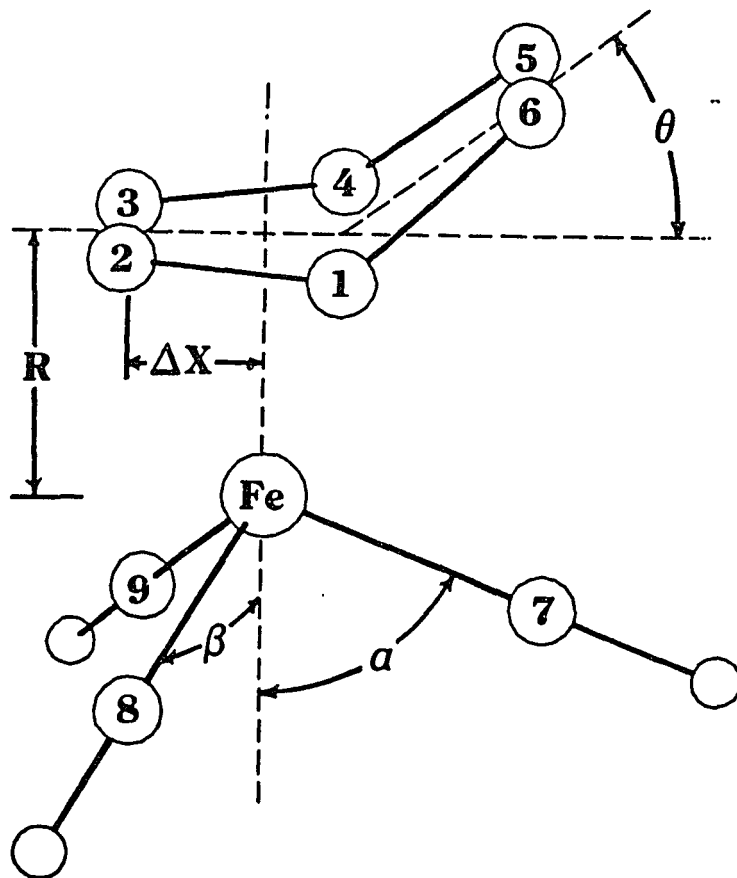


Figure V.2. Structural parameters used in the least squares fit to the isotopic rotational constants.

Principal moments of inertia and the corresponding rotational constants were calculated from the X-ray data[84] using a cartesian coordinate system established with the diene carbon atoms in the x, y plane and the z axis passing through the Fe atom (see Figure V.2). The X-ray study did not determine the hydrogen atom coordinates so standard sp^2 and sp^3 bond angles and bond lengths of $r(sp^2C - H) = 1.080 \text{ \AA}$ and $r(sp^3C - H) = 1.099 \text{ \AA}$ were used from the microwave results of [85, 86]. Elements of the inertial tensor were calculated and then diagonalized to obtain principal moments of inertia, rotational constants, and

the orientation of the principal inertial axis system. Calculations were carried out for the original X-ray structure (I), a symmetrized structure (II) in which a plane of symmetry was imposed on the X-ray structure by replacing (x, y, z) and $(x, -y, z)$ mirror coordinates with their average magnitudes. The results are compared with the microwave measurements in Table V.4. The calculated rotational constants are not very sensitive to the assumed hydrogen atom coordinates, for example, increasing all the diene C-H bonds by 0.01 Å results in a decrease in the A and B rotational constants by 0.4 and 0.9 MHz, respectively, and an increase in C by 0.2 MHz. The residuals suggest a loss of planar symmetry and further distortions in the molecular structure due to the interaction of the thiourea complex.

The structural parameters in Figure V.2 are sensitive to deformation from various interactions in the solid complex. By fitting various combinations of these structural parameters to the observed microwave data and attempts to adjust the metal-diene separation from the solid state value ($R = 1.626$ Å) did not significantly improve the value of the calculated rotational constants. However, when small adjustments in the orientation of the ligands around the central iron atom (see Tables V.6 and V.7) were made a significant improvement was made in the fit. Some selected interatomic distances and intramolecular angles for the optimized structure (III) are compared with both the original X-ray (I) and symmetrized X-ray (II) structures in Tables V.6 and V.7. The geometry and orientation of C-hexFe(CO)_3 in the principal axes is shown in Figure V.3. Figure V.3 shows that the structure is consistent with the observation of only $a-$ and $c-$ dipoles.

Table V.6. Selected interatomic distances (Å) from the X-ray structure (I and II) of C-hexFe(CO)₃ compared with those calculated with optimized ligand orientations (III).

distance	I	II	III
Fe-C1	1.799	1.799	1.799
Fe-C2	1.798	1.795	1.795
Fe-C3	1.794	1.795	1.795
Fe-C4	2.030	2.032	1.968
Fe-C5	2.104	2.102	2.125
Fe-C8	2.100	2.102	2.125
Fe-C9	2.034	2.032	1.968
O1-C1	1.140	1.139	1.139
O2-C2	1.140	1.144	1.144
O3-C3	1.142	1.144	1.144
C4-C5	1.409	1.416	1.416
C4-C9	1.398	1.398	1.398
C5-C6	1.507	1.503	1.503
C6-C7	1.540	1.538	1.538
C7-C8	1.501	1.503	1.503
C8-C9	1.423	1.416	1.416

V.2.iii Results

The microwave results are in agreement with the basic molecular structure obtained from the X-ray data [82]. However, the structure of C-hexFe(CO)₃ is deformed by various interactions with the thiourea complex. The large differences are due to angular deformation in the orientation of the ligands around the central iron atom as shown in Section V.2.ii. Comparing the angles C₁-Fe-C₂, C₁-Fe-C₃, and C₂-Fe-C₃ for the gas phase molecule (structure III) with the original X-ray structure (structure I, Table V.7) indicates that the CO ligands are distorted by

repulsive interactions with the thiourea resulting in a reduction of the carbonyl 'umbrella' angle of 2-3 °. The asymmetry of the X-ray data with respect to the $a - c$ plane, can be seen in Tables V.6-V.7.

From this analysis of the X-ray and microwave data it is clearly shown that the intrinsic gas phase structure of $C\text{-hexFe}(\text{CO})_3$ has been severely distorted in the thiourea complex. The microwave data is valuable in the sense of indicating the magnitudes of these differences as well as some of the inherent molecular structural parameters. The combination of both X-ray and microwave data will result in an overall better understanding of the structure of this complex than using either method independently.

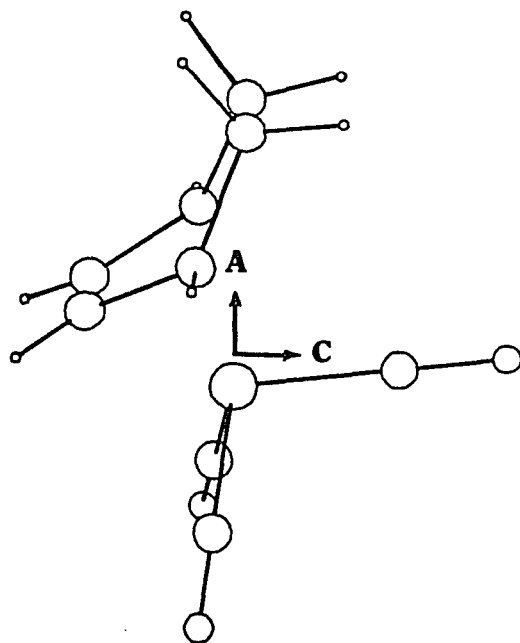


Figure V.3. Conformation and orientation of $C\text{-hexFe}(\text{CO})_3$ in the principal inertial frame as determined from microwave spectra.

Table V.7. Selected intramolecular angles from the X-ray structure (I and II) of C-hexFe(CO)₃ compared with those calculated with optimized ligand orientations (III).

angle(degree)	I	II	III
C1-Fe-C2	102.4	101.4	103.6
C1-Fe-C3	100.4	101.4	103.6
C1-Fe-C4	131.8	131.5	132.3
C1-Fe-C5	93.2	92.7	92.9
C1-Fe-C8	92.3	92.7	92.9
C1-Fe-C9	131.3	131.5	132.3
C2-Fe-C3	91.4	91.4	94.1
C1-Fe-C2	102.4	101.4	103.6

V.3 Butadiene Iron tri-Carbonyl Kraitchman Analysis

The butadiene iron tri-carbonyl ($\text{BuFe}(\text{CO})_3$) complex (shown in Figure V.4) is one of the earliest known π -bonded transition metal complexes and was described as early as the 1930's [87]. $\text{BuFe}(\text{CO})_3$ did not attract much attention since it was first thought to be a metallocycle structure with σ -bonding to the metal atom. The presently accepted π -bonded structure was proposed by Hallam and Pauson[88], based primarily on the stability of the complex. Experimental results on reactions with ozone and lithium aluminium hydride supported the π -bonded structure $\text{BuFe}(\text{CO})_3$. A large number of diene iron carbonyl complexes have been reviewed by Pettit and Emerson[89].

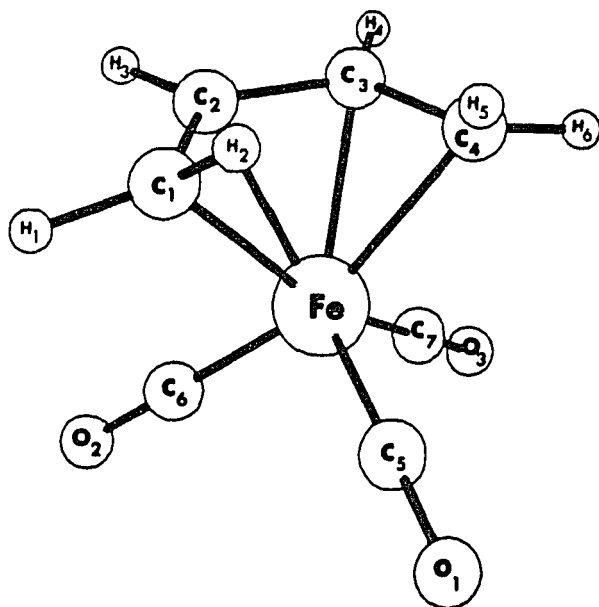


Figure V.4. Molecular structure and fitted parameters as determined from the Kraitchman analysis.

The microwave frequencies for the normal and isotopically labeled forms of $\text{BuFe}(\text{CO})_3$ have been reported[90, 91]. Transition frequencies were fitted to a Watson's A-reduced Hamiltonian including terms for quartic distortion (see equation (2) section V.3.i). The resulting rotational constants were then fitted to a molecular structure with the parameters shown in Figure 4 using a least squares fitting routine. An alternative method to obtain a molecular structure from this microwave data was pursued by using Kraitchman's equations for single isotopic substitution. The results obtained from Kraitchman's analysis can easily be interpreted in terms of the molecular structure and can be compared to the least squares fit analysis.

V.3.i Kraitchman's Equations and Molecular structure

From Kraitchman's equations one can obtain relative (relative to the normal isotopic species referred to as the parent molecule) absolute coordinates of an isotopically substituted atom within a molecule. A detailed derivation and description of Kraitchman's equations is given in Gordy and Cook[20] and shown here is a summary of those equations used in the analysis for $\text{BuFe}(\text{CO})_3$. The absolute relative coordinate a in the principal axis system is given by,

$$|a| = \left[\frac{\Delta P_a}{\mu} \left(1 + \frac{\Delta P_b}{I_a - I_b} \right) \left(1 + \frac{\Delta P_z}{I_a - I_z} \right) \right]^{1/2} \quad (37)$$

where $\mu = \frac{M\Delta m}{M+\Delta m}$. M is the total mass of the parent molecule and Δm is the isotopic shift in mass and

$$\Delta P_a = \left(\frac{1}{2} \right) (-\Delta I_a + \Delta I_b + \Delta I_c)$$

and $\Delta I_a = I'_a - I_a$. ΔP_b and ΔP_c can be generated from a cyclic permutation of a , b , and c in the above equations. These equations were used with the parent molecule of normally labelled $\text{BuFe}(\text{CO})_3$ as well as the triply substituted deuterium using the D_4 (terminal hydrogens substituted, see Figure V.4) as the parent molecule. The resulting a , b , and c coordinates can be used with the molecular plane of symmetry bisecting the butadiene and containing the unique carbonyl group C_5O_1 . Nearly enough structural parameters such as bond lengths and angles could be obtained to describe the overall geometry of the $\text{BuFe}(\text{CO})_3$ complex using only the Kraitchman's analysis. A fairly detailed description of the butadiene fragment could be obtained since coordinates for all but two of the atoms (H_3 and H_4) could be calculated. From the least-squares structural analysis, the bond lengths for the terminal protons H_1-C_1 and H_2-C_1 were constrained to be equal. However, from the Kraitchman's analysis, the H_1-C_1 bond length was found to be 0.007 Å longer than the H_2-C_1 bond.

The results of the Kraitchman's analysis are listed in Table V.8. Only the first four bond lengths and the first four angles were determined entirely from the Kraitchman analysis data. Other parameters required the Fe coordinates in the principal axis system from fit results as discussed below.

Table V.8 Comparison of interatomic distances and angles derived from the Kraitchman analysis with the Fe coordinates from the structural fit and comparable parameters determined entirely from the structural fit.

	Kraitchman	structural fit
Bond lengths Å		
H1-C1 ^a	1.0958(2)	1.087
H2-C1 ^a	1.089(5)	1.087
C1-C2 ^a	1.385(7)	1.385
C2-C3 ^a	1.409(1)	1.421
C1-Fe	2.1270(3)	2.127
C2-Fe	2.0870(2)	2.088
C3-Fe	2.0870(2)	2.088
H1-Fe	2.8230(1)	2.815
H2-Fe	2.6511(7)	2.650
Fe-C5	1.7706(0)	1.771
Fe-C6	1.7824(9)	1.783
Fe-C7	1.7824(9)	1.783
Bond angles °		
H1-C1-H2 ^a	120.8(3)	117.0
H1-C1-C2 ^a	112.1(4)	117.9
H2-C1-C2 ^a	118.6(2)	117.9
C1-C2-C3 ^a	118.4(2)	118.2
z-axis-Fe-C5	81.5(4)	82.4
z-axis-Fe-C6	52.2(4)	52.0
z-axis-H1-O2	20.5(2)	19.6
z-axis-Fe-O3	52.2(2)	52.0
xz- pl.-z-axis-O2	113.8(2)	113.3
xz- pl.-z-axis-O3	113.8(2)	113.3
Dihedral angles °		
H1-C1-C2-H3	11.3(3)	12.8
H2-C1-C2-H3	136.9(2)	136.5

^a For these parameters, the Kraitchman column values were determined entirely from the Kraitchman analysis; other parameters required data from the fit results or other measurements. pl.=plane.

The dihedral angles between $H_1-C_1-C_2-H_3$ and $H_2-C_1-C_2-H_3$ atoms were calculated by fixing the H_3 position in the carbon skeletal plane at 120° to the C_2-C_3 bond with a bond length of 1.090 \AA . These parameters also show differences in the terminal hydrogen coordinates as discussed above.

The structure of the $Fe(CO)_3$ portion of the molecule can be evaluated using the Kraitchman analysis as well. To accomplish this, the location of the Fe atom relative to center of mass for the molecule must be calculated using the fit results since the Fe atom was not isotopically labeled. The coordinates in the (a, b, c) frame for Fe obtained from the structural fit were used in the Kraitchman analysis. The Fe atom is so close to the center of mass that the uncertainties from the fit results should not introduce any significant additional error into these Kraitchman derived coordinates. Additional information on the terminal hydrogen positions can be obtained from Kraitchman using the D_4 substituted isotopomer as the parent molecule and the D_3 isotopomer for the single hydrogen substitution. The C_1-H_1 or the C_1-H_2 interatomic distances cannot be determined from these data sets. To calculate these distances one must assume a location for the Fe atom in the D_4 (a, b, c) coordinate system. The iron coordinates from the D_4 structural fits were used in a similar manner as for the normal isotopic Kraitchman analysis. Values for Fe- H_1 and Fe- H_2 distances were 2.8304 and 2.6623 \AA , respectively. When compared to values given in Table V.8, the agreement between these two distances in the D_4 and H_4 analyses is remarkably good. The results from the Kraitchman's analysis are in excellent agreement with the results from the structural fits and both sets are given in Table V.8.

CHAPTER VI:
MICROWAVE SPECTRUM, STRUCTURE,
AND DIPOLE MOMENT FOR THE HCCH-CO COMPLEX

The infrared spectrum of acetylene-carbon monoxide van der Waals complex was recently observed in the 3μ region by Marshall, Pritchard and Muentner[92,93]. The spectrum indicated a linear complex and later work[94] confirmed that the CO molecule was bound to the acetylene through a hydrogen carbon bond. A number of other linear OC-HX complexes were studied previously including OC-HF[95] , OC-HCl[96] , OC-HBr[97] , OC-HCN[98] and OC-HI[99] . In all cases hydrogen bonding to the carbon atom of CO was observed.

In the present work more precise values for rotation and distortion constants for HCCH-CO and HCCH- ^{13}C O were obtained and new results were obtained for the deuterated isotopomers HCCD-CO, DCCD-CO and DCCH-CO. All of the above isotopomers and isomers could be observed in a neon-helium ('first run neon') expansion gas as well as in argon, but, only the DCCH-CO isotopomer was *not* found in the argon expansion. This could be due to the low barrier for rotation of the acetylene molecule about its center of mass combined with a facilitation of this rotation in argon. It is expected the HCCD-CO isomer would be more stable than the DCCH-CO isomer since most hydrogen bonds are stronger for D than for H due to reduced 'zero point' vibrational motion of D relative to H.

VI.1 Experimental

All measurements were made using a Flygare-Balle type pulsed beam Fourier transform microwave spectrometer and the reader is referred to Chapter

II for experimental details of the PB-FTS system. Spectra for the five isotopic species of the HCCH-CO van der Waals complex were collected in the 4-18 GHz range and are shown in Table VI.1. Four of the isotopic forms of the HCCH-CO complex were observed by pulsing a 1-2% mixture of acetylene and carbon monoxide in 1 atm of argon buffer gas into an evacuated (10^{-6} - 10^{-7} torr) Fabry-Perot cavity. The DCCH- ^{12}CO isotopomer was observed using the same ratios of sample, but, neon was used as the carrier gas, since initial searches for this isotopomer in argon yielded no observable signals. The carrier gas was changed to neon and a signal belonging to this isotopomer was found at 7986.806 MHz . The other isotopomeric species were also observed in the neon buffer gas.

Signals for the HCCH- ^{12}CO and HCCH- ^{13}CO isotopomers were unusually strong for a complex consisting of one monomer having no permanent dipole moment (acetylene) and one having a small dipole of $0.1D$ (carbon monoxide). The signal-to-noise ratios were on the order of 100/1 per gas pulse for all of the rotational transitions. The ^{13}CO was purchased from Isotec Inc. (# 83-70003).

The deuterated forms of acetylene, HCCD and DCCD, were made by dropping a mixture of 30% H_2O and 60% D_2O onto solid CaC_2 under atmospheric pressure. The deuterated species were trapped out and further purification was accomplished by a trap-to-trap distillation under vacuum. A second method for synthesizing deuterated acetylene was utilized by placing several 'chunks' of CaC_2 in an airtight container along with several small ice cubes made from 30% H_2O and 60% D_2O solution. Once all reactants were placed inside, the container was sealed and evacuated. Upon warming, an increase in pressure was observed within the container. The sealing flange was equipped with a 'Swadge-lock' valve and could be fitted directly to our gas handling system on the spectrometer. Both methods

of producing deuterated acetylene worked equally well, however, the latter method is appealing since the sample is in ready to use form.

The signals for the deuterated species were not as strong as the HCCH- ^{12}CO ,- ^{13}CO isotopomers per gas pulse, signal- to-noise $\approx 20/1$. The DCCH- ^{12}CO complex signal strengths were considerably weaker even in neon, taking on average several hundred gas pulses to obtain reasonable signal- to-noise ratios.

Table VI.1. Measured rotational transitions ($J \rightarrow J + 1$) for the five isotopomeric forms of the HCCH-CO van der Waals complex. Frequency in MHz.

isotopomer	J	Frequency
HCCH-- ¹² CO	1	5589.316(4)
	2	8383.653(4)
	3	11177.613(4)
	4	13971.066(6)
	5	16763.886(5)
HCCH-- ¹³ CO	1	5540.405(4)
	2	8310.301(4)
	3	11079.824(2)
	4	13848.846(3)
	5	16617.261(4)
HCCD-- ¹² CO	1	5579.695(4)
	2	8369.245(4)
	3	11158.441(4)
	4	13947.154(5)
	5	16735.275(5)
DCCD-- ¹² CO	1	5318.598(3)
	2	7977.643(5)
	3	10636.379(4)
	4	13294.691(4)
	5	15952.488(6)
DCCH-- ¹² CO	2	7986.806(3)
	3	10648.554(3)

VI.2 Spectral Analysis

The acetylene-carbon monoxide spectrum is that of a linear rotor and contains no observable hyperfine structure. The presence of deuterium in some of the isotopomers brings about the possibility of measuring the deuterium quadrupole coupling in this complex. However, spectra containing deuterium exhibited very small splitting which were mostly unresolved and no attempt was made to obtain a quadrupole coupling constant for deuterium. All isotopomeric transition frequencies were fitted to

$$\nu = 2B(J + 1) - 4D_J(J + 1)^3 \quad (38)$$

using linear regression. The fit results to B and D_J are shown in Table VI.2 for all five isotopomers. All fits were well within the experimental accuracy expected from microwave measurements. Only two lines were measured for DCCH-¹²CO so the reported B value was obtained by using a D_J value obtained for the HCCD-¹²CO isotopomer. The B and D_J values determined in the present study for HCCH-¹²CO and HCCH-¹³CO species are in good agreement with those obtained by Marshall *et al.*[92, 94] using a molecular beam infrared technique. Their values are also listed in Table VI.2.

Table VI.2. Fit results for the five isotopomers of HCCH–CO compared with results obtained from references [92, 94].

isotopomer	$B(MHz)$	$D_J(kHz)$
HCCH-- ^{12}CO	1397.3705(6)	5.28(4)
HCCH-- ^{13}CO	1385.1425(8)	5.15(6)
HCCD-- ^{12}CO	1394.9635(3)	4.96(2)
DCCD-- ^{12}CO	1329.369(1)	4.31(2)
DCCH-- ^{12}CO	1331.1(1)	4.96(2) ^a
HCCH-- $^{12}CO^b$	1397.4(6)	5(2)
HCCH-- $^{13}CO^b$	1385.4(6)	9(2)

^a value fixed to the D_J value for the HCCD-- ^{12}CO isotopomer.

^b ground state constants obtained from references [92, 94].

VI.2. Structural Analysis

It is well known that van der Waals molecules undergo large amplitude motions about an equilibrium geometry, which, in the present case is linear. The observed moments of inertia will then be a function of the structural parameters induced by these vibrational motions. By taking into account these motions, the pseudodiatom model for van der Waals complexes can be modified to include the vibrationally averaged projections of the moments to yield an effective moment of inertia,

$$I_b^{complex} = \mu_{PD} R_{cm}^2 + \left\langle 1 - \frac{\sin^2 \theta}{2} \right\rangle I_b^{HCCH} + \left\langle 1 - \frac{\sin^2 \phi}{2} \right\rangle I_b^{CO} \quad (39)$$

where $\mu_{PD} = \frac{m_{HCCH}m_{CO}}{(m_{HCCH}+m_{CO})}$ and R_{cm} is the distance between the centers of mass of the monomer units. The bracketed quantities are the average values for the projections on the R_{cm} axis with vibrational motion about the linear equilibrium geometry. Figure VI.1 shows the structure of this complex. Note that the angle θ represents the vibrational amplitude, not an equilibrium value.

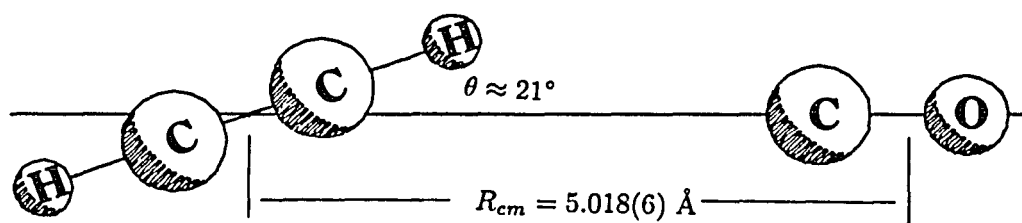


Figure VI.1. The vibrationally averaged structure obtained from the structural fit to the observed moments of inertia. The angle θ represents the vibrational amplitude of acetylene about R_{cm} .

Examining equation (39), we see that upon isotopic substitution of the monomer units there is a corresponding change in the centers of mass distance R_{cm} . To account for this in the fitting algorithm we would calculate the shifts in

the center of mass for the respective monomer units and then calculate the new centers of mass distance R_{cm} . The fitted results for each isotopomer are shown in Table VI.3. The reported value of R_{cm}^* in Table VI.4 is the corrected R_{cm} distance corresponding to the parent isotopic species HCCH- ^{12}CO . The angles θ and ϕ are the angles of the acetylene and carbon monoxide subunits respectively with R_{cm} . These were assumed not to be sensitive to isotopic substitution and no correction factors for this were introduced into the fitting algorithm.

The fit results to equation (39) in which R_{cm} , $\frac{\sin^2\theta}{2}$ and $\frac{\sin^2\phi}{2}$ are the fit parameters, are shown in Tables VI.3 and VI.4. The R_{cm}^* distance of 5.018(6) Å is in good agreement with the R_{cm} distance of 5.011 Å obtained by Marshall *et.al.*[92]. The parameter $\frac{\sin^2\theta}{2}$ yields a value of $\approx 21^\circ$ for the angle θ and is consistent with other linear hydrogen bound carbon monoxide complexes[95, 96, 97, 98, 99]. The parameter $\frac{\sin^2\phi}{2}$ was fixed to 0 since there was only one data point which was sensitive to this parameter, e.g. the HCCH- ^{13}CO isotopomer. Fits which included this parameter did not yield a statistically significant value for $\frac{\sin^2\phi}{2}$.

Table VI.3 Measured and calculated rotational constants obtained from the least squares fit to the observed moments of inertia. The parameter values are listed in Table VI.4. Values in MHz. The σ_{fit} was 0.583 MHz.

isotopomer	measured	calculated	M-C
HCCH- ^{12}CO	1397.370	1397.163	0.207
HCCH- ^{13}CO	1385.142	1385.336	-0.194
HCCD- ^{12}CO	1394.963	1394.448	0.515
DCCD- ^{12}CO	1329.684	1329.770	-0.086
DCCH- ^{12}CO	1331.225	1331.704	-0.479

Table VI.4. Parameter values from the fit to the observed rotational constants. Indicated uncertainties are 2 standard deviations.

parameter	value
R_{cm}^*	5.018(6) Å
$\frac{\sin^2\theta}{2}$	0.06(6)

VI.3. D_J , Force Constant and Binding Energy

Reasonably accurate and consistent values for the centrifugal distortion constant D_J were obtained from analysis of the spectra. These D_J values, combined with some structural data, can be used to calculate the stretching force constant k_s for changing the separation of centers of mass of the monomers (R_{cm}) and to estimate the binding energy. The normal expression for D_J for a diatomic molecule is modified[100] for a polyatomic linear dimer to give

$$D_J = \frac{4B^3}{\omega_s^2} \left(1 - \frac{B}{B_{HCC H}} - \frac{B}{B_{CO}} \right) \quad (40)$$

where B is the rotational constant of the complex and the stretching frequency (for the hydrogen bond) is such that

$$\omega_s^2 = \frac{4\pi^2 k_s}{\mu_{PD}} \quad (41)$$

Using these relations k_s values for the various isotopomers were calculated and listed in Table VI.5.

Table VI.5. Calculated k_s , ν_s , r_e and ϵ values derived from measured distortion constants D_J and R_{cm} values. The r_e values are the equilibrium centers of mass separation for the complexes.

isotopomer	$k_s(\text{mdyne } \text{\AA}^{-1})$	$\nu_s(\text{cm}^{-1})$	$r_e(\text{\AA})$	$\epsilon(\text{cm}^{-1})$
HCCH- ¹² CO	0.0171	46.4	5.0011	299
HCCH- ¹³ CO	0.0174	47.9	4.9788	301.5
HCCD- ¹² CO	0.0185	47.8	4.9078	311.5
DCCD- ¹² CO	0.0185	47.8	5.0006	323.4

The Lennard-Jones potential has only two adjustable parameters; the binding energy ϵ and the equilibrium internuclear separation r_e . This potential has been used, with pseudo- diatomic model for complexes to estimate the binding energy ϵ , given the derived force constant k_s and interpreting r_0 as the measured value for r_{cm} . First an 'equilibrium' rotational constant is obtained from the measured rotational constant for the complex B_0 using

$$2B_e = \frac{\nu_s}{18} - \left[\left(\frac{\nu_s}{18} \right)^2 - 4 \left(\frac{\nu_s}{18} \right) B_0 \right] \quad (42)$$

and

$$2\pi\nu_s = \omega_s$$

r_e is then the equilibrium value for R_{cm} obtained from B_e using the pseudo-diatomic model given earlier. The well depth is obtained from expanding the Lennard-Jones potential in a Taylor series about r_e and identifying the coefficient of the $(r - r_e)^2$ term with the calculated force constant to obtain an expression for the estimated dissociation energy ϵ

$$\epsilon = k_s r_e^2 / 72 \quad (43)$$

The values obtained are listed in Table VI.6. Our present results for k_s and ϵ are compared with results for other linear OC-HX complexes in Table VI.6. We note the expected trend of increasing binding energy and force constant, and decreasing r_e as the strength of the Lewis acid HX is increased.

Table VI.6. Comparison of k_s , r_e and ϵ for various hydrogen bound carbon monoxide van der Waals molecules. r_e is the equilibrium centers of mass separation.

complex	k_s (mdyne \AA^{-1})	r_e (\AA)	ϵ (cm^{-1})
HCCH-CO	0.0171	5.0011	299
IH-CO	0.0171	4.8925	286
BrH-CO	0.0330	4.5153	469
ClH-CO	0.0446	4.2260	569
FH-CO	0.108	3.047	987

VI.4 Dipole Moment

Stark plates were installed in the PB-FTS apparatus and details are given in Chapter II. The dipole measurement was made by tracking the $J=3, m=3 \rightarrow J=2, m=2$ Stark transition as a function of applied electric field,

$$\Delta\nu = \frac{\mu_{complex}^2 \epsilon^2}{B_{complex}} \left(\frac{5}{504} \right) \quad (44)$$

where $\mu_{complex}$ is the dipole moment of the complex, ϵ is the electric field across the Stark plates, and $B_{complex}$ is the rotational constant for the complex. Table VI.7 and Figure VI.2 show the dependance of $\Delta\nu$ on ϵ . The Slope of the plot in Figure VI.2 yields a dipole moment $\mu_{complex} = 0.333(2)$ D.

Table VI.7 Observed Stark shifts for HCCH-CO $J = 3, m_J = 3 \rightarrow J = 2, m_J = 2$ transition.

$\epsilon(\text{V/cm})$	$\nu(\text{MHz})$	$\Delta\nu(\text{MHz})$
0	8383.6526	0
178.737	8383.6608	0.0082
219.256	8383.6629	0.0103
252.881	8383.6662	0.0136
282.833	8383.6672	0.0146

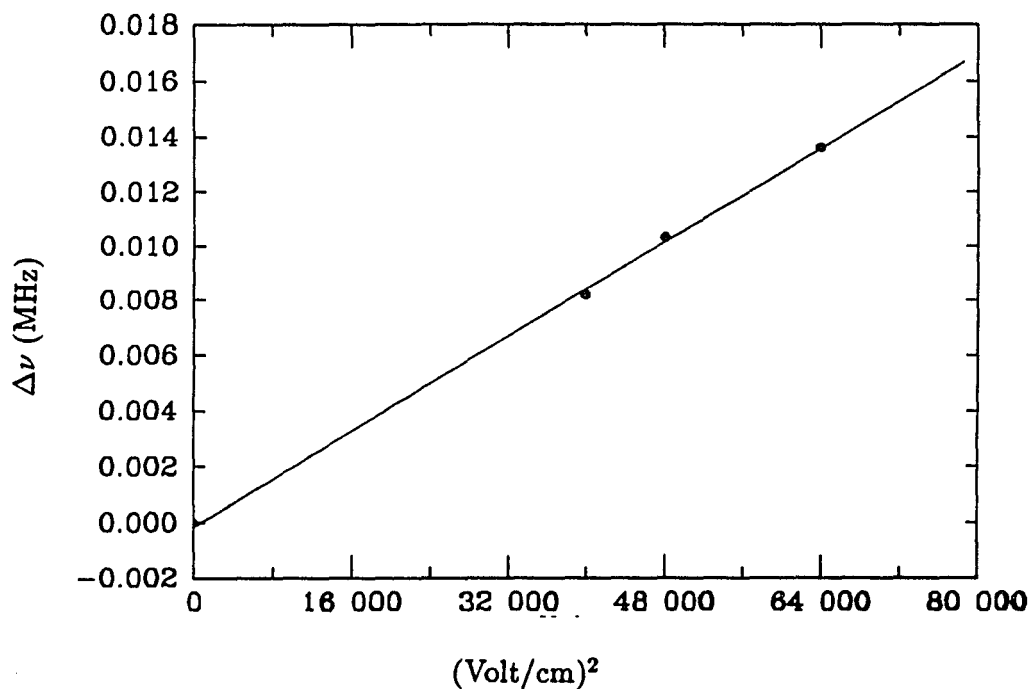


Figure VI.2 Plot of $\Delta\nu$ vs. ϵ^2 for the HCCH-CO complex.

VI.5. Summary

The lack of any observable signals for the DCCH-CO isomer in argon carrier gas was quite unexpected, since signals for the other isomers were easily observed with a single beam pulse. It is likely that most of the DCCH-CO isomers formed were isomerized to the lower energy HCCD-CO isomer in the presence of the argon. This would require a low barrier for rotation of the acetylene molecule within the complex. We may speculate that since argon forms stronger complexes with other

molecules than neon does, three-body collisions involving argon would facilitate the isomerization more readily than neon would. It would be helpful and interesting to have results of *ab initio* calculations on this complex with energies for various values for θ , the angle of rotation of acetylene relative to r_{cm} and to compare a calculated dipole moment for this complex.

CHAPTER VII:
SUMMARY AND CONCLUSIONS

Pulsed beam Fourier transform microwave spectroscopy was used to measure the ground state rotational, distortion and hyperfine constants for NOCl, ClF₃ and the transition metal complexes Co(CO)₃NO , CpCo(CO)₂ , and CpMn(CO)₃ . Ground state parameters for the iron containing complexes CbFe(CO)₃ , C-hexFe(CO)₃ , and BuFe(CO)₃ were also measured using this technique as was the weakly bound HCCH-CO complex. The versatility of this technique has been clearly demonstrated by the varied list of molecules studied here. The experiments presented here have been successful in obtaining new and important structural and nuclear hyperfine information in the gas phase for these compounds as well as establishing it as a viable technique in which to study complex molecules like transition metal complexes.

The spectra obtained for NOCl and ClF₃ provide the first high resolution data set for transitions involving low J rotational states. More precise measurements for the nitrogen quadrupole coupling in NOCl were obtained and comparisons to other 'simple' nitrosyl compounds were made using the Townes-Dailey interpretation of nuclear quadrupole coupling data. Quadrupole coupling data for Cl in ClF₃ were also interpreted using the Townes-Dailey model and more precise gas phase structural information was also obtained from the two isotopic spectra of ³⁵Cl and ³⁷Cl.

High resolution gas phase spectra were obtained for complexes involving cobalt and manganese. New data relating to the structure of these compounds and the first gas phase measurements of cobalt and manganese nuclear quadrupole coupling in these complexes were obtained from the data. $\text{CpCo}(\text{CO})_2$ was found to be a hindered internal rotor with a moderately low barrier to internal rotation of $0.82(20)$ THz (0.3 kJ/mol) estimated from the data. The complication of the large quadrupole moment for Co and hindered rotation precluded a more precise determination of this parameter. The possible hindered rotor nature of $\text{CpMn}(\text{CO})_3$ can not be determined from this data set since hindered rotation effects are not seen for symmetric top spectra.

The iron containing complexes provided new structural information on the interaction of conjugated diene systems with the transition metal iron. Cyclobutadiene was found to be square when complexed to the $\text{Fe}(\text{CO})_3$ as opposed to rectangular as once postulated. Cyclohexadiene and butadiene subunits were found to be bonded to $\text{Fe}(\text{CO})_3$ in a *pi di - sigma* type fashion rather than in the conjugated sense of a planar butadiene subunit. There were no significant observable hindered rotation effects in the spectra for these complexes indicating a fairly high barrier to internal rotation of the respective conjugated diene subunit relative to the tricarbonyl group.

Ground state vibrationally averaged structural parameters for the HCCH-CO weakly bound complex were determined from the microwave data. The structure was found to be averaged over a linear equilibrium geometry with one of the hydrogens of the HCCH bound to the carbon of the CO subunit. Force constants and stretching frequencies were obtained from the analysis of the distortion constant

D_J . A binding energy of 300 cm^{-1} was estimated from this data as well. Interesting intermolecular dynamics were observed for this complex when the deuterated isotopomers were studied. An apparent facilitation of the interconversion between the hydrogen and deuterium bound species of the complex was found to occur more readily in an argon carrier gas than in a neon carrier gas. A dipole moment of 0.333 D was also obtained from the stark experiment and is comparable to a value obtained simultaneously by the Gutowsky group [101] of 0.3112 D.

VII.1 Future Directions

As was stated in Chapter II the only real limitation of the PB-FTS technique is the ability to deliver a sample through the pulsed valve intact into the Fabry-Perot cavity. Advances such as the hot source and the incorporation of the Stark plates have demonstrated the feasibility of adapting the PB-FTS technique to new experimental challenges. There still remains much work to be done with the transition metal complexes and presented here are the foundations in which future studies may be based. The sample handling techniques learned here will provide the investigator with valuable information and tools in which to successfully measure spectra of the next transition metal challenge, hydrides. Transition metal hydride complexes are very unstable and reactive species and will require novel sample handling techniques and the inevitable design or radical modification of existing pulsed nozzle sources to accommodate their unstable nature. Some preliminary testing of new nozzle designs made from Teflon material have already been made with some success. An attempt to measure a $\text{HMn}(\text{CO})_5$ rotational transition was made already, but the sample life in the current spectrometer configuration was too short to have made an effective search for such a transition.

Other high temperature species may be measured using PB-FTS by modifying the new designs of today's fuel injectors used in the automobile industry. These fuel injectors can withstand very high operating temperature and could be used in the study of high temperature species and may even be used in forming radicals in high enough concentrations. Since the exit nozzle of these fuel injectors have four 'pin-holes' the amount of mass flux per pulse may be high enough for the subsequent generation of radicals while retaining the properties of supersonic expansions. One of these fuel injectors has been modified in our lab already and the signal arising from the Ar-HCl complex has been detected with greater than 20 to 1 signal to noise ratios thus showing the retention of free jet expansion properties. Incorporation of the fuel injector may significantly improve experiments requiring significant populations of these hard to get species like radicals.

Through the course of these experiments, unique situations and questions have arisen concerning the experimental data. More often these questions can be queried by either *ab initio* or semiempirical studies. The knowledge obtained from experimental studies can be used to formulate new ideas for theoretical studies and also to guide the modification of existing theories in their continual development. An *ab initio* study [102] of the HCCH-CO complex is one example of the interaction of theory and experiment. The future will see more and more of such interactions of theory and experiment and perhaps the modern day experimental spectroscopist will also have to be a competent theoretician as well.

APPENDIX A.I:
CF₃ TRANSITION FREQUENCIES

Table A.I.1 Measured and calculated (least-squares fit) transition frequencies for $^{35}\text{ClF}_3$. Frequencies in MHz. The standard deviation for the fit is 17kHz. Units in MHz.

J_{K_p, K_o}	2F	$J'_{K'_p, K'_o}$	2F'	Meas.	M-Calc.
1 _{1,1}	5	2 _{0,2}	5	6859.947(8)	-0.010
1 _{1,1}	1	2 _{0,2}	3	6863.782(7)	0.022
1 _{1,1}	3	2 _{0,2}	5	6876.331(9)	0.021
1 _{1,1}	5	2 _{0,2}	7	6883.525(8)	0.003
1 _{1,1}	1	2 _{0,2}	1	6887.322(8)	0.017
1 _{1,1}	3	2 _{0,2}	3	6893.172(10)	0.011
1 _{1,1}	3	2 _{0,2}	1	6916.707(4)	0.002
1 _{0,1}	1	1 _{1,0}	1	10242.282(3)	-0.002
1 _{0,1}	3	1 _{1,0}	1	10279.189(4)	-0.011
1 _{0,1}	5	1 _{1,0}	5	10288.183(1)	0.028
1 _{0,1}	3	1 _{1,0}	5	10308.665(50)	0.006
1 _{0,1}	5	1 _{1,0}	3	10325.016(4)	0.003
1 _{0,1}	3	1 _{1,0}	3	10345.530(5)	0.013
2 _{0,2}	1	2 _{1,1}	1	11527.025(7)	0.014
2 _{0,2}	1	2 _{1,1}	3	11543.343(5)	0.011
2 _{0,2}	3	2 _{1,1}	1	11550.550(6)	-0.006
2 _{0,2}	7	2 _{1,1}	7	11555.460(2)	0.024
2 _{0,2}	3	2 _{1,1}	3	11566.884(3)	0.007
2 _{0,2}	7	2 _{1,1}	5	11571.814(3)	0.004
2 _{0,2}	3	2 _{1,1}	5	11578.548(3)	0.024
2 _{0,2}	5	2 _{1,1}	3	11583.727(3)	-0.001
2 _{0,2}	5	2 _{1,1}	5	11595.389(3)	0.014

Table A.I.1 *Continued.*

J_{K_p, K_o}	2F	$J'_{K'_p, K'_o}$	2F'	Meas.	M-Calc.
3 _{0,3}	3	3 _{1,2}	3	13623.775(4)	-0.008
3 _{0,3}	3	3 _{1,2}	5	13633.956(4)	0.007
3 _{0,3}	9	3 _{1,2}	9	13641.558(6)	0.011
3 _{0,3}	9	3 _{1,2}	7	13651.754(6)	0.001
3 _{0,3}	5	3 _{1,2}	5	13661.933(3)	0.002
3 _{0,3}	5	3 _{1,2}	7	13666.701(5)	0.023
3 _{0,3}	7	3 _{1,2}	9	13669.568(15)	0.022
3 _{0,3}	7	3 _{1,2}	5	13675.000(3)	0.007
3 _{0,3}	7	3 _{1,2}	7	13679.760(8)	0.006
2 _{1,2}	1	3 _{0,3}	3	15677.957(4)	0.010
2 _{1,2}	3	3 _{0,3}	5	15686.858(5)	0.011
2 _{1,2}	7	3 _{0,3}	9	15691.215(3)	-0.016
2 _{1,2}	5	3 _{0,3}	7	15700.060(3)	0.007
2 _{1,2}	5	3 _{0,3}	5	15713.128(3)	-0.015
4 _{0,4}	5	4 _{1,3}	5	16719.820(9)	-0.016
4 _{0,4}	7	4 _{1,3}	7	16759.643(4)	-0.017
4 _{0,4}	9	4 _{1,3}	7	16771.354(4)	-0.029
0 _{0,0}	3	1 _{1,1}	3	17183.757(3)	-0.031
0 _{0,0}	3	1 _{1,1}	5	17200.136(3)	-0.005
0 _{0,0}	3	1 _{1,1}	1	17213.147(5)	-0.042

Table A.I.2 Measured and calculated (least-squares fit) transition frequencies for $^{37}\text{ClF}_3$. Frequencies in MHz. The standard deviation for the fit is 17kHz. Units in MHz.

J_{K_p, K_o}	2F	$J'_{K'_p, K'_o}$	2F'	Meas.	M-Calc.
1 _{1,1}	5	2 _{0,2}	5	6945.428(7)	-0.007
1 _{1,1}	3	2 _{0,2}	5	6958.340(8)	0.012
1 _{1,1}	5	2 _{0,2}	7	6964.043(7)	-0.001
1 _{1,1}	1	2 _{0,2}	1	6967.069(7)	0.026
1 _{1,1}	3	2 _{0,2}	3	6971.633(8)	0.002
1 _{0,1}	5	1 _{1,0}	3	10230.832(5)	0.000
1 _{0,1}	3	1 _{1,0}	3	10247.000(5)	0.006
2 _{0,2}	1	2 _{1,1}	1	11454.733(7)	0.005
2 _{0,2}	1	2 _{1,1}	3	11467.618(5)	0.018
2 _{0,2}	3	2 _{1,1}	1	11473.303(6)	-0.021
2 _{0,2}	7	2 _{1,1}	7	11477.198(3)	0.024
2 _{0,2}	3	2 _{1,1}	3	11486.210(3)	0.014
2 _{0,2}	7	2 _{1,1}	5	11490.081(6)	0.002
2 _{0,2}	3	2 _{1,1}	5	11495.406(2)	0.021
2 _{0,2}	5	2 _{1,1}	7	11495.817(10)	0.035
2 _{0,2}	5	2 _{1,1}	3	11499.501(3)	0.001
2 _{0,2}	5	2 _{1,1}	5	11508.696(5)	0.008
3 _{0,3}	3	3 _{1,2}	3	13565.239(5)	0.001
3 _{0,3}	3	3 _{1,2}	5	13573.264(4)	0.017
3 _{0,3}	9	3 _{1,2}	9	13579.298(4)	0.015
3 _{0,3}	5	3 _{1,2}	3	13587.347(24)	-0.030
3 _{0,3}	5	3 _{1,2}	5	13595.385(2)	0.001
3 _{0,3}	5	3 _{1,2}	7	13599.141(3)	0.016

Table A.I.2 *Continued.*

J_{K_p, K_o}	2F	$J'_{K'_p, K'_o}$	2F'	Meas.	M-Calc.
3 _{0,3}	7	3 _{1,2}	9	13601.456(3)	0.023
3 _{0,3}	7	3 _{1,2}	5	13605.721(6)	-0.008
3 _{0,3}	7	3 _{1,2}	7	13609.475(4)	0.007
2 _{1,2}	3	3 _{0,3}	5	15761.498(5)	0.005
2 _{1,2}	7	3 _{0,3}	9	15764.987(5)	-0.006
2 _{1,2}	5	3 _{0,3}	7	15771.888(4)	0.003
4 _{0,4}	5	4 _{1,3}	5	16686.710(9)	0.006
4 _{0,4}	5	4 _{1,3}	7	16691.772(16)	0.003
4 _{0,4}	7	4 _{1,3}	7	16718.198(3)	0.012
4 _{0,4}	9	4 _{1,3}	7	16727.466(9)	0.027
4 _{0,4}	9	4 _{1,3}	9	16729.263(8)	0.005
0 _{0,0}	3	1 _{1,1}	3	17085.911(3)	0.024
0 _{0,0}	3	1 _{1,1}	5	17098.825(10)	0.003
0 _{0,0}	3	1 _{1,1}	1	17109.079(2)	0.041

APPENDIX A.II:
TRANSITION FREQUENCIES FOR
COBALT TRI-CARBONYL NITROSYL, CYCLOPENTADIENYL
COBALT DI-CARBONYL, AND CYCLOPENTADIENYL
MANGANESE TRI-CARBONYL

Table A.II.1 Measured and calculated hyperfine transition frequencies for the $J = 2 \rightarrow 3$, $K=0$ transition for $\text{Co}(\text{CO})_3\text{NO}$ in MHz. The standard deviation for the fit was 11kHz. Units in MHz.

2I	2F	2I'	2F'	Meas.	M-Calc.
9	9	9	5	6249.592	-0.005
9	9	9	9	6251.695	0.002
7	9	7	11	6251.851	0.003
7	7	5	9	6251.993	-0.020
9	11	9	13	6252.112	-0.001
7	11	7	13	6252.518	0.004
9	13	9	15	6252.570	0.007
5	3	5	3	6252.629	-0.005
7	7	5	7	6252.867	0.005
9	11	9	11	6252.967	0.004
5	7	7	9	6253.500	-0.002
9	9	9	11	6253.649	0.010
9	5	9	5	6254.039	0.002
7	5	7	7	6255.387	0.002
9	7	9	9	6255.529	0.003
5	3	5	5	6255.651	-0.006
9	5	9	7	6257.027	0.024
9	13	9	13	6257.891	-0.023
7	11	7	11	6258.073	-0.004

Table A.II.2 Measured and calculated hyperfine transition frequencies for the $J = 3 \rightarrow 4$, $K=0$ transition for $^{59}\text{Co}(\text{CO})_3\text{NO}$ in MHz. The standard deviation for the fit was 9kHz. Units in MHz.

2I	2F	2I'	2F'	Meas.	M-Calc.
9	9	9	9	8335.891	-0.003
9	7	9	7	8336.174	-0.002
9	11	9	11	8336.292	0.001
9	13	9	15	8336.612	0.001
9	5	7	5	8337.706	0.003
5	1	9	3	8337.008	0.008
7	9	7	11	8337.106	-0.005
7	9	5	9	8337.265	0.003
5	7	7	9	8337.326	0.004
7	7	7	9	8337.936	-0.003
9	9	9	11	8338.183	-0.022
7	11	7	11	8338.242	0.009
5	3	5	5	8338.962	-0.005
5	5	5	5	8339.145	0.011

Table A.II.3 Measured and calculated transition frequencies for the $J = 4 \rightarrow 5$ transitions for $^{59}\text{Co}(\text{CO})_3\text{NO}$ in MHz. The standard deviation for the fit was 0.008 MHz.

2I	2F	2I'	2F'	Meas.	M-Calc.
9	9	7	9	10419.863	0.003
9	7	7	7	10420.066	-0.003
7	13	7	15	10421.088	0.010
9	15	9	17	10421.146	0.004
5	11	5	13	10421.216	0.004
7	19	7	17	10421.322	-0.009
9	17	9	19	10421.356	0.004
9	13	9	15	10421.421	-0.009
9	11	9	13	10421.804	-0.005
5	7	5	9	10421.935	-0.011
7	7	9	9	10422.202	0.011
9	9	9	11	10422.353	-0.002
7	5	5	7	10444.448	-0.001
9	7	7	9	10422.574	0.005
7	13	7	13	10423.035	0.001

Table A.II.4 Measured and calculated hyperfine transition frequencies for the $J = 5 \rightarrow 6$ transitions for $^{59}\text{Co}(\text{CO})_3\text{NO}$ in MHz. The standard deviation for the fit was 14 kHz.

2I	2F	2I'	2F'	Meas.	M-Calc.
9	15	9	15	12505.211	0.001
9	17	9	19	12505.493	-0.006
7	17	7	19	12505.653	0.012
9	19	9	21	12505.653	-0.002
5	5	5	7	12506.051	-0.002
9	9	9	11	12506.140	-0.022
9	5	9	7	12506.238	0.012
7	9	7	11	12506.434	0.006

Table A.II.5 Measured and calculated transition frequencies for the $J = 3 \rightarrow 4$ transitions for $^{59}\text{Co}(\text{CO})_3\text{NO}$ in MHz. The standard deviation for the fit was 0.01 MHz.

2I	2F	2I'	2F'	Meas.	M-Calc.
9	3	7	5	8330.883	-0.005
9	5	9	7	8332.637	0.001
7	13	7	15	8334.378	-0.006
9	15	9	17	8334.778	0.005
5	11	5	13	8334.819	-0.005
9	7	9	9	8335.397	0.006
7	5	7	7	8335.683	0.009
9	9	9	9	8339.038	-0.001
7	7	7	7	8339.232	-0.003
7	11	7	13	8339.556	0.013
5	9	5	11	8339.742	-0.014
7	9	8	11	8340.399	0.011
5	7	5	7	8340.613	-0.013

Table A.II.6 Measured and calculated transition frequencies for the hindered rotor spectrum of $\text{CpCo}(\text{CO})_2$. The measured frequencies are averaged over many hyperfine components caused by the quadrupole coupling interaction of the cobalt atom and also possible m -state splitting. Standard deviation for the fit = 10 kHz. Frequencies in MHz .

m'	J'	K'	m	J	K	Measured	Calc.	(M-C)
0	3	0	0	2	0	6064.1	6053.2	10.9
1	3	1	1	2	1	6087.1	6083.6	3.5
2	3	2	2	2	2	6274.3	6268.5	5.9
0	4	0	0	3	0	7806.8	7808.5	1.7
1	4	1	1	3	1	7819.0	7816.5	2.5
0	4	2	0	3	2	8478.0	8458.1	19.9
1	4	3	1	3	3	8825.8	8822.3	3.5
1	4	-1	1	3	-1	8841.8	8839.2	2.6
0	5	0	0	4	0	9527.1	9524.8	2.3
1	5	1	1	4	1	9527.1	9525.2	2.0
1	5	3	1	4	3	10790.3	10804.0	13.7
0	6	0	0	5	0	11242.3	11249.3	7.1
2	6	0	2	5	0	13396.7	13405.6	8.9
0	7	0	0	6	0	12978.3	12987.3	9.0
0	8	0	0	7	0	14738.1	14733.5	4.8

Table A.II.7 Measured and Calculated (Calc.) frequencies for quadrupole hyperfine structure on $K = 0$, $m = 0$ for $J \rightarrow J' = 2 \rightarrow 3$, $3 \rightarrow 4$, $4 \rightarrow 5$ transitions for $\text{CpCo}(\text{CO})_2$. $eQq_{aa} = 12(4)$ MHz and $eQq_{bb} = 113(4)$ MHz. Standard deviation for the fit = 0.07 MHz. Frequencies in MHz.

J	$2F$	J'	$2F'$	Measured	Calc.	(M-C)
2	5	3	3	6053.13	6053.15	-0.02
2	7	3	5	6056.38	6056.40	-0.02
2	11	3	13	6060.42	6060.40	0.02
2	5	3	5	6063.14	6053.19	-0.05
2	7	3	7	6066.39	6066.39	0.00
2	9	3	11	6068.31	6068.28	0.03
2	7	3	9	6072.42	6072.36	0.05
2	11	3	11	6078.96	6078.97	-0.01
3	13	4	15	7808.43	7808.32	0.11
3	7	4	7	7808.85	7808.85	0.00
3	9	4	9	7812.98	7813.02	-0.04
3	11	4	13	7813.46	7813.45	0.01
3	9	4	11	7817.15	7817.15	0.00
3	7	4	9	7819.01	7819.00	0.01
3	11	4	11	7820.21	7820.28	-0.07
3	13	4	13	7832.00	7832.02	-0.02
4	9	5	9	9522.70	9522.83	-0.13
4	15	5	17	9525.09	9525.06	-0.03
4	13	5	15	9527.75	9527.78	-0.03
4	11	5	11	9528.24	9528.20	0.04
4	11	5	13	9530.58	9530.44	0.13
4	9	5	11	9532.41	9532.33	0.08
4	7	5	9	9532.86	9532.98	-0.12

Table A.II.8 Hyperfine components for the $J = 2 \rightarrow 3$ rotational transition and their corresponding assignments $\text{CpMn}(\text{CO})_3$. Observed transitions are $F \rightarrow F'$ and listed frequencies are in MHz units. The $\sigma_{FIT} = 10 \text{ kHz}$

K	F	F'	Meas.	Calc.	M-C
2	9	11	4963.357	4963.352	0.005
1	3	3	4964.982	4964.991	-0.009
1	9	11	4966.396	4966.384	0.012
0	7	9	4966.749	4966.741	0.008
0	9	11	4967.405	4967.395	0.010
1	7	9	4969.160	4969.170	-0.010
0	5	7	4970.125	4970.136	-0.011
1	5	7	4970.866	4970.863	0.003
2	5	7	4973.049	4973.045	0.004
2	7	9	4976.460	4976.455	0.005

Table A.II.9 Hyperfine components for the $J = 3 \rightarrow 4$ rotational transition and their corresponding assignments for $\text{CpMn}(\text{CO})_3$. Frequencies in MHz .

K	F	F'	Meas.	Calc.	M-C
0	5	5	6618.920	6618.911	0.009
3	11	13	6619.333	6619.347	-0.014
2	1	3	6619.370	6619.369	0.001
1	5	5	6619.760	6619.753	0.007
2	11	13	6621.787	6621.789	-0.002
1	11	13	6623.259	6623.254	0.005
0	9	11	6623.339	6623.325	0.014
0	11	13	6623.753	6623.742	0.011
1	9	11	6624.141	6624.144	-0.003
0	7	9	6624.778	6624.776	0.002
2	7	7	6625.241	6625.250	-0.009
1	7	9	6625.380	6625.377	0.003
1	3	5	6625.715	6625.716	-0.001
1	5	7	6626.075	6626.077	-0.002
2	9	11	6626.565	6626.602	-0.037
2	7	9	6627.163	6627.178	-0.015
3	7	9	6630.174	6630.179	-0.005
3	9	11	6630.705	6630.699	0.006
0	11	11	6635.767	6635.762	0.005

Table A.II.10 Hyperfine components for the $J = 4 \rightarrow 5$ rotational transition and their corresponding assignments for $\text{CpMn}(\text{CO})_3$. Frequencies in MHz .

K	F	F'	Meas.	Calc.	M-C
3	3	5	8274.890	8274.889	0.001
2	5	5	8275.394	8275.406	-0.012
4	13	15	8275.585	8275.585	0.000
0	9	9	8276.615	8276.593	0.022
2	7	7	8277.205	8277.200	0.005
3	13	15	8277.486	8277.493	-0.007
3	5	7	8278.239	8278.238	0.001
3	13	13	8278.643	8278.641	0.002
2	13	15	8278.842	8278.856	-0.015
1	13	15	8279.682	8279.673	0.009
0	13	15	8279.960	8279.946	0.014
1	11	13	8280.018	8280.013	0.005
1	3	5	8280.401	8280.396	0.005
0	9	11	8280.465	8280.459	0.006
1	9	11	8280.811	8280.809	0.002
1	5	7	8281.351	8281.349	0.002
0	7	9	8281.392	8281.387	0.005
2	7	9	8281.443	8281.458	-0.015
3	7	9	8281.547	8281.548	0.001
2	9	11	8281.839	8281.859	-0.020
0	11	11	8281.906	8281.886	0.020
1	11	11	8282.027	8282.019	0.008
3	11	13	8282.864	8282.880	-0.016
3	9	9	8283.186	8283.203	-0.017
3	9	11	8283.604	8283.608	-0.004
4	11	13	8285.398	8285.388	0.010
2	13	13	8285.872	8285.882	-0.010
4	9	11	8286.063	8286.057	0.005

Table A.II.11 Hyperfine components for the $J = 5 \rightarrow 6$ rotational transition and their corresponding assignments for $\text{CpMn}(\text{CO})_3$. Frequencies in MHz .

K	F	F'	Meas.	Calc.	M-C
1	9	9	9930.711	9930.699	0.012
2	7	7	9930.584	9930.605	-0.021
5	15	17	9931.890	9931.893	-0.003
2	9	9	9932.310	9932.330	-0.020
4	15	17	9933.405	9933.398	0.007
3	5	7	9933.574	9933.579	-0.005
3	15	17	9934.567	9934.570	-0.003
4	7	9	9934.652	9934.630	0.022
3	9	9	9935.042	9935.049	-0.007
2	5	7	9935.386	9935.382	0.004
3	7	9	9935.770	9935.773	-0.003
1	15	17	9935.913	9935.908	0.005
1	13	15	9936.048	9936.044	0.004
0	15	17	9936.074	9936.076	-0.002
0	11	13	9936.371	9936.370	0.001
1	5	7	9936.471	9936.464	0.007
1	11	13	9936.561	9936.582	-0.021
0	9	11	9937.000	9936.986	0.014
1	9	11	9937.043	9937.044	-0.001
1	7	9	9937.078	9937.079	-0.001
3	13	15	9937.497	9937.514	-0.017
4	9	11	9937.914	9937.902	0.012
5	9	11	9938.419	9938.418	0.001
2	13	13	9938.543	9938.545	-0.002
1	13	13	9938.597	9938.587	0.010
4	1	15	9938.801	9938.799	0.002
3	11	13	9938.268	9938.273	-0.005
4	11	13	9939.762	9939.753	0.009
4	11	11	9940.185	9940.190	-0.005
5	13	15	9940.459	9940.452	0.007
5	11	13	9941.656	9941.655	0.001

Table A.II.12 Hyperfine components for the $J = 6 \rightarrow 7$ rotational transition and their corresponding assignments for $\text{CpMn}(\text{CO})_3$. Frequencies in MHz .

K	F	F'	Meas.	Calc.	M-C
1	17	19	11592056	11592049	0.007
1	15	17	11592102	11592098	0.004
0	13	15	11592336	11592344	-0.008
1	13	15	11592478	11592480	-0.002
1	11	13	11592839	11592838	0.001
1	9	11	11592899	11592900	-0.001
3	11	13	11593260	11593270	-0.010
4	15	17	11593682	11593672	0.010

APPENDIX A.III:
TRANSITION FREQUENCIES FOR
CYCLOBUTADIENE IRON TRI-CARBONYL, CYCLOHEXADIENE
IRON TRI-CARBONYL, AND BUTADIENE IRON TRI-CARBONYL

Table A.III.1 Measured and calculated $J + 1 \leftarrow J$ transition frequencies for cyclobutadiene iron tricarbonyl. Units in MHz.

J	K	Meas.	M-C
2	0	5771.893	-0.004
2	1	5771.893	0.004
2	2	5771.865	0.002
3	0	7695.843	0.002
3	1	7695.843	0.012
3	2	7695.793	-0.009
3	3	7695.759	0.005
4	0	9619.761	-0.006
4	1	9619.761	0.006
4	2	9619.717	0.002
5	0	11543.668	-0.004
5	1	11543.668	0.013
5	2	11543.601	-0.013
5	3	11543.547	0.006
6	0	13467.545	-0.004
6	4	13467.272	-0.006
7	0	15391.408	0.012
7	2	15391.303	-0.015
7	3	15391.224	0.003
7	4	15391.093	-0.003

Table A.III.2 Measured transition frequencies and least squares residuals (M.-C.) for C-hex⁵⁶Fe(CO)₃. Units in MHz.

J_{K_p, K_o}	$J'_{K'_p, K'_o}$	Meas.	(M.-C.)
3 _{1,3}	4 _{1,4}	5317.020	-0.0004
3 _{0,3}	4 _{0,4}	5351.691	0.0012
3 _{2,2}	4 _{2,3}	5363.540	0.0008
3 _{3,1}	4 _{3,2}	5367.055	0.0025
3 _{2,1}	4 _{2,2}	5376.413	-0.0003
3 _{1,2}	4 _{1,3}	5406.840	-0.0005
3 _{0,3}	4 _{1,3}	5769.572	-0.0007
3 _{1,2}	4 _{2,2}	6184.592	0.0017
4 _{1,3}	5 _{0,5}	6262.795	-0.0012
3 _{1,3}	4 _{2,3}	6300.294	0.0004
4 _{1,4}	5 _{1,5}	6644.117	0.0005
4 _{0,4}	5 _{0,5}	6680.680	0.0005
4 _{2,3}	5 _{2,4}	6702.779	0.0030
4 _{1,3}	5 _{1,4}	6755.745	-0.0012
4 _{2,2}	5 _{2,3}	6727.786	-0.0008
4 _{3,1}	5 _{3,2}	6710.729	-0.0008
4 _{3,2}	5 _{3,3}	6709.728	-0.0005
4 _{4,0}	5 _{4,1}	6708.620	-0.0082
3 _{2,1}	4 _{3,1}	6808.935	-0.0011
3 _{2,2}	4 _{3,2}	6815.138	-0.0014
4 _{0,4}	5 _{1,4}	7173.634	0.0036
4 _{1,3}	5 _{2,3}	7505.538	0.0011
5 _{1,5}	6 _{1,6}	7970.010	-0.0014
5 _{0,5}	6 _{0,6}	8005.089	0.0001
5 _{2,4}	6 _{2,5}	8040.927	0.0011
5 _{5,1}	6 _{5,2}	8050.118	-0.0011
5 _{4,2}	6 _{4,3}	8051.282	0.0041
5 _{4,1}	6 _{4,2}	8051.324	-0.0058

Table A.III.2 Continued.

J_{K_p, K_o}	$J'_{K'_p, K'_o}$	Meas.	(M.-C.)
5 _{3,3}	6 _{3,4}	8052.777	-0.0003
5 _{3,2}	6 _{3,3}	8055.422	-0.0008
5 _{2,3}	6 _{2,4}	8082.621	0.0019
5 _{1,4}	6 _{1,5}	8102.518	0.0013
4 _{2,3}	5 _{3,3}	8161.329	0.0003
4 _{2,2}	5 _{3,2}	8143.252	0.0004
5 _{0,5}	6 _{1,5}	8595.464	-0.0031
6 _{2,4}	7 _{1,6}	8716.581	0.0009
5 _{1,4}	6 _{2,4}	8832.409	0.0001
6 _{1,6}	7 _{1,7}	9294.673	0.0014
6 _{0,6}	7 _{0,7}	9325.627	0.0002
6 _{2,5}	7 _{2,6}	9377.789	0.0011
6 _{6,1}	7 _{6,2}	9391.637	-0.0033
6 _{4,2}	7 _{4,3}	9394.598	0.0007
6 _{3,4}	7 _{3,5}	9396.065	0.0025
6 _{3,3}	7 _{3,4}	9401.932	0.0006
6 _{2,4}	7 _{2,5}	9439.950	-0.0019
6 _{1,5}	7 _{1,6}	9446.473	0.0007
5 _{2,3}	6 _{3,3}	9470.890	0.0021
5 _{2,4}	6 _{3,4}	9511.328	-0.0020
7 _{1,7}	8 _{1,8}	10618.143	-0.0002
7 _{0,7}	8 _{0,8}	10643.546	-0.0004
7 _{2,6}	8 _{2,7}	10713.174	-0.0111
7 _{6,1}	8 _{6,2}	10734.039	0.0023
7 _{5,3}	8 _{5,4}	10735.506	0.0029
7 _{4,4}	8 _{4,5}	10738.099	-0.0022
7 _{4,3}	8 _{4,4}	10738.574	-0.0002

Table A.III.2 Continued.

J_{K_p, K_o}	$J'_{K'_p, K'_o}$	Meas.	(M.-C.)
7 _{3,5}	8 _{3,6}	10739.374	-0.0012
7 _{3,4}	8 _{3,5}	10750.856	0.0084
7 _{1,6}	8 _{1,7}	10786.850	-0.0006
7 _{2,5}	8 _{2,6}	10798.255	0.0014
8 _{1,8}	9 _{1,9}	11940.531	-0.0026
8 _{0,8}	9 _{0,9}	11960.158	-0.0001
8 _{2,7}	9 _{2,8}	12046.967	0.0001
8 _{6,2}	9 _{6,3}	12076.722	-0.0049
8 _{5,3}	9 _{5,4}	12078.852	0.0122
8 _{4,5}	9 _{4,6}	12082.322	-0.0016
8 _{3,6}	9 _{3,7}	12082.445	0.0020
8 _{1,7}	9 _{1,8}	12122.886	0.0012
9 _{1,9}	10 _{1,10}	13261.989	-0.0011
9 _{0,9}	10 _{0,10}	13276.439	0.0022
9 _{2,8}	10 _{2,9}	13379.031	0.0027
9 _{3,7}	10 _{3,8}	13424.956	-0.0009
9 _{4,6}	10 _{4,7}	13427.064	-0.0021
9 _{4,5}	10 _{4,6}	13429.468	-0.0010
9 _{1,8}	10 _{1,9}	13453.972	0.0006
9 _{3,6}	10 _{3,7}	13458.104	-0.0032
9 _{2,7}	10 _{2,8}	13511.508	-0.0010

Table A.III.3 Measured transition frequencies and least squares residuals (M.-C.) for C-hex⁵⁴Fe(CO)₃. Units in MHz.

J_{K_p, K_o}	$J'_{K'_p, K'_o}$	Meas.	(M.-C.)
4 _{1,4}	5 _{1,5}	6645.883	-0.0004
4 _{0,4}	5 _{0,5}	6682.449	0.0002
4 _{2,3}	5 _{2,4}	6704.589	0.0004
4 _{2,2}	5 _{2,3}	6729.647	0.0007
4 _{1,3}	5 _{1,4}	6757.591	-0.0001
5 _{1,5}	6 _{1,6}	7972.126	0.0005
5 _{0,5}	6 _{0,6}	8007.193	-0.0004
5 _{2,4}	6 _{2,5}	8043.095	-0.0004
5 _{2,3}	6 _{2,4}	8084.863	-0.0005
5 _{1,4}	6 _{1,5}	8104.720	-0.0003
6 _{1,6}	7 _{1,7}	9297.133	0.0000
6 _{0,6}	7 _{0,7}	9328.065	0.0000
6 _{2,5}	7 _{2,6}	9380.314	-0.0001
6 _{1,5}	7 _{1,6}	9449.029	0.0005

References

1. H.A. Fry and S.G. Kukolich, *J. Chem. Phys.* **76**, 4387 (1982).
2. T.J. Balle and W.H. Flygare, *Rev. Sci. Instrum.* **52**, 33 (1981).
3. F.J. McQuillin, D.G. Parker, and G.R. Stepheson, *T. Metal Organometallics for Organic Synthesis*, University Press, Cambridge 1991.
4. G.W. Parshall, *Homogeneous Catalysis*, John Wiley and Sons, New York, 1980.
5. *Dynamics of Polyatomic Van der Waals Complexes*, Eds. N. Halberstadt and K.C. Janda, NATO ASI series. Series B: Physics v. 227.
6. *Structure and Dynamics of Weakly Bound Molecular Complexes*, Ed. A. Weber, NATO ASI series. Series C: Mathematical and Physical Sciences v. 212.
7. R. Bumgarner, *Microwave Spectroscopy of Weakly Bound Complexes and High Resolution Infrared Studies of the ν_6 and ν_8 Bands of Formic Acid*, Ph.D. Dissertation, University of Arizona, 1988, Chp. II.
8. J.B. Anderson, *Molecular Beams and Low Density Gas Dynamics*, Ed. P.P. Wegener (Marcel Dekker, New York, 1974).
9. H. Pauly and J.P. Toennies, *Methods of Experimental Physics*, Eds. B. Bederson and W.L. Fite (Academic, New York, 1968), Vol. 7, pt. A.
10. J.B. Anderson, R.P. Andres, and J.B. Finn, *Advances in Chemical Physics*, Ed. I. Prigogine (Wiley, New York, 1974), Vol. 25.
11. K. Bier and O. Hagena, *Rarified Gas Dynamics*, Ed. J.H. deLeur (Academic, New York, 1966), Vol. II.
12. H. Ashkenas and F.S. Sherman, *Rarified Gas Dynamics*, Ed. J.H. deLeur (Academic, New York, 1966), Vol. II.
13. O.F. Hagena and W. Obert, *J. Chem. Phys.* **56**, 1793 (1972).
14. D. Golomb, R.E. Good, A.B. Bailey, M.R. Busby, and R. Dawborn, *J. Chem. Phys.* **57**, 3844 (1970).
15. D. Golomb, and R.F. Brown, *J. Chem. Phys.* **52**, 1545 (1970).
16. .M. Calo, *J. Chem. Phys.* **62**, 4904 (1975).
17. T.A. Milen, A.E. Vandegrift, and F.T. Green, *J. Chem. Phys.* **52**, 1552 (1970).
18. A.C. Legon, *Ann. Rev. Phys. Chem.* **34**, 275 (1983).
19. E.J. Campbell, L.W. Buxton, T.J. Balle, and W.H. Flygare, *J. Chem. Phys.* **74**, 829 (1981).
20. W. Gordy and R.L. Cook, "Microwave Molecular Spectra", John Wiley and Sons, New York (1984), Ch. 14.
21. D.J. Millen and J. Pannell, *J. Chem. Soc.*, 1322 (1961).
22. G. Cazzoli, R. Cervellati, and A.M. Mirri, *J. Mol. Spect.* **56**, 422 (1975); A. Guarnieri and P.G. Favero, *Nuovo Cimento* **39**, 76 (1965).

23. R.E. Bumgarner and S.G. Kukolich, *J. Chem. Phys.* **86**, 1083 (1987).
24. S.G. Kukolich, J.V. Rund, D.J. Pauley and R.E. Bumgarner, *J. Am. Chem. Soc.* **110**, 7356 (1988).
25. Coleman, *Inorganic syntheses* **1**, 55 (1939).
26. S.G. Kukolich, *Mol. Phys.* **29**, 249 (1975).
27. S.G. Kukolich and C.D. Cogley, *J. Chem. Phys.* **76**, 1685 (1982).
28. G. Cazzoli, R. Cervellati, and A.M. Mirri, *J. Mol. Spect.* **56**, 422 (1975); A. Guarnieri and P.G. Favero, *Nuovo. Cim.* **39**, 76 (1965) .
29. D.F. Smith, *J. Chem. Phys.* **21**, 609 (1953).
30. R.D. Burbank and F.N. Bensey, *JCP*, **21**, 602 (1953).
31. J.H. Holloway, Ph.D. thesis, Department of Physics, M.I.T., 1956; J.H. Holloway, B.B. Aubrey, and J.G. King (unpublished results)..
32. A.A. Ishchenko, I.N. Myakshin, G.V. Romanov, V.P. Spiridonov, and V.F. Sukhoverkhov, *Dokl. Acad. Nauk. USSR* **267**, 1143 (1982)..
33. D.W. Magnuson, *J. Chem. Phys.* **27**, 233 (1957)..
34. R.D. Feltham and J.H. Enemark, "Topics in Stereo Chemistry", G.L. Geoffroy, Ed. Vol **12**, 155 (1981).
35. W.L. Meerts, *Chem. Phys* **14**, 421 (1976).
36. K.H. Casleton and S.G. Kukolich, *J. Chem. Phys.* **62**, 2696 (1975).
37. K.S. Buckton, A.C. Legon and D.J. Millen, *Trans. Faraday Soc.* **65**, 1975 (1969).
38. D.Coffey, C.O. Britt and J.E. Boggs, *J. Chem. Phys.* **49**, 591 (1968).
39. Landolt-Bornstein- Numerical data and functional relationships in science and technology (Springer, Berlin, 1974) Vol 6..
40. S.G. Kukolich and A.C. Nelson, *J. Am. Chem. Soc.* **95**, 680 (1973).
41. J.G. King and V. Jaccarino, *Phys. Rev.* **94**, 1610 (1954).
42. C.D. Cogley, H.A. Fry, and S.G. Kukolich, *J. Mol. Spectrosc.* **75**, 447 (1979).
43. J. March, *Advanced Organic Chemistry*, McGraw Hill Book Co., New York 1977.
44. A.C. Lehninger, *Biochemistry*, Worth Publishers Inc., New York, 1978.
45. K. Hedberg, L. Hedberg, K. Hagen, R.K. Ryan and L.H. Jones, *Inorg. Chem.* **24**, 2771 (1989).
46. A.P. Cox, L.F. Thomas and J. Sheridan, *Nature* **181**, 1157L (1958).
47. Values from: W. Gordy and R.L. Cook, *Microwave Molecular Spectra*, 3rd Ed., John Wiley and Sons, New York (1984); 1 barn = 10⁻²⁴ cm²..
48. S.G. Kukolich, J.V. Rund, D.J. Pauley and R.E. Bumgarner, *J. Am. Chem. Soc.* **110**, 7356 (1988).

49. E.A.C. Lucken, Nuclear Quadrupole Coupling Constants, Ch. 13, pp. 328-329, Academic Press, London (1969).
50. F.A. Cotton and G. Wilkinson, Advanced Inorganic Chemistry, Ch.27, Interscience, New York (1962).
51. W.L. Meerts, Chem. Phys. 14, 921 (1976) (See discussion in Ref. 6).
52. B.Beagley, C.T.Parrot, V.Ulbrecht and G.G.Young, *J. Mol. Struct.* **52**, (1979) 47 .
53. S.G.Kukolich, M.A.Roehrig, S.T.Haubrich and J.C.Shea, *J. Chem. Phys.***94**, (1991) 191.
54. E.B.Wilson, C.C.Lin and D.R.Lide, *J. Chem. Phys.***23**, 136 (1955).
55. C.C.Lin and J.D.Swalen, *Rev. Mod. Phys.* **31**, (1959) 841.
56. W.M.Tolles, E.Tannenbaum Handelman and W.D.Gwinn, *J. Chem. Phys.***43**, (1965) 3019.
57. S.T. Haubrich, M.A. Roehrig and S.G. Kukolich, *J. Chem. Phys.***93**, (1990) 121.
58. B.E Mann, In *Comprehensive Organometallic Chemistry*, G. Wilkinson, F.G.A. Stone, E.W Abel, Eds; Pergamon Press: Oxford 1982, Vol 3 pp 89-171.
59. E.V.Ivash and D.M.Dennison, *J. Chem. Phys.***21**, 1804 (1953).
60. K.M.Sinnott, *J. Chem. Phys.***34**, 851 (1961).
61. Tannenbaum, Myers and Gwinn, *J. Chem. Phys.***25**, 42 (1956).
62. R.E.Naylor Jr. and E.B.Wilson Jr., *J. Chem. Phys.***26**, 1057 (1957).
63. J.K. Tyler, A.P. Cox and J. Sheridan, *Nature* **183**, 1182 (1959).
64. T.B. Brill and G.G. Long, *Inorg. Chem.* **10**, 74 (1971).
65. C.C. Lin and J.D. Swalen, *Rev. Mod. Phys.* **31**, 841 (1959).
66. A.F. Berndt and R.E. Marsh, *Acta. Cryst.* **16** (1963).
67. F.A. Cotton, G. Wilkinson, *Advanced Inorganic Chemistry*, 5th ed., John Wiley and Sons, New York, 1988.
68. J.P. Collman, L.C. Hegedus, J.R. Norton, R.G. Finke, *Principles and Applications of Organotransition Metal Chemistry*, University Science Books, Mill Valley, CA, 1987.; R.H. Crabtree, *The Organometallic Chemistry of the Transition Metals*, John Wiley and Sons: New York, 1988.
69. G.F Emerson, L. Watts, and R. Pettit, *J. Am. Chem. Soc.* **87**, 131-133 (1965).
70. T.H. Lowry and K.S. Richardson, "Mechanism and Theory in Organic Chemistry"; Harper and Row: New York, 1987, 31-52 .
71. G. Maier, S. Pfrien, U. Schafer, and R. Matusch, *Angew. Chem. Int. Ed. Engl.* **17**, 520-521 (1978).

72. L. Salem, 'The Molecular Orbital Theory of Conjugated Systems', W.A. Benjamin: New York, 1966, Chap. 8 .
73. H. Oberhammer and H.A. Brune, *Z. Naturforsch* **24a**, 607-612 (1969).
74. M.I. Davis and C.S. Speed, *J. Organometallic Chem.* **21**, 401-413 (1973).
75. E.A. Lucken, R. Pozzi, and K.R. Ramaprasad, *J. Mol. Struct.* **18**, 377-380 (1973).
76. R. Pettit and J. Henery, *Organic Synthesis* **50**, 21-24 (1979).
77. S.G. Kukolich, J.V. Rund, D.J. Pauley, and R.E. Bumgarner, *J. Am. Chem. Soc.* **110**, 7356 (1988).
78. S.G. Kukolich, M.A. Roehrig, S.T. Haubrich, and J.C. Shea, *J. Chem. Phys.* **94**, 191-194 (1991).
79. S.G. Kukolich, M.A. Roehrig, D.W. Wallace, and Qi-Qi Chen, *Submitted to Chemical Physics Letters*.
80. C.C Lin and J.D. Swalen, *Rev. Mod. Phys.* **31**, 841-892 (1954).
81. F.A. Cotton and J.M. Troup, *J. Organomet. Chem.* **77**, 369 (1974).
82. W. Tam, D.F. Eaton, J.C. Calabrese, I.D. Williams, Y. Wang, and A.G. Anderson, *Chem. Mater.* **1**, 128 (1989).
83. J.K.G. Watson, *Vibrational Spectra and Structure*, J.R. Durig, Ed., Elsevier, New York, 1977, Vol. 6, pp 1-89.
84. J. Calabrese, E. I. du Pont de Nemours and Co., Willmington, DE, 19880, private communication.
85. L.H. Scharpen, V.W. Laurie, *J. Chem. Phys.* **43**, 2765 (1965).
86. D. Damiani, L. Ferretti, and E. Gallinella, *Chem. Phys. Lett.* **37**, 265 (1976).
87. H. Reihlen, A. Gruhl, G. VonHesting, and O. Pfrangle, *Justus Liebiop Ann. Chem.* **482**, 161 (1930).
88. B.F. Hallam and P.L. Pauson, *J. Chem. Soc.* **1958**, 642.
89. R. Pettit and G.F. Emerson, *Adv. Organomet. Chem.* F.G.A. Stone and R. West, Eds., **1** 1.
90. S.G. Kukolich, M.A. Roehrig, G.L. Henderson, and Qi-Qi Chen, *J. Chem. Phys.* **97**, 829 (1992).
91. S.G. Kukolich, M.A. Roehrig, D.W. Wallace, and G.L. Henderson, *J. Am. Chem. Soc.*, in press.
92. M.D. Marshall, D.G. Prichard and J.S. Muentner, *J. Chem. Phys.* **90**, 6049 (1989).
93. A.C. Legon, A.L. Wallwork, J.W. Bevan, and Z. Wang, *Chem. Phys. Lett.* **180**, 57 (1991).
94. M.D. Marshall, J. Kim, T.A. Hu, L.H. Sun and J.S. Muentner, *J. Chem. Phys.* **94**, 6334 (1991).

95. A.C. Legon, P.D. Soper and W.H. Flygare, *J. Chem. Phys.* **74**, 4944 (1981).
96. P.D. Soper, A.C. Legon and W.H. Flygare, *J. Chem. Phys.* **74**, 2138 (1981); R.S. Altman, M.D. Marshall, W. Klemperer and A. Krupnov, *ibid.* **79**, 52 (1985).
97. M.R. Keenan, T.K. Minton, A.C. Legon, T.J. Balle and W.H. Flygare, *Proc. Natl. Acad. Sci.*, **77**, 5583 (1980).
98. F.J. Goodwin and A.C. Legon, *Chem. Phys. Lett.* **87**, 81 (1984).
99. A. Suckley, Z. Wang, G. Bandarage, R.R. Lucchese, A.C. Legon and J.W. Bevan, 46th *Ohio State University international Symposium on Molecular Spectroscopy, June 17-21, 1991*. Paper TF'8.
100. D.J. Millen, *Can. J. Chem* **63**, 147 (1985).
101. T.C. Germann, S.L. Tschopp, and H.S. Gutowsky, 47th *Ohio State University International Symposium on Molecular Spectroscopy, June 15-19, 1992*, talk: THO3.
102. L. Adamowicz, *Chem. Phys. Lett.* **192**, 199 (1992).